



Friedrich-Schiller-Universität Jena
Physikalisch-Astronomische Fakultät
Thüringer Landessternwarte Tautenburg



Investigation of Class I jets with SOFIA

Dissertation

To fulfill the requirements for the Degree of
doctor rerum naturalium (Dr. rer. nat.)

Submitted to

**The Council of Faculty of Physics & Astronomy
of the Friedrich-Schiller-Universität Jena**

by **M. Sc. Thomas Sperling**

born on **20.09.1986** in **Magdeburg, Germany**

Referees

1. Prof. Dr. Artie Hatzes

Thüringer Landessternwarte Tautenburg

2. Prof. Dr. Tom Ray

Dublin Institute for Advanced Studies

3. Prof. Dr. Peter Schilke

Universität zu Köln

Date of defense: 06. July 2021

Zusammenfassung

Protostellare Ausströmungen in Form von Jets oder weniger stark kollimierten Winden sind spektakuläre Phänomene der Sternentstehung (Bally 2016; Frank *et al.* 2014). Junge Sterne führen über sie während ihrer Akkretionsphase überschüssigen Drehimpuls ab. Sie sind geeignete Laboratorien für die Untersuchung des Ejektions-Mechanismus, der in vielen astrophysikalischen Objekten (Aktive Galaxienkerne, Pulsare, Gamma-Ray Bursts etc.) eine zentrale Rolle spielt.

Im Rahmen dieser Arbeit wurden erstmalig neun protostellare Ausströmungen (Cep E, HH 1, HH 212, HH 26, HH 34, HH 111, L1551 IRS5, SVS 13, HH 30) in den beiden ferninfraroten Emissionslinien von atomarem Sauerstoff bei 63,18 μm und 145,53 μm mit der *fliegenden* Sternwarte SOFIA kartiert.

Räumlich aufgelöste $[\text{O I}]_{63,145}$ Karten zeigen die warme ($T \sim 500\text{--}5\,000\text{ K}$), neutrale und dichte Gaskomponente der Ausströmung an. Das Stoßwellenmodell von Hollenbach and McKee (1989) sagt vorher, dass die $[\text{O I}]_{63}$ Linie die stärkste Kühllinie in einer in der Ausströmung eingebetteten dissoziativen Stoßwelle ist. Sie bietet daher potentiell die Möglichkeit, Massenausflussraten \dot{M}_{out} zu messen. Mit Abschätzungen zu den Akkretionsraten \dot{M}_{acc} aus stellaren Parametern kann damit auch die Effizienz der Ausströmung, das heißt das Verhältnis $\dot{M}_{\text{out}}/\dot{M}_{\text{acc}}$, untersucht und mit theoretischen Modellen verglichen werden.

Nisini *et al.* (2015) kartierten bereits fünf protostellare Ausströmungen in $[\text{O I}]_{63,145}$ mit Herschel/PACS und konzentrierten sich in ihrer Studie auf Klasse 0-Quellen. Podio *et al.* (2012) hingegen konnten die $[\text{O I}]_{63}$ Linie in vier deutlich weiter entwickelten Klasse II-Ausströmungen auflösen. In dieser Arbeit wird mit neuen SOFIA Beobachtungen von vorwiegend Klasse 0 und Klasse I-Ausströmungen versucht, die vorhandene Lücke zu schließen und die Rolle der neutralen Gaskomponente in der Evolution junger Ausströmungen zu bewerten.

Die Ergebnisse dieser Arbeit zeigen, dass die überwiegende Mehrheit der Klasse 0-Ausströmungen eine dominante molekulare Komponente besitzt. Die meisten Klasse I-Ausströmungen weisen hingegen eine dominante neutrale Komponente auf, die durch die $[\text{O I}]_{63}$ Linie nachgewiesen wird. Mit diesen Ergebnissen wird die Vermutung untermauert, dass protostellare Ausströmungen mit der antreibenden Quelle eine zeitliche Entwicklung durchlaufen. Während der Protostern-Entwicklung von Klasse 0 über Klasse I zu Klasse II-Objekten scheint die zugehörige Ausströmung tendenziell (aber nicht notwendigerweise) heißer, dünner und schneller zu werden.

Abstract

Protostellar outflows in form of highly collimated jets or less collimated winds are spectacular phenomena associated with star formation (Bally 2016; Frank *et al.* 2014). Through them excess angular momentum is transported away from the young forming star during its main accretion phase. Outflows are proficient laboratories to study the ejection mechanism that plays a crucial role in many astrophysical objects (e.g. active galactic nuclei [AGNs], pulsars, Gamma-Ray Bursts).

In this study nine protostellar outflows (Cep E, HH 1, HH 212, HH 26, HH 34, HH 111, L1551 IRS5, SVS 13, HH 30) have been mapped for the first time in both far-infrared transitions of atomic oxygen at 63.18 μm and 145.53 μm using the *fly-ing* observatory SOFIA.

These $[\text{OI}]_{63,145}$ maps enable us to trace the warm ($T \sim 500\text{--}5\,000\text{ K}$), neutral, and dense gas component of the outflow. The $[\text{OI}]_{63}$ emission line is predicted to be the main coolant in a dissociative J-shock (Hollenbach and McKee 1989). Potentially, mass-loss rates \dot{M}_{out} can be determined from the $[\text{OI}]_{63}$ line luminosity. Thus, the efficiency $\dot{M}_{\text{out}}/\dot{M}_{\text{acc}}$, that is the ratio between the mass-loss in the outflow and the mass accretion onto the source (\dot{M}_{acc} , from stellar parameters), can be estimated and compared with theoretical model predictions.

Nisini *et al.* (2015) have already mapped five protostellar outflows from mainly Class 0 sources in $[\text{OI}]_{63,145}$ with Herschel/PACS. Podio *et al.* (2012) could resolve the $[\text{OI}]_{63}$ emission line towards four more evolved Class II outflows. In this context, our new SOFIA observations of mainly Class 0 and Class I outflow sources help to evaluate the evolutionary role of the neutral outflow component traced by $[\text{OI}]_{63}$.

As a main result of this work, the majority of Class 0 outflows feature a dominant molecular component. On the contrary, Class I outflows are predominantly atomic, that is the bulk mass-loss resides in the component traced by $[\text{OI}]_{63}$. Our results support the frequently stated hypothesis, that protostellar outflows evolve as their respective driving source goes through the stages of evolution. As the driving source evolves from a Class 0 to a Class II object the corresponding outflow becomes by tendency hotter, and thinner and faster.

Acknowledgments

The Universe is under no obligation to make sense to you.

Neil deGrasse Tyson



First and foremost I am extremely grateful to my supervisor Dr. Jochen Eislöffel for his invaluable guidance throughout my PhD journey. At any time I could rely on his help and on his profound expertise. He always had the gift of encouraging me, especially when I was close to desperation. I am not exaggerating when I say that Jochen is a true mine of information and his strong commitment to research made a huge impression on me. For that and much more I thank you, Jochen!

I convey my sincere gratitude to Dr. Brunella Nisini, Dr. Teresa Giannini, Dr. Christian Fischer, and Dr. Alfred Krabbe for their valuable scientific help and concise comments on my research work. Our correspondence has been extremely helpful for me in developing a deeper understanding of relevant technical and scientific aspects of our research field.

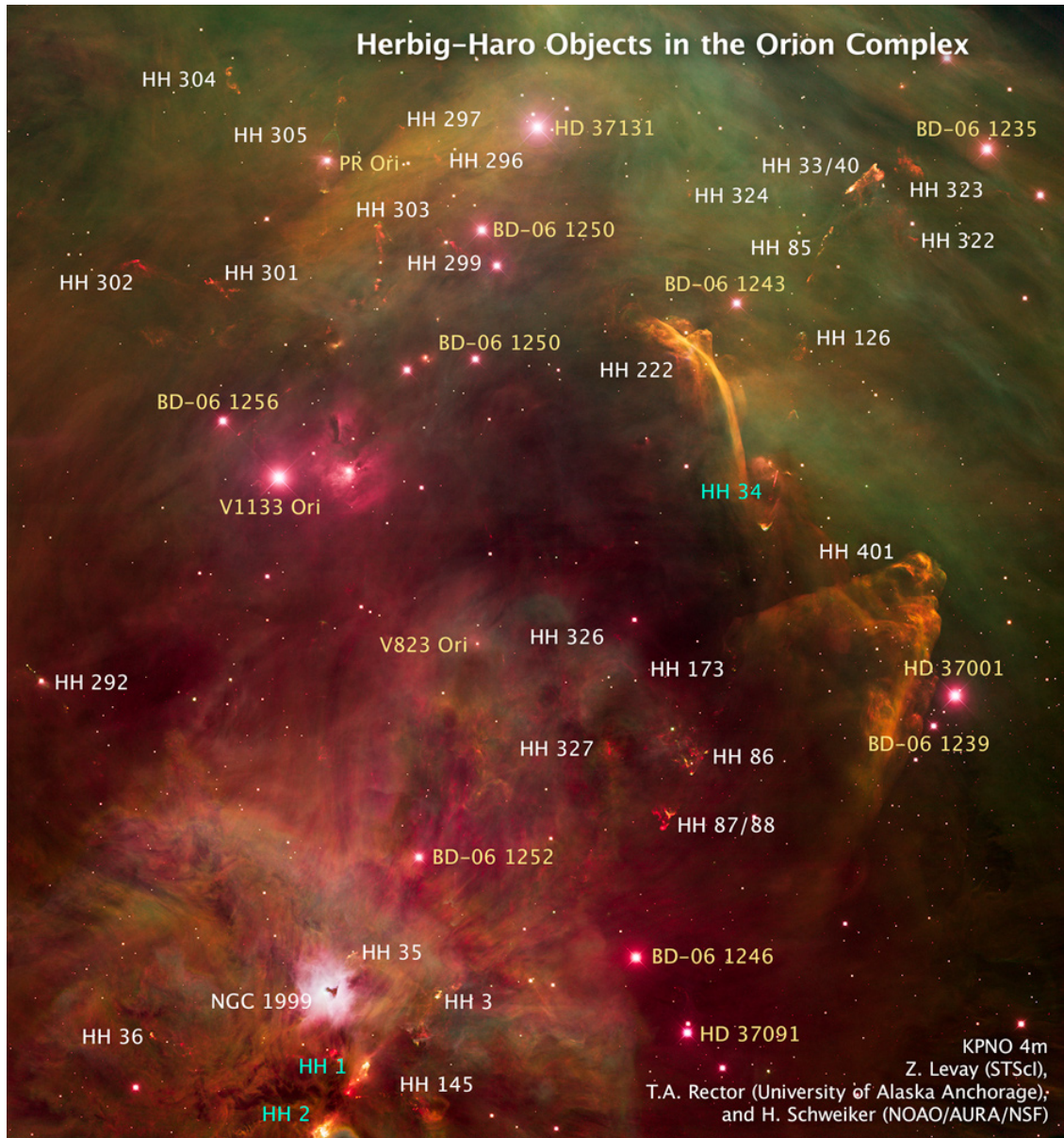
I thank the Director Dr. Artie Hatzes and Deputy Director Dr. Matthias Hoefft for their academic support at the Thüringer Landessternwarte Tautenburg (TLS). I sincerely thank the whole staff at TLS for being kind and ready to help at any time!

The star formation group at TLS consisting of Dr. Jochen Eislöffel, Dr. Bringfried Stecklum, Dr. Stanislav Melnikov, and Verena Wolf was like a small family to me and I am grateful that I was part of it.

I shall express my special thanks to many colleagues and friends who have accompanied me at TLS. I will miss chatting with you in the office or at the coffee break. You have contributed immensely to my personal and professional time at TLS: Dr. Alexander Drabent, Dr. Priyanka Chaturvedi, Dr. Mukul Mhaskey, Dr. Cosmos Dumba, Dr. Jakob Gelzinis, Sebastian Schmidl, Dr. Silvia Sabotta, Verena Wolf, Dr. Kamlesh Rajpurohit, David Wöckel, Dr. Sireesha Chamarthi, Dr. Priscilla Muheki, Dr. Michael Hartmann, Shubham Bhagat, Dr. Aritra Basu, Dr. Vijay Mahatma, Dr. Eleni Vardoulaki.

I am deeply thankful to my beloved family who has always supported me. Let me especially mention my mum and dad, my sister Katrin, my grandma Ursula, my uncles Harry and Horst, and aunt Irmchen. Thank you for your love and support!

The person who was always there for me within the last years was my girlfriend Rebekka. If something good happened to me, it wasn't real until I shared it with her.



Credits: Z. Levay (STScI), T.A. Rector (University of Alaska, Anchorage), and H. Schweiker (NOAO/AURA/NSF); Image from: <https://hubblesite.org/image/2868/news/25-stellar-jets>.

Contents

Zusammenfassung	iii
Abstract	v
Acknowledgments	vii
1 Introduction	1
1.1 Outflows in the Universe	1
1.2 Aims and structure of this thesis	4
2 Outflows from Young Stellar Objects (YSOs)	7
2.1 Fundamentals of shock physics	12
2.2 Classification scheme of Young Stellar Objects	16
2.3 Observations of protostellar outflows	18
2.4 The atomic outflow component traced by the far-infrared [O I] ₆₃ emission line	21
3 Observations with SOFIA	27
3.1 SOFIA's telescope, capabilities, and instruments	27
3.2 The Field Imaging Far-Infrared Line Spectrometer	30
3.3 The sample of nine protostellar outflows	33
4 Data Reduction	35
4.1 Mitigating the residual Earth atmosphere	35
4.2 Mass-loss rate measurements	41
4.2.1 Mass-loss rates from a shock model	42
4.2.2 Mass-loss rates from the jet luminosity in [O I] ₆₃	45
5 First fully mapped [O I] outflows with SOFIA	51
5.1 Morphology and schematics	51
5.1.1 Cep E	51
5.1.2 HH1	52
5.1.3 HH212	52
5.1.4 HH26	53
5.1.5 HH34	53
5.1.6 HH111	54

5.1.7	L1551 IRS5	55
5.1.8	SVS 13	55
5.1.9	HH 30	56
5.2	Line Detections	65
5.3	Flux and mass-loss rate measurements	71
5.4	Accretion rates	72
6	The evolutionary role of the atomic outflow component	77
6.1	Efficiencies of fully mapped Class 0/I outflow sources	77
6.2	Other outflow components	80
6.3	A comparison with outflows with unresolved mapping	82
7	Conclusions	89
	Bibliography	90
	Appendices	113
A	Accretion rates of Cep E and SVS 13	113
B	Detected continuum sources and their fluxes	115
C	Publications, Talks and accepted Proposals	125

List of Figures

1.1	Astrophysical outflows in the Universe.	1
2.1	A gallery of five iconic protostellar outflows.	8
2.2	The jet-launching zone.	9
2.3	1D planar steady shocks from two perspectives.	12
2.4	A schematic of the terminal working surface of a protostellar jet. . .	14
2.5	Classification scheme of YSOs.	17
2.6	Grotrian diagram for the O I system.	22
2.7	The theoretical $[\text{O I}]_{63}/[\text{O I}]_{145}$ line ratio.	24
3.1	The flying observatory SOFIA.	27
3.2	A transparent view on the centrepiece of the SOFIA observatory. .	28
3.3	The structural assembly.	28
3.4	The light guidance within the optical system.	28
3.5	SOFIA's instruments.	29
3.6	The two channels of FIFI-LS.	31
3.7	An illustration of a 3D FIFI-LS datacube.	32
4.1	SOFIA flight parameters.	35
4.2	Synthetic transmission curve of the Earth's atmosphere.	36
4.3	Expected signals from protostellar outflows in the $[\text{O I}]_{63}$ emission line.	39
4.4	Expected signals from protostellar outflows in the $[\text{O I}]_{145}$ emission line.	40
4.5	The cooling zone behind a shock.	43
4.6	A simple hydrodynamical outflow model.	46
4.7	The analytical solution of $n_2/n(\text{O})$ for five selected temperatures. . .	48
5.1	The continuum subtracted $[\text{O I}]_{63}$ map of Cep E.	57
5.2	The continuum subtracted $[\text{O I}]_{63}$ map of HH 1.	58
5.3	The continuum subtracted $[\text{O I}]_{63}$ map of HH 212.	59
5.4	The continuum subtracted $[\text{O I}]_{63}$ map of HH 26.	60
5.5	The continuum subtracted $[\text{O I}]_{63}$ map of HH 34.	61
5.6	The continuum subtracted $[\text{O I}]_{63}$ map of HH 111.	62
5.7	The continuum subtracted $[\text{O I}]_{63}$ map of L1551 IRS5.	63
5.8	The continuum subtracted $[\text{O I}]_{63}$ map of SVS 13.	64

5.9	Line detections towards Cep E.	66
5.10	Line detections towards HH 1.	67
5.11	Line detections towards HH 212.	67
5.12	Line detections towards HH 26.	68
5.13	Line detections towards HH 34.	68
5.14	Line detections towards HH 111.	69
5.15	Line detections towards L1551 IRS5.	69
5.16	Line detections towards SVS 13.	70
5.17	Line detections towards HH 30.	70
6.1	The $\dot{M}_{\text{out}}^{\text{lum}}(\text{[OI]})$ vs. \dot{M}_{acc} diagram for the extensively mapped out- flow sources.	79
6.2	The $\dot{M}_{\text{out}}^{\text{lum}}(\text{[OI]})$ vs. \dot{M}_{acc} diagram for the limitedly mapped outflow sources with a single Herschel/PACS footprint.	86
B.1	Continuum maps of Cep E.	116
B.2	Continuum maps of HH 1.	117
B.3	Continuum maps of HH 212.	118
B.4	Continuum maps of HH 26.	119
B.5	Continuum maps of HH 34.	120
B.6	Continuum maps of HH 111.	121
B.7	Continuum maps of L1551 IRS5.	122
B.8	Continuum maps of SVS 13.	123
B.9	Continuum maps of HH 30.	124

List of Tables

2.1	Characteristics of protostellar outflows.	10
2.2	Discontinuities for a 1D steady shock.	13
3.1	Protostellar outflows observed with SOFIA.	33
4.1	Chosen ATRAN parameters for the data reduction.	37
5.1	[O I] ₆₃ flux measurements towards the observed outflows.	71
5.2	Calculated mass-loss and accretion rates for the observed targets (Cep E, HH 1, HH 212, L1551 IRS5).	74
5.3	Calculated mass-loss and accretion rates for the observed targets (HH 26, HH 34, HH 111, SVS 13, HH 30).	75
6.1	Comparison of the capabilities of the SOFIA/FIFI-LS and the Her- schel/PACS instruments.	77
6.2	Mass-loss rates and accretion rates for other extensively mapped outflow sources.	78
6.3	Not extensively observed Class II outflow sources (GASPS survey).	83
6.4	Not extensively observed outflow sources (DIGIT, WILL, and WISH surveys).	84
6.5	Not extensively observed outflow sources (WILL survey).	85
B.1	Measured continuum fluxes of our objects at the observed [O I] transitions.	115

List of abbreviations

SOFIA	Stratospheric Observatory for Infrared Astronomy
FIFI-LS	Field-Imaging Far-Infrared Line Spectrometer
HST	Hubble Space Telescope
PACS	Photodetecting Array Camera and Spectrometer
FOV	Field of View
HH object	Herbig-Haro object
YSO	Young Stellar Object
SED	Spectral energy distribution
CTTSs	Classical T-Tauri stars
LTE	Local thermodynamical equilibrium
ISO	Infrared Space Observatory
STO	Stratospheric Terahertz Observatory
STO2	Stratospheric Terahertz Observatory 2
BLAST	Balloon-borne Large Aperture Submillimeter Telescope
FORCAST	Faint Object infraRED CAmera for the SOFIA Telescope
EXES	Echelon-Cross-Echelle Spectrograph
HIRMES	High-resolution Mid-infrared Spectrometer
GREAT	German REceiver for Astronomy at Terahertz Frequencies
HAWC+	High-resolution Airborne Wideband Camera Plus
FWHM	Full Width Half Maximum
ATRAN	Atmospheric transmission model
SIF	Spectral instrument function
PDR	Photodissociation region
HM89	Hollenbach and McKee (1989) shock model
WISH	Water in star-forming regions with Herschel
WILL	The William Herschel Line Legacy
DIGIT	Dust, Ice, and Gas In Time
GASPS	Gas Survey of Protoplanetary Systems

CHAPTER 1

Introduction

1.1 Outflows in the Universe

Jets and outflows appear almost everywhere in the Universe (Fig. 1.1). Typically, they are seen in form of highly collimated particle flows (jets), less-collimated bipolar lobes, quasi-spherical winds, or diffuse nebulosities. The scales of astrophysical jets are striking: solar coronal jets have lengths up to a few solar radii (Hanaoka *et al.* 2018), protostellar jets can extent up to a few parsecs (Frank *et al.* 2014), and the radio lobes associated with Hercules A (3C 348) in Fig. 1.1a have a spatial dimension of about 200 kpc or more (Sadun and Morrison 2002). This represents a span of 13 orders of magnitude in physical length. Astrophysical jets are indeed main protagonists on both stellar and galactic dimensions.

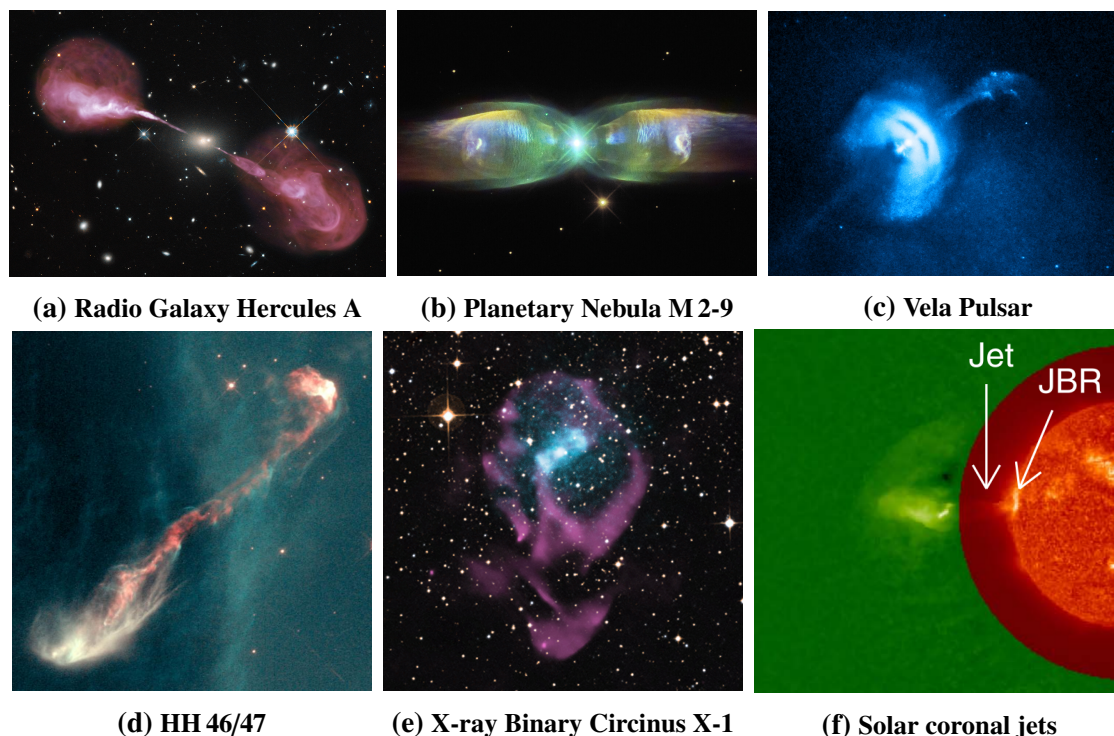


Fig. 1.1. Astrophysical outflows in the Universe. Credits: **a)** NASA, ESA, S. Baum and C. O’Dea, R. Perley and W. Cotton, and the Hubble Heritage Team; **b)** ESA/Hubble & NASA, Acknowledgement: Judy Schmidt; **c)** X-ray: NASA/CXC/Univ of Toronto/M.Durant *et al.*; Optical: DSS/Davide De Martin; **d)** NASA, ESA, and P. Hartigan; **e)** X-ray: NASA/CXC/Univ. of Wisconsin-Madison/S. Heinz *et al.*; Optical: DSS; Radio: CSIRO/ATNF/ATCA; **f)** Miao *et al.* (2018)

Surprisingly, astrophysical outflows are most often found in systems that feature three main ingredients: large-scale magnetic fields, intrinsic rotation, and accretion. It seems, that outflows are inevitably formed in such systems. It is therefore not entirely far-fetched to assume that one universal physical mechanism may drive these astrophysical outflows on all scales in the Universe.

Why study protostellar outflows?

Protostellar outflows are particularly interesting laboratories in the presented gallery of astrophysical jets. They are perfectly suited to study the still not fully understood accretion/ejection mechanism and shocks, since many bright protostellar outflows are located in our very neighbourhood (astronomically). An overview of some of the most pressing questions about protostellar outflows is listed in Günther *et al.* (2019).

The most spectacular known outflows from young protostars are at a distance of about $\sim 140\text{--}750$ pc within huge star forming regions such as Taurus, the Orion Nebula, or the Cepheus region. Therefore, protostellar outflows can principally be traced back to the innermost interaction region by means of observations at high angular resolution in the visible or near-infrared (e.g. the Subaru Telescope atop Mauna Kea, the Hubble Space Telescope [HST], the UK Infrared Telescope [UKIRT], the Large Binocular Telescope [LBT]), or even towards millimetre (and even longer) wavelengths with the Very Large Array (VLA), the Atacama Large Millimeter/Submillimeter Array (ALMA), or the Low Frequency Array (LOFAR). The launch of the James Webb Space Telescope (JWST) is eagerly awaited and there will be a number of guaranteed time programs devoted to observing protostellar outflows (Ray and Ferreira 2020).

So far, only a few outflows have been extensively studied in the far-infrared ($\lambda \sim 25\text{--}1\,000$ μm or $\nu \sim 12\,000\text{--}300$ GHz) part of the electromagnetic spectrum with Herschel/PACS or ISO. At these wavelengths extinction plays a minor role, so that we can in principle observe deeply embedded objects such as forming stars and their outflows. There are other reasons, however, to study protostellar outflows at these wavelengths that are not accessible from the ground.

The far-infrared Universe

Observations towards the Galactic Plane reveal that significantly more than 90 % of detectable radiant energy falls within the far-infrared region of the electromagnetic spectrum (Planck Collaboration *et al.* 2015). This finding is not surprising at all. Apart from some *hot islands* (the stars) the universe is very cold and dusty. The most prominent cooling lines of the interstellar medium arise in the far-infrared:

[C II]₁₅₈, [O I]_{63,145}, [N II]₁₂₂, [N III]₅₇, [O III]_{52,88} (e.g. Malhotra *et al.* 2001; Osterbrock and Ferland 2006).¹ In this set, the two emission lines of atomic oxygen ([O I]_{63,145}) are particularly interesting as they are expected to provide insightful information about the shocks associated with protostellar outflows. Ultimately, such observations will help us to understand the physics of star and planet formation as they are connected with each other.

¹**Notation:** Forbidden transitions are standardly labelled by square brackets (e.g. Tennyson 2019). The degree of ionisation of an atom is indicated with Roman numerals (I for neutral, II for singly ionised, and III for doubly ionised, etc.). We mark the wavelength in μm of the corresponding transition as subscript, that is e.g. [C II]₁₅₈ is short for the forbidden emission line of singly ionised carbon C⁺ at $\lambda = 157.7 \mu\text{m}$.

1.2 Aims and structure of this thesis

The main goal of this work is to map several well-studied protostellar outflows in the far-infrared transitions of atomic oxygen at $63.18\ \mu\text{m}$ and $145.53\ \mu\text{m}$ (short: $[\text{OI}]_{63}$ and $[\text{OI}]_{145}$). These maps will enable us to study the importance of the warm ($T \sim 500\text{--}5\,000\ \text{K}$), neutral outflow component in the earliest stages of protostellar evolution, namely towards Class 0/I outflow sources (i.e., Figure 2.5).

The $[\text{OI}]_{63}$ emission line is expected to be directly connected to shock excited gas in a dissociative J-shock and comparably bright amongst other shock tracers. As a result, measurements of the instantaneous mass-loss rate \dot{M}_{out} in the outflow become potentially possible. Together with estimates on their accretion rates \dot{M}_{acc} , the efficiency of the outflow, that is the ratio between the mass-loss in the outflow and the mass accretion onto the source, can be evaluated and compared with model predictions.

Until now, only a few protostellar outflow sources have been extensively mapped in $[\text{OI}]_{63}$. Nisini *et al.* (2015) used the Herschel/PACS instrument to study five mainly Class 0 outflows. Podio *et al.* (2012) could resolve the $[\text{OI}]_{63}$ emission line towards four more evolved Class II sources. This leaves a gap of understanding in the significance of the neutral gas component traced by $[\text{OI}]_{63}$ towards Class I sources. The role of this outflow component in the evolutionary scheme of outflows from Class 0 over Class I to Class II sources is still pending. In this context, we wish to obtain more insight into the evolutionary role of the atomic component in protostellar outflows with our new observations.

In order to tackle the stated objectives we structure this thesis as follows:

- Chapter 2 comprises a brief introduction to selected aspects of protostellar outflows, e.g. the basic physical parameters of outflows, the connection to shocks and their role in the theory of star formation. In addition, the physical origin of the forbidden $[\text{OI}]_{63}$ line emission is discussed to better understand the underlying physical conditions of $[\text{OI}]$ emitting outflow regions.
- In Chapter 3 we briefly describe some relevant technical details of the used telescope (SOFIA) and instrument (FIFI-LS) for our observations. As part of this thesis nine protostellar outflows have been mapped in both far-infrared $[\text{OI}]$ transitions along the outflow direction close to their respective driving source. Sorted by age they are:

Class 0: Cep E, HH 1, HH 212

Class I: HH 26, HH 34, HH 111, L1551 IRS5, SVS 13

Class I/II: HH 30

- A challenging part of this study was to mitigate the residual effects of the Earth’s atmosphere from the obtained SOFIA/FIFI-LS data. We describe the details of our own written data reduction pipeline *JENA.py*, that does this job quite effectively, in Chapter 4.

We propose two different techniques to derive mass-loss rates \dot{M}_{out} from the $[\text{O I}]_{63}$ line luminosity. The first method was newly derived in this study (Sperling *et al.* 2020) and utilises the jet geometry and jet luminosity. The second method exploits a numerical result of the shock model proposed by Hollenbach and McKee (1989). Both methods and their underlying assumptions are described in detail in Section 4.2.

- We present the continuum subtracted $[\text{O I}]_{63}$ maps of the nine observed outflows in Chapter 5 together with a schematic interpretation of the detected emission. Some exemplary spaxels (spatial pixels) demonstrate the $[\text{O I}]_{63}$ line detection towards relevant outflow regions. Mass-loss rates from both methods are evaluated and compared with other outflow components. Furthermore, we compile a set of similarly observed outflows to study the outflow efficiency for these fully $[\text{O I}]_{63}$ mapped outflow sources.
- In Chapter 6 we compare our results of the fully mapped outflow sources with outflows that have been mapped only to a limited extent in $[\text{O I}]_{63}$ (spatially unresolved) with a single footprint of Herschel/PACS.

This work is based on the publications Sperling *et al.* (2020) and Sperling *et al.* 2021 written by the author under the supervision of Jochen Eislöffel. This work has been supported by the German Verbundforschung grant 50OR1717 to J.E.

CHAPTER 2

Outflows from Young Stellar Objects (YSOs)

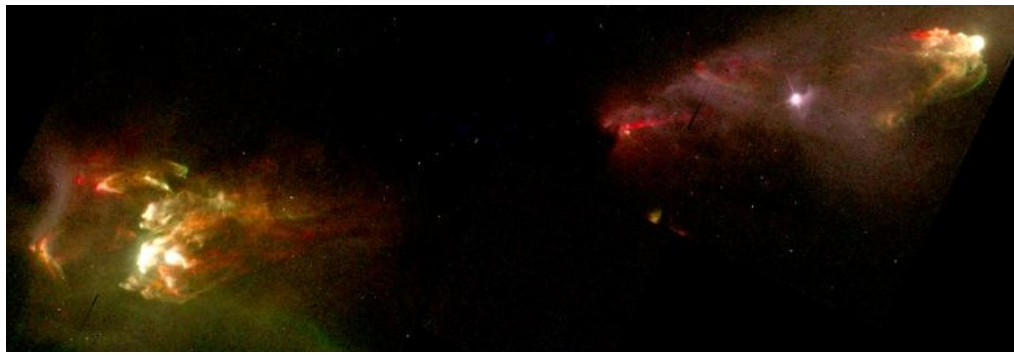
Historic Notes

Nowadays it is clear, that protostellar jets are an integral part of star formation (e.g. Bodenheimer 2011; McKee and Ostriker 2007). However, their discovery came with great astonishment as outflows had not been predicted by theory. In-falling material was expected to be seen towards young forming stars. Instead supersonic, outflowing gas and plasma in the form of bipolar lobes were observed (Snell *et al.* 1980).

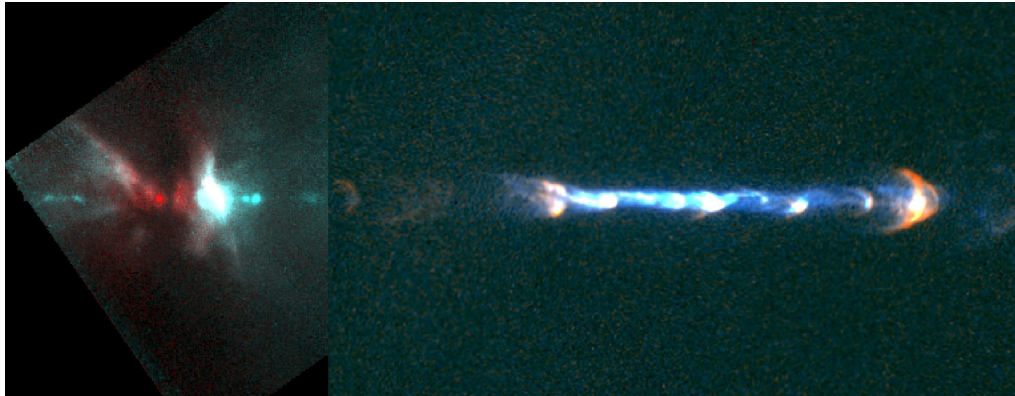
The history of protostellar outflows may be traced back about 70 years ago (see review Reipurth and Heathcote 1997). Haro (1952) and Herbig (1951) discovered several mysterious *faint nebulosities* in dark clouds. These emission-line nebulae showed very peculiar spectra when compared to HII regions. Later it turned out that these emission regions are shock excited material powered by an outflow from a young star (Schwartz 1975, 1978). They form a separate class of astrophysical objects – the Herbig-Haro objects (short: HH objects). HH objects can be detected in optical emission lines and are comparably small (20''–50''). Until now more than one thousand Herbig-Haro objects are known (e.g. Reipurth 2000; Smith *et al.* 2010; Walawender *et al.* 2005) and many of them are associated with highly-collimated jets. HH objects are labelled by an individual natural number starting with HH 1, HH 2, HH 3, and so on – listed approximately in ascending order of their recognition (Herbig 1974).

The Hall of Fame of protostellar outflows

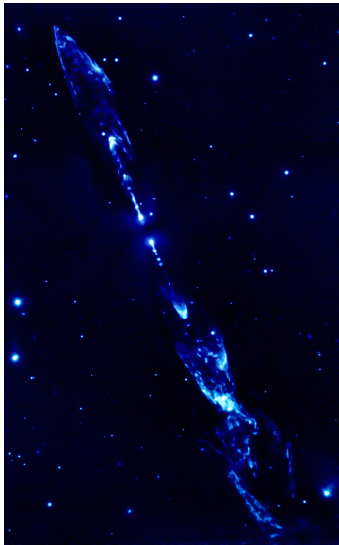
Over the past decades several bright outflows have been studied extensively throughout the spectral range. A gallery of five such *iconic* objects is depicted in Fig. 2.1. All the quoted HH objects and a few more have been mapped for the first time in the far-infrared [OI] transitions as main part of this thesis. But before we address the question of *What can we learn from such observations?*, some physical basics have to be introduced.



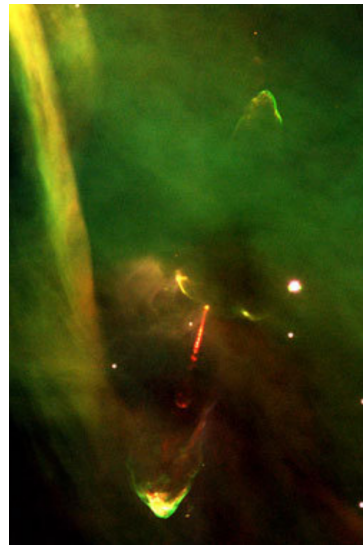
(a) HH 1/2



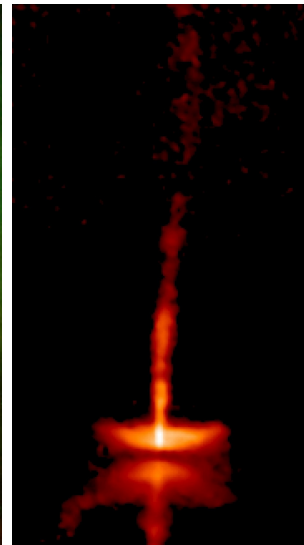
(b) HH 111



(c) HH 212



(d) HH 34



(e) HH 30

Fig. 2.1. A gallery of five iconic protostellar outflows. **HH 1/2:** Color representations of HST/WFPC2 images towards the HH 1/2 complex (Hester *et al.* 1998), $H\alpha$ (green), [S II] (red), line-subtracted F702W continuum frame (blue); **HH 111:** A mosaic observed with the HST (Reipurth *et al.* 1999). *Left:* Infrared NICMOS images taken in the two filters F160W (turquoise) and F205W (red) transmitting the near-infrared [Fe II] and H_2 emission lines, respectively. *Right:* Optical WFPC2 images ([S II] blue and $H\alpha$ orange); **HH 212:** ISAAC observations in the near-infrared H_2 transition (McCaughrean *et al.* 2002); **HH 34:** Optical three-color composite image taken with VLT/FORS2: B Band (blue), $H\alpha$ (green), [S II] (red), Credit: ESO, <https://www.eso.org/public/images/eso9948b/>; **HH 30:** Optical R Band image taken with HST (WFPC2), Credits: NASA, Alan Watson, Karl Stapelfeldt, John Krist and Chris Burrows, <https://hubblesite.org/image/998/news/25-stellar-jets>;

Origin of bipolar outflows

Protostellar outflows are driven by young still forming stars – so-called proto-stars. A lot of questions concerning the launching process itself, the actual launching region, or the collimation mechanism of protostellar outflows are still under debate (Frank *et al.* 2014).

Our current understanding is that jets are launched within a few astronomical units of the forming protostar by magnetic fields through magneto-centrifugal acceleration (e.g. Blandford and Payne 1982; Camenzind 1990; Pudritz *et al.* 2007; Pudritz and Ray 2019; Ray and Ferreira 2020). Two main jet-launching theories have been put forward (see e.g. Ferreira *et al.* 2006): the X-wind scenario of Shu *et al.* (1994) and Shu *et al.* (1988, 2000), and the disk wind model of Casse and Ferreira (2000) and Ferreira (1997).

Simply put, in the X-wind model the outflow originates from a small disk annulus at the so-called magnetic X-point, that is the co-rotation radius of the disk and the protostar. In contrast, in the disk wind model the outflow is launched from the disk as an extended wind. In order to get a rough idea of the jet launching process we refer to Figure 2.2. However, spatially resolving the launching region with conventional telescopes is out of reach. To illustrate this point, a launching region of 5 au in diameter at 140 pc distance (corresponding to the nearest star forming regions such as Taurus) would correspond to an angular distance of $\theta \approx 0.06''$.

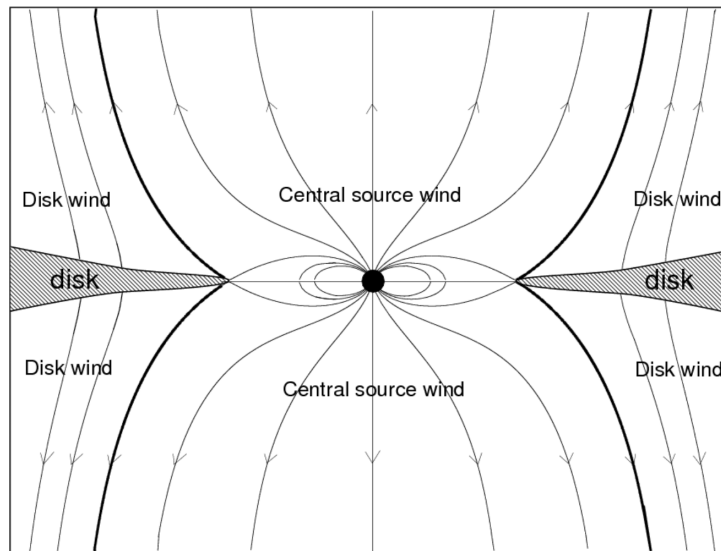


Fig. 2.2. An illustration of the jet-launching process. Taken from (Tsinganos 2010).

Both models predict that the mass-outflow rate \dot{M}_{out} scales with the accretion rate \dot{M}_{acc} . Efficiency ratios of $\dot{M}_{\text{out}}/\dot{M}_{\text{acc}} \sim 0.3$ are predicted in the X-wind scenario, whereas $\dot{M}_{\text{out}}/\dot{M}_{\text{acc}} \sim 0.01\text{--}0.5$ is implied in the disk wind scenario. Thus, reliable

measurements on both quantities (\dot{M}_{out} , \dot{M}_{acc}) may provide decisive information on the proposed jet acceleration mechanisms. Further clues about the launching mechanism may be obtained by measuring the jet rotation (Pudritz and Ray 2019).

Protostellar outflows in numbers

Orders of magnitude are important to understand a given physical system.¹ We therefore compile a set of physical quantities that broadly characterise protostellar jets and outflows. The stated numbers are taken from Bally (2016), Frank *et al.* (2014), Ray (2007), and Ray and Ferreira (2020) and illustrate the environmental conditions at these outflows. What we learn from these numbers is that protostellar outflows must be complex, feature-rich physical entities, since a wide parameter space is covered. The actual measurements of these quantities can be quite challenging and large uncertainties may be associated with them.

Characteristics of protostellar outflows

Physical lengths:	$l \lesssim 10^{17}$ m (up to a few parsecs)
Gas velocities:	$v_{\text{out}} \sim 100\text{--}1000$ km s ⁻¹ ($v_{\text{out}} \sim v_{\text{esc}}^{\text{a}}$)
Particle densities:	$n \sim 10^2\text{--}10^6$ cm ⁻³ ($n_{\text{air}}^{\text{b}} \sim 10^{19}$ cm ⁻³)
Temperatures:	$T \sim 10^2\text{--}10^6$ K
Ionisation fractions:	$x_e \gtrsim 1\text{--}10$ %
Mach numbers:	$\mathcal{M} \sim 20\text{--}100$ (supersonic jets)
Mass-loss rates:	$\dot{M}_{\text{out}} \sim 10^{-9}\text{--}10^{-5}$ M_{\odot} yr ⁻¹ ($\dot{M}_{\text{out},\odot}^{\text{c}} \sim 10^{-14}$ M_{\odot} yr ⁻¹)
Magnetic field strengths:	$B \sim 20\text{--}500$ μG ($B_{\oplus}^{\text{d}} \sim 0.5$ G)
Collimation angle:	$\theta \sim 5^{\circ}$ (for highly collimated jets)
Dynamical time scales:	$\tau_{\text{dyn}} \sim 10^3\text{--}10^6$ yr
Mechanical force:	$F \sim 10^{-6}\text{--}10^{-1}$ M_{\odot} yr ⁻¹ km s ⁻¹
Viscous Reynolds number:	$Re \sim 10^6$
Magnetic Reynolds number:	$Re_M \sim 200\text{--}500$

Tab. 2.1. ^a v_{esc} as escape velocity, ^b n_{air} as density of air, ^c $\dot{M}_{\text{out},\odot}$ as mass-loss rate of the sun (solar wind), ^d B_{\oplus} as Earth's magnetic field strength (at its surface).

¹ see e.g. the online lecture notes: *Order-of-Magnitude Physics: Understanding the World with Dimensional Analysis, Educated Guesswork, and White Lies*; Peter Goldreich, Sanjoy Mahajan, Sterl Phinney; <http://www.inference.org.uk/sanjoy/oom/book-letter.pdf>

The role of outflows in the theory of star formation

The significance of protostellar outflows may be illustrated by two main factors (compiled from Bally 2016; Bodenheimer 2011; Frank *et al.* 2014; McKee and Ostriker 2007):

A Feedback: Outflows of parsec-scale dimensions clearly feed back material into their surrounding cloud and other nearby star forming regions. The interaction of outflows with the ambient medium induces turbulence, which in turn has a huge influence on the star formation efficiency. Indeed, surprisingly low star formation efficiencies are being observed in the Milky Way. It turns out that the three usually invoked components (gravity, magnetic fields, turbulence) are simply not enough to fully explain that – jets may play a fundamental role here.

Furthermore, outflows fundamentally change the local environment of the protostar/disk system by removing mass and energy, changing the chemical composition, and clearing away the infalling envelope. Ultimately, this determines the range of stellar masses once the protostar has reached the main sequence.

A potential impact on planet formation cannot be ruled out, since the outflow dynamically interacts with the disk where protoplanets are forming.

B Angular momentum: Protostars and their associated accretion disk somehow have to get rid of excess angular momentum during the collapse, otherwise a compact object such as a star at the centre would not form at all. In this regard, outflows are potentially the main agents removing this angular momentum and therefore allowing accretion to occur – without them stars and (exo-)planets as we know it would probably not exist.

Protostellar outflows as shock laboratories

Protostellar outflows are prominently detected in various emission lines (Fig. 2.1). In the optical most favorable lines are [OI] λ 6300, [SII] λ 6716, 6731, and H α , whereas in the near-infrared jets are often visible in [Fe II] at 1.64 μ m or in H $_2$ at 2.12 μ m. An analysis of emission line spectra towards Herbig-Haro objects allowed only one conclusion: these emission lines originate from cooling zones behind shocks (e.g. Schwartz 1977). Conclusively, protostellar outflows are perfect laboratories to test our understanding of shock physics.

2.1 Fundamentals of shock physics

What is a shock?

Shocks inevitably occur when protostellar jets impact an obstacle such as the ambient medium at high velocities (see review Draine and McKee 1993). Basically, there are two ways of how a gas might react to such an external disturbance. If the imposed perturbation is small the mathematical equations describing the physical situation can be linearised. In this case a standard wave equation with $c_s = \sqrt{\gamma k_B T / \mu m_H}$ as adiabatic sound speed describes the resulting propagation of the disturbance in the medium. On the contrary, if the disturbance is too violent and abrupt the discontinuity – now called *shock* – moves through the gaseous medium with supersonic velocity ($v_s > c_s$).

Jump-shock vs. Continuous-shock

There are two broad shock types: Jump-shocks and Continuous-shocks (short: J-shocks and C-shocks, Hollenbach 1997). We start with a brief introduction of J-shocks (e.g. Hollenbach and McKee 1989). Both interacting gases (outflow and the ambient medium) are described by a set of non-linear, three-dimensional, coupled partial differential equations in the framework of fluid dynamics. In the most simplified version the shock is modeled in the absence of magnetic fields as a planar, stationary, one-dimensional shock (Fig. 2.3).

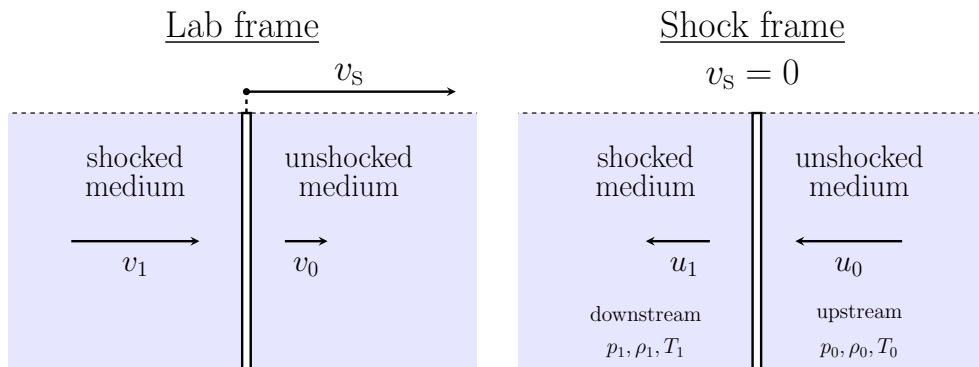


Fig. 2.3. A shock from two perspectives (adapted from Dyson and Williams 1997). In the observers frame of reference (left) the shock passes with the shock velocity v_s . The same situation can be described in the frame of reference where the shock is stationary (right). The transition from one system to another that is done by a Galilean transformation, that is $u_0 = v_0 - v_s \approx -v_s$ and $u_1 = v_1 - v_s$.

Conservation laws dictate the physical properties such as the densities ρ , pressures p , temperatures T , and gas velocities u in the upstream and downstream zones of the shock. The Rankine–Hugoniot jump conditions prevail and impli-

cate that these quantities abruptly change in a very thin layer as the shock moves through the gas (Tab. 2.2). These shocks are therefore called *Jump*-shocks.

In the limit of a strong shock (high involved upstream Mach numbers, that is $\mathcal{M}_0 = u_0/c_s \gg 1$) the density increases and the velocity decreases by the same factor of four behind the shock. Expectedly, pressure and temperature increase depending on the involved shock velocity v_s . The increase in temperature behind the shock involves an irreversible conversion of kinetic energy of the flowing particles into thermal energy of the shock-heated gas. Consequently, there occurs a jump in specific entropy ($\Delta s > 0$) across the shock. The thickness of the discontinuity is mainly determined by viscosity and thermal conduction. Ultimately, the shock-excited gas behind the shock front forms a radiative cooling zone.

Discontinuities for a 1D (planar) steady shock with the Rankine–Hugoniot jump conditions and no magnetic fields.

Property	upstream/downstream ratio	strong shock limit $\mathcal{M}_0 \rightarrow \infty, \gamma = 5/3$
Density	$\left(\frac{\rho_0}{\rho_1}\right) = \frac{(\gamma-1)\mathcal{M}_0^2+2}{(\gamma+1)\mathcal{M}_0^2}$	$\rho_1 = 4\rho_0$
Velocity	$\left(\frac{u_0}{u_1}\right) = \frac{(\gamma+1)\mathcal{M}_0^2}{(\gamma-1)\mathcal{M}_0^2+2}$	$u_1 = \frac{1}{4}u_0$
Pressure	$\left(\frac{p_0}{p_1}\right) = \frac{\gamma+1}{2\gamma\mathcal{M}_0^2-\gamma+1}$	$p_1 = \frac{3}{4}\rho_0 u_0^2$
Temperature	$\left(\frac{T_0}{T_1}\right) = \frac{(\gamma+1)^2\mathcal{M}_0^2}{(2\gamma\mathcal{M}_0^2-\gamma+1)((\gamma-1)\mathcal{M}_0^2+2)}$	$T_1 = \frac{3}{16} \frac{\mu m_H}{k_B} u_0^2$

Tab. 2.2. Notations: $\gamma = C_p/C_V$ as ratio between the specific heats at constant pressure and at constant volume ($\gamma = 5/3$ for mono-atomic gas), μ as the mean molecular mass (about 0.7 for fully ionised, 1.5 for atomic, and 2.7 for molecular gas), m_H as the hydrogen mass, k_B as the Boltzmann constant. The other quantities are introduced in Fig. 2.3.

The presence of a transverse magnetic field may moderate the stated compressions across the shock (e.g. Draine 1980; Draine *et al.* 1983). In this case, additional terms in the Rankine–Hugoniot jump conditions have to be included describing the upstream and downstream magnetic field strengths and directions. Taking into account magnetic fields severely complicates the model, since e.g. the degree of ionisation becomes important and different types of waves in a magnetic fluid (e.g. Alfvén waves) have to be considered (Lequeux 2005). Qualitatively, the magnetic field is well coupled with the interstellar medium (*freezing-in condition*), so that the occurring gas compression produces a compression of the magnetic field lines. If the discontinuity can be suppressed, i.e. smoothed out over a large region, by the presence of magnetic fields the occurring shocks are called *Continuous*-shocks.

In principle, both shock types can be strong enough to dissociate molecules, when the temperature behind the shock exceeds a few thousand degrees. In this case the shock is called *dissociative*, otherwise *non-dissociative*. J-shocks featuring shock velocities of $v_s \sim 30\text{--}50 \text{ km s}^{-1}$ are mostly dissociative (Kwan *et al.* 1977), whereas C-shocks are generally non-dissociative with their lower shock velocities $v_s \lesssim 40 \text{ km s}^{-1}$ (Draine *et al.* 1983; Smith and Brand 1990). The shocks produced in astrophysical jets are expected to be initially of J-shock type and may become of C-type as time advances (e.g. Flower and Pineau Des Forêts 2010). Generally, J-shocks and C-shocks mainly differ in their overall structure, chemistry, involved shock velocities, and above all in their expected emission line spectra (Draine and McKee 1993). However, due to the complex shock structures in Herbig-Haro objects it is expected that both shock types coexist and a reasonable question might rather be, which shock type dominates in a given emitting region.

Jets and their shocks

The described 1D-shock model is clearly an oversimplification of the real physical situation when the primary jet hits the ambient medium. An illustration of the terminal working surface, that is where the supersonic flow hits the ambient medium, is depicted in Fig. 2.4.

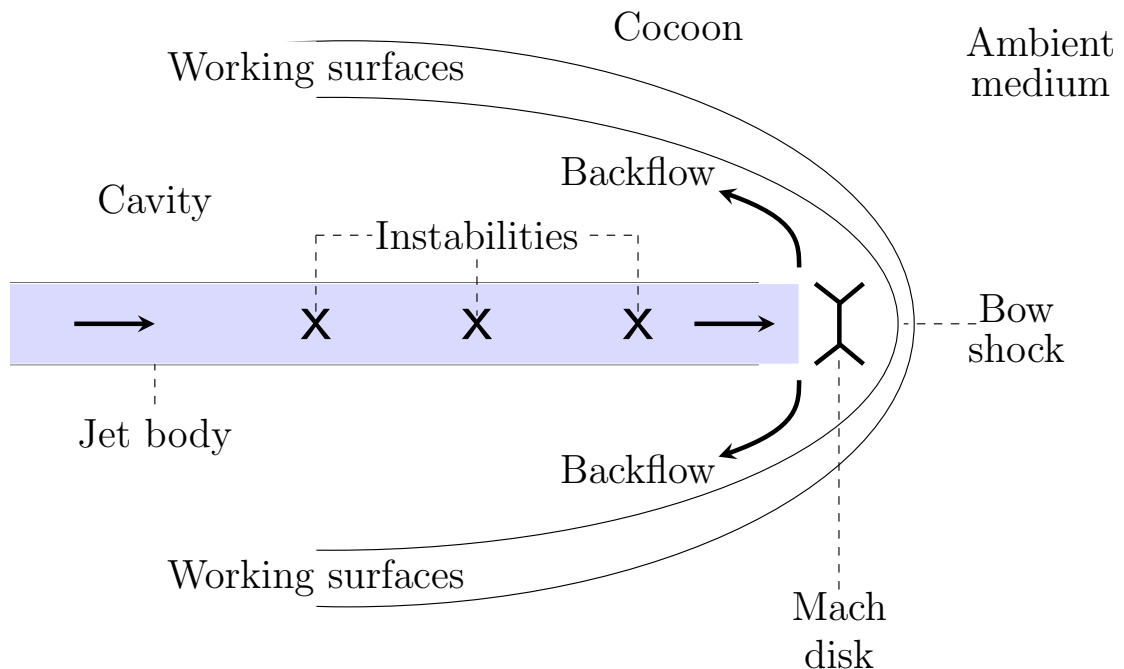


Fig. 2.4. An illustration of the terminal working surface of a protostellar jet. Adapted from several cartoons of different authors: e.g. Bührke *et al.* (1988), Hartigan (1989), Norman (1996), and Stanke (2001).

Locally, two shocks are occurring there: a forward shock that accelerates the material and a reverse shock that decelerates the supersonic flow (e.g. Hartigan 1989). Apart from that, it is expected (e.g. Norman 1996; Norman and Winkler 1985) that five global structures form: a cocoon that surrounds the beam of the jet, a leading bow shock at the head of jet, a Mach disk, a cooling zone behind the shock, and instabilities/turbulences.

Protostellar jets are *underexpanded*, since their internal pressure inside the jet is higher than the pressure in the external medium. In turn, pressure imbalances can produce a compression shock perpendicular to the jet flow – the X-shaped Mach disk. A bow shock is a curved shock that forms at the terminal working surface where the jet hits the ambient medium. Backflowing material may be set in motion in a bow shock. At the boundary between the jet and the surrounding medium shear-instabilities may occur. In general, there are many instabilities involved at the same time (see review Reipurth and Bally 2001): hydrodynamic (e.g. Bührke *et al.* 1988; Micono *et al.* 1998), thermal (e.g. de Gouveia dal Pino and Opher 1990), and magneto-hydrodynamic (e.g. Cerqueira and de Gouveia Dal Pino 1999). The production of knots towards protostellar jets (e.g. HH 30, HH 34, HH 111) may be explained by these mechanisms. Alternatively, time-variability in the ejection process (e.g. Raga *et al.* 1990) may provide a competing theory of the appearance of knots in the collimated flow.

The cooling zone behind the shock can be much more extended than the actual shock front. Here, the shocked gas emits radiation in the form of forbidden lines and recombination lines and cools down.

Simulations and experiments

Apart from direct observations, protostellar jets can also be studied via numerical MHD simulations (e.g. Clarke 1996; de Gouveia dal Pino and Benz 1993; Norman *et al.* 1982; Rosen and Smith 2004; Stone and Norman 1992) or scaled laboratory experiments (e.g. Ciardi *et al.* 2007; Ciardi *et al.* 2009; Lebedev *et al.* 2005).

2.2 Classification scheme of Young Stellar Objects

Protostars are not stars yet

Main sequence stars are conventionally classified by their spectra that naturally provide information about their photosphere (e.g. Gray and Corbally 2009). Not surprisingly, a similar classification scheme for Young Stellar Objects (YSOs) has proven unsuccessful, since their evolutionary status and not their still forming, highly obscured photosphere is the determining factor in describing their physics. Conceptually, as YSOs evolve with time they accrete more and more material from their dusty envelope, develop outflows, and form disks until most surrounding material has been dissipated. It seems natural to utilise the infrared excess in the spectral energy distribution (SED) of the protostar as an evolutionary indicator, since it is a function of the amount of the circumstellar material. The infrared excess is defined as an excess of the (proto-)stellar infrared emission with respect to a pure blackbody spectrum. Physically, dust particles in the envelope and the forming disk absorb almost all radiation from the protostar and re-radiate this energy in the infrared. Following this premise, the shape of the SED is expected to evolve as the YSO evolves (e.g. Adams *et al.* 1987).

Five SED-Classes

YSOs are empirically divided into five classes based on the slope α_{IR} of the SED between the near-infrared and the mid-infrared (Andre *et al.* 1993; Greene *et al.* 1994; Lada 1987), that is

$$\alpha_{\text{IR}} = \frac{d \log \lambda F_{\lambda}}{d \log \lambda} \quad \text{with} \quad \lambda \approx 2\text{--}25 \mu\text{m}. \quad (2.1)$$

In the earliest evolutionary phase the newly formed protostar lies heavily obscured in its cold, natal cloud featuring no optical or near-infrared emission (Class 0, α_{IR} undefined). At this stage the protostar accretes the bulk part of its final mass and commonly shows strong outflow activity. Lifetimes of Class 0 sources are on the order of $\tau_{\text{life}} \sim 10^4$ yr (Andre *et al.* 2000). In the consecutive Class I phase ($\alpha_{\text{IR}} > 0.3$), the protostar is still embedded in a dusty envelope but becomes visible in the near-infrared. Class I sources ($\tau_{\text{life}} \sim 10^5$ yr, Evans *et al.* 2009) are surrounded by both a disk and an infalling envelope. It is speculated that planet formation potentially onsets already at this early evolutionary stage (see Tychoniec *et al.* 2020, and references therein).

SED-Flat sources feature $-0.3 < \alpha_{\text{IR}} < 0.3$ and their nature in the evolutionary sequence has yet to be clarified (Dunham *et al.* 2014). The more evolved Class II

($-1.6 < \alpha_{\text{IR}} < -0.3$) and Class III sources ($\alpha_{\text{IR}} < -1.6$) have already lost most parts of their dense envelopes and are therefore best described as star/disk systems. However, with lifetimes on the order of $\tau_{\text{life}} \sim 10^6\text{--}10^7$ yr (Palla and Stahler 1999) these sources are still far from reaching the zero-age main-sequence. The Class II and Class III sources are also referred to as classical T-Tauri stars (CTTSs) and weak-lined T-Tauri stars, respectively.

Other physical quantities such as the bolometric temperature T_{bol} or the ratio of specific luminosities ($L_{\text{smm}}/L_{\text{bol}}$) may be used as additional observational criteria to classify protostars (Andre *et al.* 1993; Chen *et al.* 1995; Myers and Ladd 1993). However, Robitaille *et al.* (2006) pointed out that there is a distinction between the SED class (observationally defined) and the evolutionary stage (from theory) of a protostellar object. Due to geometric effects (e.g. inclination, aspherical geometry) both do not necessarily have to match (e.g. Masunaga and Inutsuka 2000). With this in mind, we illustrate the different stages of star formation in Figure 2.5 in a simplified version.

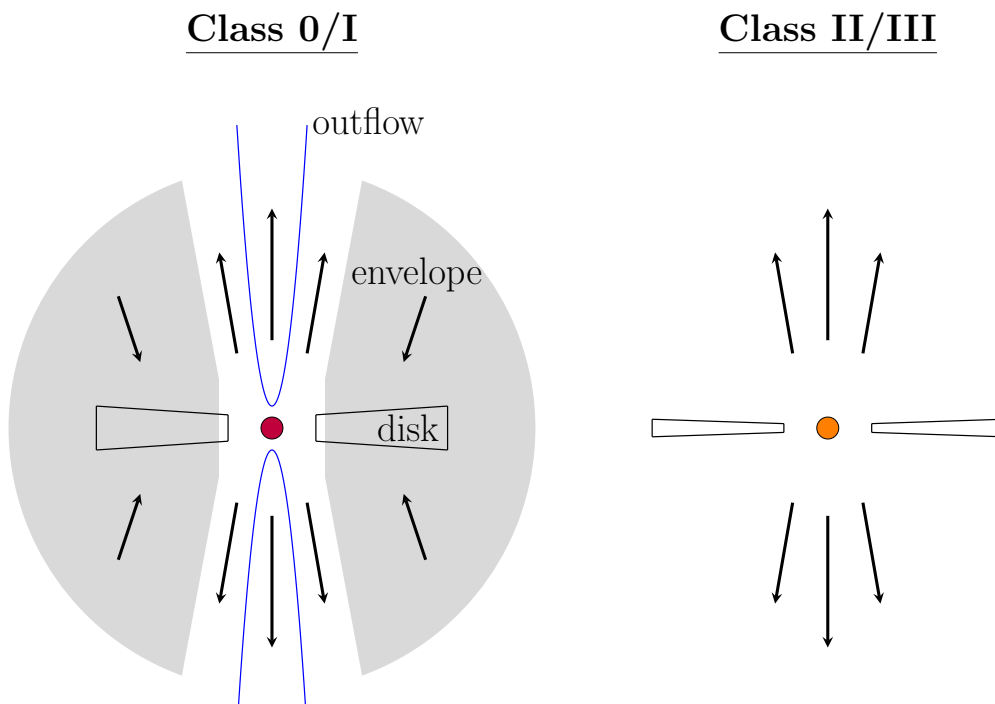


Fig. 2.5. The earliest stages of protostellar evolution. Adapted from Armitage (2015).

Unfortunately, a comparable evolutionary scheme of protostellar outflows is still pending. However, it seems obvious that the evolutionary state of the driving source of the outflow may provide most promising insights towards such theory, since both are physically connected to each other. So far, only a handful of studies have been investigating the idea of an evolution of protostellar outflows (Ellerbroek *et al.* 2013; Mottram *et al.* 2017; Nisini *et al.* 2015; Watson *et al.* 2016). In this context, observations at well-chosen emission lines might be very insightful (see Section 2.3).

2.3 Observations of protostellar outflows

Outflows from YSOs in form of collimated jets or poorly-collimated winds are commonly observed a) throughout the spectral range from radio to X-ray wavelengths, b) towards all early SED Classes, and c) over the entire mass range from brown dwarfs to massive young stars (see reviews Bally 2016; Frank *et al.* 2014; Reipurth and Bally 2001). It is widely believed that all low-mass protostars go through an outflow phase along with an accretion phase.

In general, protostellar outflows are being traced by certain emission lines (ionic, atomic, molecular) that are believed to emerge from shock excited or swept-up material due to the outflow. So far, only in a few cases has radio synchrotron emission been used to trace protostellar outflows (e.g. HH 80-81, Carrasco-González *et al.* 2010; Feeney-Johansson *et al.* 2019; Vig *et al.* 2018).

The basic idea behind analysing emission lines towards outflow regions is that, from their presence, absence or intensity ratios physical quantities such as temperature, density, ionisation fraction, etc. can be derived (e.g. Osterbrock and Ferland 2006). Additionally, spectral mapping of protostellar outflows at different transitions provides insightful information about the physics of the occurring shocks (C-type/J-type, dissociative/non-dissociative) and ultimately on the question of how stars are forming.

Surprisingly, protostellar outflows can exhibit multiple coexisting gas components from very low temperatures ($T \sim 100$ K) up to several thousand K and in a few cases even noticeably higher temperatures. Consequently, protostellar outflows are far from being in thermodynamical equilibrium and are most appropriately described in local thermodynamical equilibrium (LTE) conditions as most astrophysical objects. This circumstance can be interpreted as a natural consequence of the presence of shocks and the interaction of the jet with the environment.

Ultimately, all existing outflow components must be taken into account in order to derive rigorous conclusions on the global energy budget of the outflow. In the following paragraph we present a brief summary of the most relevant emission lines probing specific physical conditions in protostellar outflows.

Probing protostellar outflows

Outflows associated with Class 0 sources are predominantly detected in molecular species such as CO, SiO, SO at submillimetre wavelengths or in H₂ in the infrared (see reviews Lee 2020; Richer *et al.* 2000). The low-J pure rotational CO lines at 2.6 mm, 1.3 mm, and 0.86 mm trace cold ($T \sim 50$ –100 K), swept-up gas, whereas higher J-transitions of CO are considered to originate from the actual outflow, that

is a high-velocity, collimated jet at temperatures up to $T \sim 500$ K (Yıldız *et al.* 2015, and references therein). Very dense gas ($n(\text{H}_2) \sim 10^5\text{--}10^6 \text{ cm}^{-3}$) at $T \sim 100\text{--}500$ K is traced by SiO emission (Cabrit *et al.* 2007; Nisini *et al.* 2007). SiO molecules are assumed to be produced in shocked outflow material (C-shocks) via grain sputtering (Caselli *et al.* 1997; Schilke *et al.* 1997). The near-infrared $2.122 \mu\text{m } \nu = 1-0 \text{ S}(1)$ line of H_2 traces warm ($T \sim 2\,000\text{--}3\,000$ K), shocked molecular gas and typically originates from non-dissociative regions such as bowshock wings or boundary regions between the jet and the ambient medium (e.g. Bally *et al.* 2007). Generally, H_2 emission lines have proved to be a powerful tracer of parsec-scale jets towards both Class 0 and Class I outflows (Eisloffel 2000). Complementary observations of various [Fe II] lines in the near-infrared (e.g. $1.644 \mu\text{m}$) are often useful to probe shock-excited regions associated with Class 0/I/II outflows (Davis *et al.* 2003, 2011a; Garcia Lopez *et al.* 2008, 2010; Nisini *et al.* 2002). In contrast to the H_2 emission line at $2.122 \mu\text{m}$ the near-infrared [Fe II] lines trace partially-ionised, hot gas at $T_e \sim 10\,000$ K and (electron) densities up to $n_e \sim 10^5 \text{ cm}^{-3}$ (e.g. Nisini 2008; Pesenti *et al.* 2003). Both near-infrared emission lines may be attributed to different shock types, whereby [Fe II] emission is mainly produced in dissociative J-shocks and H_2 in non-dissociative C-type shocks (O’Connell *et al.* 2005). Near-infrared [Fe II] lines are utilised to derive electron temperatures T_e , electron densities n_e and maybe even more importantly visual extinctions A_V making them a powerful tool in combining optical and infrared spectral line diagnostic (Nisini 2008; Nisini *et al.* 2005). In particular, Class I and Class II outflows are commonly observed in optical transitions such as [O I] $\lambda 6300$, $\text{H}\alpha$, [S II] $\lambda\lambda 6716, 6731$, and [N II] $\lambda 6583$. Most detailed observations are undertaken at high spatial resolution ($\theta \lesssim 0.1''$) with the Hubble Space Telescope (e.g. Bally *et al.* 2002a; Hartigan *et al.* 2011, 2019; Ray *et al.* 1996; Reipurth *et al.* 1997). Principally, these optical lines probe very hot ($T_e \sim 5\,000\text{--}20\,000$ K), ionised gas at electron densities in range of $n_e \sim 10^4\text{--}10^5 \text{ cm}^{-3}$ (e.g. Dougados *et al.* 2010). Solely based on optical line ratios of S^+ , O^0 , and N^+ Bacciotti and Eisloffel (1999) developed a unique technique (BE method) to measure electron densities, temperatures, and even ionisation fractions $x_e = n_e/n_{\text{H}}$ in protostellar jets. More evolved Class II outflows are commonly observed as small-scale microjets (e.g. in [O I] $\lambda 6300$, [N II] $\lambda 6583$, [S II] $\lambda 6731$, [Fe II] $_{1.64}$, H_2 at $2.12 \mu\text{m}$) close to the driving source (e.g. Bacciotti *et al.* 2002; Dougados *et al.* 2002; Lavalley-Fouquet *et al.* 2000; Ray 2007).

The special status of the [O I] $_{63}$ line

The far-infrared [O I] $_{63}$ emission line plays an important role amongst the presented outflow tracers. Compared to optical or near-infrared emission lines the far-infrared [O I] $_{63}$ line is suitable to study the warm ($T \sim 500\text{--}2\,000$ K), dense

($n \sim 10^4\text{--}10^5 \text{ cm}^{-3}$), atomic outflow component. Additionally, it is expected that the $[\text{OI}]_{63}$ emission line plays a crucial role as a main coolant in shock-excited gas associated with outflows (Hollenbach and McKee 1989). As such, this line is the best tracer of the interactions between the high velocity primary jet and the dense ambient medium. Other tracers such as the near-infrared $[\text{Fe II}]$ or H_2 emission lines are affected by extinction, so that detailed studies of extended jets from highly embedded objects are usually performed only far from the central source (i.e. $> 10''$). In these regions, however, the jet has already interacted with the ambient medium through multiple shocks, losing the pristine information about its acceleration mechanism.

Unfortunately, the $[\text{OI}]_{63}$ line is absorbed by the water-vapour in the Earth's atmosphere. Therefore this line is not accessible from the ground. However, observations at the $[\text{OI}]_{63}$ transition are possible via satellites (e.g. Herschel, ISO), balloons (e.g. STO, STO2, BLAST), and as part of this thesis with SOFIA – an airborne observatory (see Chapter 3).

2.4 The atomic outflow component traced by the far-infrared [O I]₆₃ emission line

The atomic oxygen system

After hydrogen and helium, oxygen is the third most abundant element in the universe (e.g. Asplund *et al.* 2009; Pilyugin *et al.* 2003). The energy needed to ionise atomic oxygen is 13.61806 eV² (1st ionisation potential), almost coinciding with the ionisation energy of atomic hydrogen (13.59844 eV³). It is thus fair to say that whenever atomic oxygen is neutral so is hydrogen. The corresponding temperature at which ionisation becomes important may be calculated via equating the ionisation energy with the internal energy per particle of an ideal gas ($E = 3/2 k_B T$). Therefore, above $T \sim 2 \times 10^5$ K significant parts of oxygen atoms within a gas mixture will be ionised (Maxwellian distribution). In a strong shock this temperature is reached for shock velocities $v_s \gtrsim 70 \text{ km s}^{-1}$ (from the corresponding equation in Table 2.2).

Chemically, oxygen is a sixth main group element with the electronic ground state configuration [He] 2s² 2p⁴. Since oxygen is a light element (atomic number: $Z = 8$) the Russell-Saunders-Coupling scheme characterises the spin-orbit interaction of the involved electrons to a good approximation (Russell and Saunders 1925). In this scheme, the total orbital momentum L , the total spin S and the total angular momentum J of a multi-electron system is given by

$$L = \sum_i l_i, \quad S = \sum_i s_i, \quad J = L + S, \quad (2.2)$$

whereby l_i and s_i represent the orbital moments and spins of each individual bound electron. As a result of the spin-orbit coupling, an additional term in the Hamiltonian of the system appears ($\hat{H}_{\text{so}} = \text{const} \times L \cdot S$) leading to a split of the fundamental energy level into several distinct energy levels – the *fine-structure-splitting* (e.g. Draine 2011). The relative energy shifts are on the order of about 10⁻² eV. In the case of atomic oxygen (short: OI), the fundamental energy level is split into three fine-structure levels (triplets) denoted as ³P₂, ³P₁, and ³P₀ in ascending order of energy (Fig. 2.6).⁴

All possible transitions in-between the three lowest ³P_{*j*} levels are *forbidden*, that is they are not electric dipole transitions, since they all violate at least the Laporte

² <https://webbook.nist.gov/cgi/inchi?ID=C17778802&Mask=20>

³ <https://webbook.nist.gov/cgi/cbook.cgi?ID=C12385136&Mask=20>

⁴ Spectroscopic notation for the energy levels (e.g. Draine 2011): $^{2S+1}L_J^p$ with S , J , and p as total spin, total angular momentum, and parity, respectively. The parity is labelled either with the symbol o for a state of odd parity or *blank* for a state of even parity. The letters $L = S, P, D, F, \dots$ correspond to the total orbital angular momentum $L = 0, 1, 2, 3, \dots$

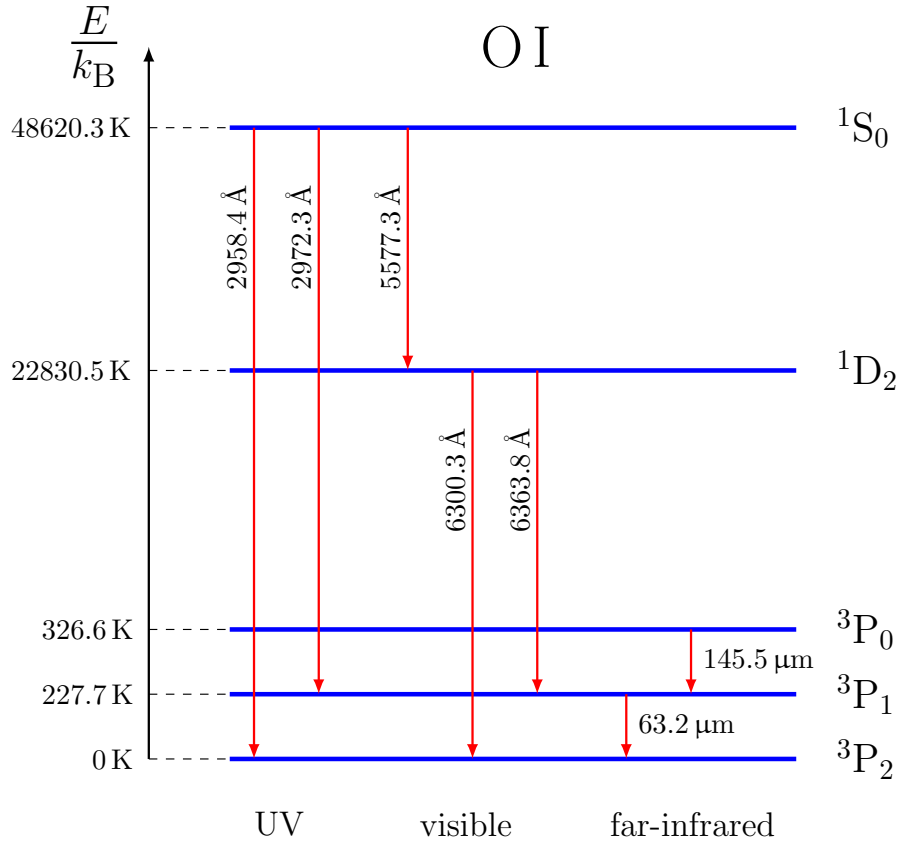


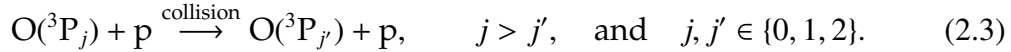
Fig. 2.6. Energy level diagram for the O I system (Grotrian diagram). The lowest five energy levels together with selected ultraviolet, optical, and far-infrared transitions are depicted. Due to L-S-coupling the lowest energy level is split into three fine-structure levels ($^3P_{2,1,0}$) from which the two far-infrared [O I] $_{63,145}$ emission lines emerge. The term symbol 3P_2 denotes the ground state.

selection rule (Tennyson 2019). More specifically, the two forbidden far-infrared [O I] $_{63,145}$ emission lines arise from magnetic dipole transitions. Optical forbidden lines such as the [O I] $\lambda 6300$, [O I] $\lambda 6363$, and [O I] $\lambda 5577$ lines arise from transitions from higher excited states (1D_2 , 1S_0).

The terminology *forbidden* might be chosen rather unfortunate since they are not strictly forbidden – their transition probabilities for spontaneous emission are just too low to be seen under laboratory conditions on Earth. The only strictly forbidden transition in the 5-level oxygen system is the radiative decay from 1S_0 to 1P_0 since it violates the conservation of angular momentum. The appearance of forbidden emission lines in astrophysical spectra can be explained by collisional excitation on microscopic level in a very thin medium (Bowen 1927; Eddington 1927). Thus, the term *collisionally excited* lines may be more fitting. In the framework of emission line diagnostics towards outflows photoexcitation and photoionisation are usually neglected, although this assumption may not be valid very close to the forming protostar.

[O I] line cooling

Typically, oxygen atoms are in the ground state in the interstellar medium. The first excited states ($^3P_{1,0}$) are about ~ 300 K above the ground state. A collision with another free particle p such as hydrogen atoms, hydrogen molecules or free electrons can lead to an excitation of an oxygen atom to a higher energy level as indicated in this reaction



The corresponding transition probabilities⁵ for spontaneous emission are on the order of $A_{ul} \sim 10^{-5} - 10^{-4} \text{ s}^{-1}$ indicating mean lifetimes ($\tau \sim 1/A_{ul}$) of several hours. However, in low-density astronomical environments the excited oxygen atom can have enough time for a spontaneous decay before another collision happens. A collisional de-excitation would not be accompanied with the emission of a photon, since it is qualitatively the reverse reaction of Eq. 2.3. However, a spontaneous decay to a lower state is accompanied with the emission of a photon at $63.1852 \mu\text{m}$ ($^3P_1 \rightarrow ^3P_2$) or $145.5254 \mu\text{m}$ ($^3P_0 \rightarrow ^3P_1$). The direct transition from the 3P_0 to the 3P_2 state is highly unlikely given the transition probability of $\sim 1.34 \times 10^{-10} \text{ s}^{-1}$ corresponding to a mean lifetime of about 300 years. If the emitted photons freely escape the gas after the radiative decay the gas effectively cools down via the so called [O I] line cooling.

The theoretical [O I]₆₃/[O I]₁₄₅ line ratio

Quantitatively, the statistical population of each energy level in the atomic oxygen system can be analysed in detail with a set of simple rate equations including collisional excitation/de-excitation and spontaneous decay (e.g. Goldsmith 2019; Liseau *et al.* 2006; Osterbrock and Ferland 2006). Given the fact that collisional rate coefficients for the atomic oxygen system with various collisional partners are available (e.g. Abrahamsson *et al.* 2007; Jaquet *et al.* 1992; Lique *et al.* 2018; Vieira and Krems 2017) theoretical [O I]₆₃/[O I]₁₄₅ line intensity ratios can be calculated as a function of temperature, density, and gas mixture. Generally, all such line ratio diagrams are only useful, if the observed emission originates from the same region featuring homogeneous excitation conditions. This premise is violated almost always when observing cooling zones behind shocks, since they are potentially unresolved by the observations (Hartigan *et al.* 1994). Recently, Harti-

⁵ Transition probabilities for the most relevant atomic species are listed in <https://www.nist.gov/pml/atomic-spectra-database>

gan *et al.* (2019) successfully resolved such cooling zones in the optical using the HST. However, best available telescopes that can be used to observe the $[\text{O I}]_{63}$ line (e.g. Herschel/PACS, SOFIA/FIFI-LS) have a 50 times lower spatial resolution.

Nisini *et al.* (2015) modelled the atomic oxygen system including the five lowest lying energy levels as depicted in Fig. 2.6. In their model two main collisional partners (atomic and molecular hydrogen) contribute to the collisional excitation and de-excitation of atomic oxygen in an almost neutral, dense environment. It is reasonable to neglect excitation and de-excitation via electron-oxygen collisions – they become relevant only for $n(e^-)/n(\text{H})$ fractions larger than 0.6 (Podio *et al.* 2012). A reproduction of the line intensity ratio diagram starting from the low-density limit ($n_{\text{coll}} \lesssim 10^4 \text{ cm}^{-3}$) to the high-density limit ($n_{\text{coll}} \gtrsim 10^6 \text{ cm}^{-3}$) for three different temperatures is depicted in Fig. 2.7. In the low-density limit collisional de-excitation is unimportant, since almost every collisional excitation is followed by radiative decay. In contrast, in the high density limit most collisional excitations are followed by collisional de-excitation. Radiative decays that would produce photons are effectively suppressed and the associated emission lines are *quenched*.

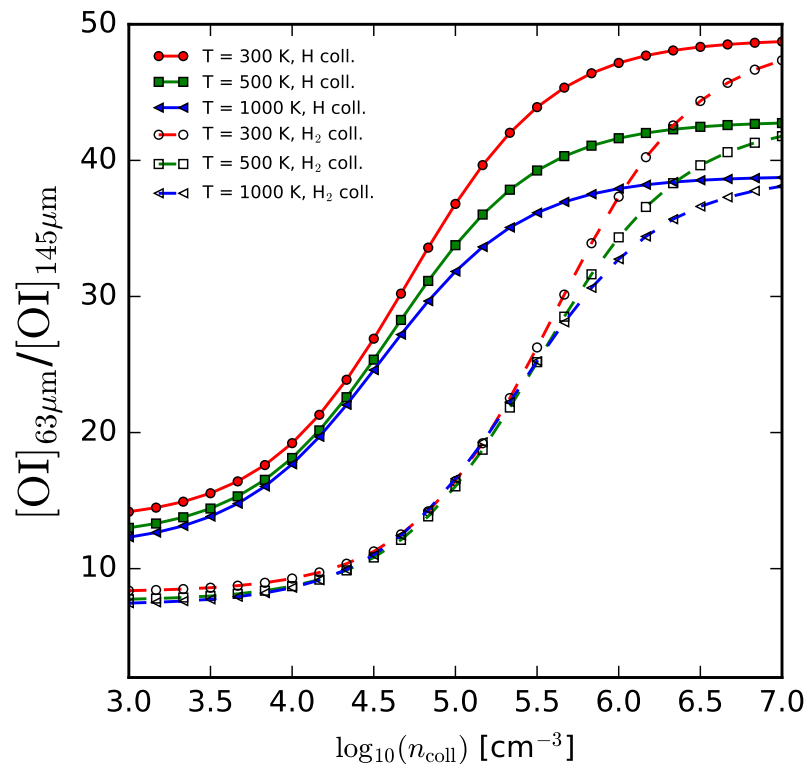


Fig. 2.7. The theoretical $[\text{O I}]_{63}/[\text{O I}]_{145}$ line intensity ratio plotted as a function of the collider density n_{coll} for three temperatures. Solid (dashed) lines correspond to collisions with atomic (molecular) hydrogen. Reproduced from Nisini *et al.* (2015).

From Figure 2.7 we see that the $[\text{O I}]_{63}$ emission line is predicted to be 10–50 times stronger than the $[\text{O I}]_{145}$ line. Inversely, Fig. 2.7 may be utilised to derive hydrogen densities from the $[\text{O I}]_{63}/[\text{O I}]_{145}$ line intensity ratio (Nisini *et al.* 2015).

$[\text{O I}]$ emission towards YSOs

The theoretical prediction of the $[\text{O I}]_{63}/[\text{O I}]_{145}$ ratio is in very good agreement with observations towards protostellar outflows (e.g. Liseau *et al.* 2006; Nisini *et al.* 2015; Podio *et al.* 2012). More recently, Alonso-Martínez *et al.* (2017) analysed far-infrared spectra of 76 YSOs at different evolutionary stages in Taurus. They detected the $[\text{O I}]_{63}$ line towards all known outflow sources. In the case of non-outflow sources the $[\text{O I}]_{63}$ detection rate drops to 31 percent. Additionally, the $[\text{O I}]_{63}$ line is significantly stronger towards outflow sources as compared to non-outflow sources. These statistically reliable findings strongly support the interpretation that a substantial part of the detected far-infrared $[\text{O I}]$ emission towards protostellar outflows traces the warm, dense, atomic outflow component.

Possible origins of the $[\text{O I}]_{63}$ line

In principle, the $[\text{O I}]_{63}$ emission line can originate from various physical environments:

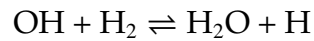
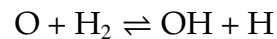
- a) stationary C- and J-type shocks (Flower and Pineau Des Forêts 2010; Flower and Pineau des Forêts 2015; Hollenbach and McKee 1989),
- b) a photodissociation region (PDR), that is due to UV-illumination by a nearby (proto)star or by the interstellar UV-field (e.g. Goldsmith 2019; Hollenbach and Tielens 1997a);
- c) the surface of a gas-disk (e.g. Gorti and Hollenbach 2008; Gorti *et al.* 2011; Kamp *et al.* 2011);
- d) the collapsing envelopes surrounding YSOs (Ceccarelli *et al.* 1996)
- e) debris disk sources (Riviere-Marichalar *et al.* 2012, 2016)

It is challenging to quantitatively disentangle all possible contributions to the total observed $[\text{O I}]_{63}$ line flux (see Section 4.2).

Oxygen chemistry in shocks

Oxygen atoms are involved in a complex chemical network in the interstellar medium (e.g. Hollenbach and McKee 1989). Main oxygen carriers in astrophysical environments are e.g. CO, OH, H₂O, HCO⁺. In shocks, oxygen atoms may

react for $T \gtrsim 300$ K with hydrogen forming OH and H₂O via the reactions (Draine and McKee 1993; Flower and Pineau Des Forêts 2010)



Thus, oxygen atoms can be removed or released in protostellar outflows. Other far-infrared coolants depending on the shock environment can contribute to the total cooling. Stationary shock models such as the ones from Flower and Pineau Des Forêts (2010), Flower and Pineau des Forêts (2015), and Hollenbach and McKee (1989) include chemical networks, so that their impact to the observable spectrum can be evaluated. Thus, supplementary observations at transitions of OH and H₂O might help to understand the chemistry in shocks.

CHAPTER 3

Observations with SOFIA

3.1 SOFIA's telescope, capabilities, and instruments



Fig. 3.1. The front of SOFIA together with the author in Stuttgart 2019.

SOFIA, short for **S**tratospheric **O**bservatory **F**or **I**nfrared **A**stronomy, is a highly modified Boeing 747SP¹ aircraft equipped with a 2.69 m Cassegrain-type telescope (Young *et al.* 2012), see Fig. 3.1. The entire telescope is mounted behind two port-side cavity doors inside the airplane fuselage between the wings and the back (Figs. 3.2 and 3.3).

The optical system essentially consists of a parabolic primary mirror made from a massive block of Zerodur (mass: ~ 850 kg) and a secondary mirror assembly consisting of the focus-centering-mechanism, the tilt-chopping-mechanism and the hyperbolic secondary mirror (diameter: 0.35 m, mass: ~ 2 kg), e.g. Bittner *et al.* (1998) and Krabbe (2000). The chopping mechanism attached to the secondary mirror provides chop frequencies in the range of 1 to 20 Hz with a maximum chop throw on sky of $\pm 4'$ (unvignetted). Just like most infrared telescopes the secondary mirror of SOFIA is deliberately undersized to enable chopping without spilling the beam onto the warm region surrounding the primary mirror (Temi *et al.* 2014).

¹SP stands for **S**pecial **P**erformance

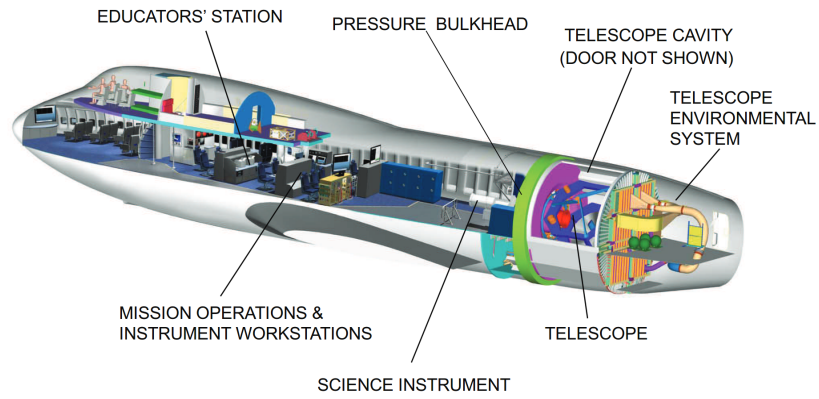


Fig. 3.2. A transparent view of the SOFIA observatory (Credits: Young *et al.* 2012).

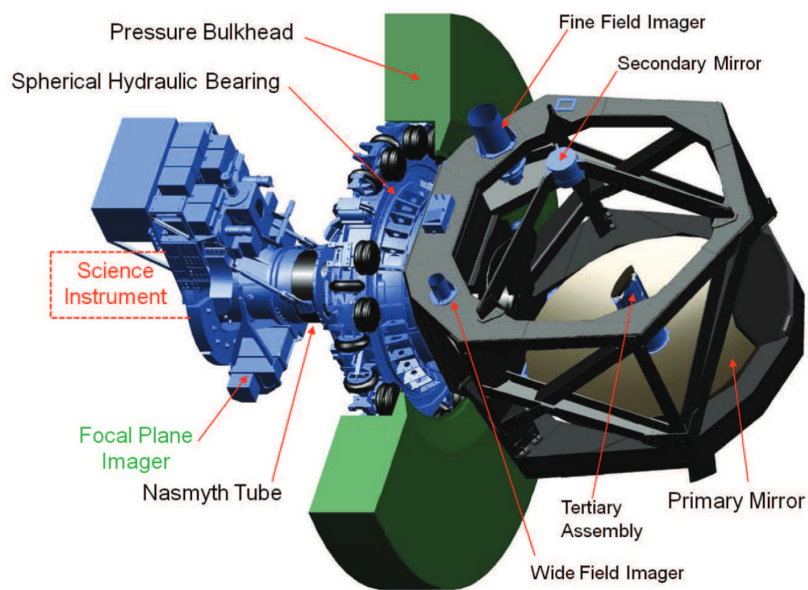


Fig. 3.3. The structural assembly of the SOFIA telescope (Credits: Young *et al.* 2012).

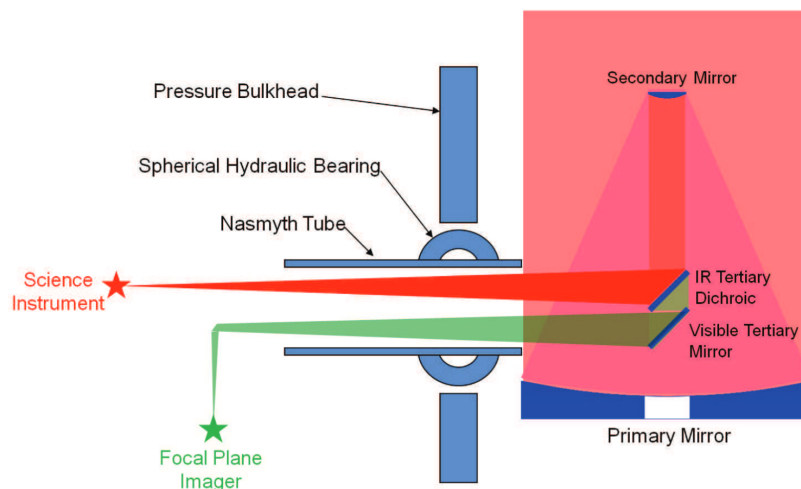


Fig. 3.4. The light guidance within SOFIA's optical system (Credits: Young *et al.* 2012).

As a result SOFIA has an effective aperture diameter of 2.5 m covering an unvignetted field-of-view (FOV) of 8'. Technically, SOFIA's telescope is elaborately stabilised by shock absorbers, a spherical bearing, and spinning gyroscopes providing a nominal pointing stability of about 0.5". The telescope's elevation range is 23°–57°.

A gold-coated dichroic mirror (tertiary mirror) separates the light coming from the secondary mirror into a reflected infrared beam and a visible light beam (Fig. 3.4). Subsequently, both beams are guided spatially separated through the Nasmyth tube. After passage, the infrared beam is fed into the currently installed scientific instrument, whereas the visible part is sent to the Focal Plane Imager (FPI), that is a 1 024 × 1 024 pixel CCD guide camera. Principally, two more visible light cameras are available to collect guiding and tracking information – the Fine Field Imager (FFI) and the Wide Field Imager (WFI).

A variety of science instruments such as FIFI-LS, FORCAST, EXES, GREAT, and HAWC+ are specially designed for imaging, spectroscopic, and polarimetric observations in the infrared and can operate aboard SOFIA (see Fig. 3.5). For a brief description of each individual instrument see e.g. Krabbe *et al.* (2013) and Zinnecker (2013).

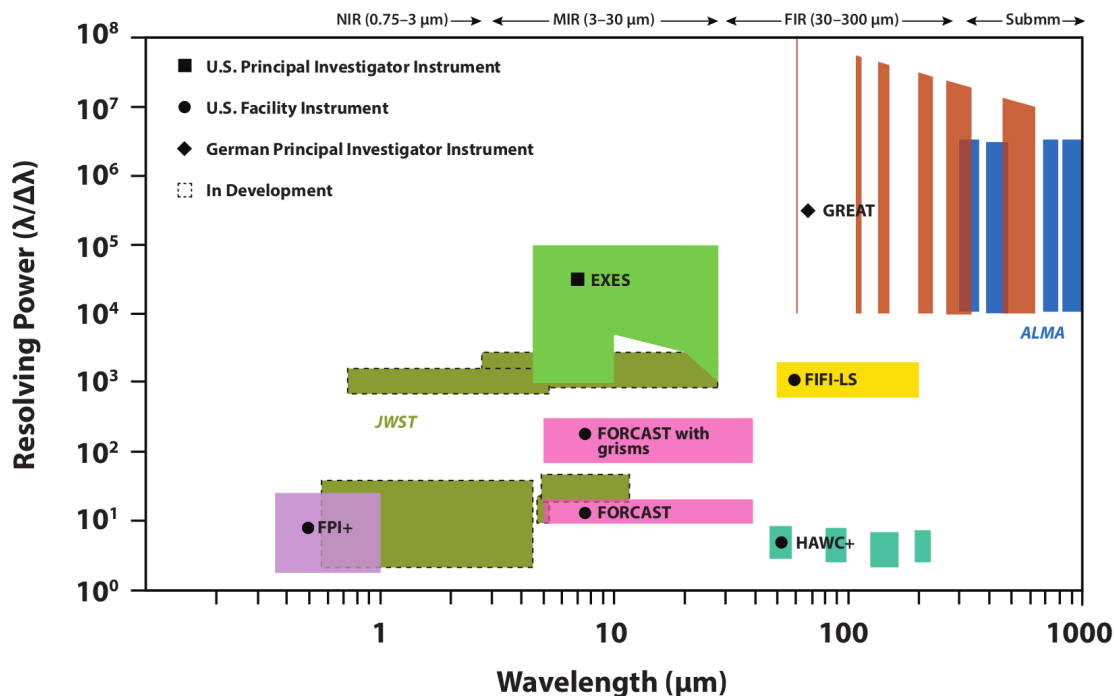


Fig. 3.5. The SOFIA instruments – wavelength coverages and spectral resolving powers. Figure from the SOFIA Quick Guide: https://www.sofia.usra.edu/sites/default/files/Other/Documents/quick_guide.pdf.

All SOFIA instruments together cover a nominal operational wavelength from 0.3 to 1 600 μm , where most radiation is absorbed by the water vapour in the Earth's atmosphere. SOFIA primarily observes in the mid- and far-infrared (30 μm –300 μm). Ground based observations at these wavelengths are typically not feasible forcing astronomers to go above the atmosphere. Therefore, SOFIA operates in the Earth's stratosphere at altitudes of about 12–14 km, that is above 99 % atmospheric water vapour. Through frequent flight missions SOFIA collects valuable astronomical data making it a unique observatory in the world. In fact, compared to ground-based observatories SOFIA's telescope is only of medium size. However, mounting a medium-sized telescope on an aircraft and technically ensuring high-performance observations makes it the largest and most potent telescope observing in the mid- and far-infrared. The main advantages are plain to see: a) SOFIA can operate distinct instruments customised to specific scientific goals; b) SOFIA and its instruments can be steadily improved and repaired, if necessary; c) new instruments can be designed, if needed.

By contract, SOFIA is a joint project of NASA (National Aeronautics and Space Administration) and the DLR (German Aerospace Center). Both partners share the observing time and costs for e.g. maintenance and fuel. The German 20 per cent share is managed by the Deutsches SOFIA Institut (DSI) at the University of Stuttgart. SOFIA's first in-flight night observations were undertaken on May 26 2010.

3.2 The Field Imaging Far-Infrared Line Spectrometer

The Field Imaging Far-Infrared Line Spectrometer (abbreviation: FIFI-LS) is an integral field, far-infrared spectrometer operating aboard SOFIA (Colditz *et al.* 2018; Fischer *et al.* 2018; Looney *et al.* 2000). It consists of two independent grating spectrometers with wavelength ranges of 51 – 120 μm (*blue channel*) and 115 – 200 μm (*red channel*). Thus, the most prominent cooling lines of interstellar gas (e.g. [C II]₁₅₈, [O I]₆₃, [O I]₁₄₅, [O III]₅₂, [O III]₈₈, high-J CO lines, Hollenbach and Tielens 1997b) are in the FIFI-LS range. Both detectors provide an array of 25 \times 16 pixels, that is 5 \times 5 spatial pixels (spaxels) and 16 pixels in the spectral dimension, of Gallium-doped Germanium photoconductors (Fig. 3.6). In the blue channel the projected pixel size is 6'' \times 6'', thus covering a total field of view of 30'' \times 30''. Compared to that, the red channel provides a larger projected pixel size of 12'' \times 12'' with a higher angular coverage of 1' \times 1' field of view.

The spectral resolution $R = \lambda/\Delta\lambda$ depends on the channel being used and observed wavelength varying between 500 and 2 000. At the relevant [O I]₆₃ and [O I]₁₄₅ transitions the spectral resolutions are specified as 1 300 and 1 000, respectively. The corresponding velocity resolution $\Delta v = c/R$ are thus given by

230 km s^{-1} in the blue channel and 300 km s^{-1} in the red channel. The observed FIFI-LS wavelength bands are centered at the rest wavelengths of the [O I] transitions and have a total width of about $0.4 \mu\text{m}$ in the blue channel and $1.0 \mu\text{m}$ in the red channel. In our obtained data, each spectrum in the blue channel (red channel) features a sampling of 34 km s^{-1} (42 km s^{-1}) per spectral element. We used the D105 dichroic beam splitter for our observations. In this instrumental setting the minimum detectable line fluxes (MDLF) for the [O I] $_{63}$ emission line is specified as $\sim 1 \times 10^{-16} \text{ W m}^{-2}$ and for the [O I] $_{145}$ line it is $\sim 2 \times 10^{-17} \text{ W m}^{-2}$ (for a 4σ in 15 min on-source integration).

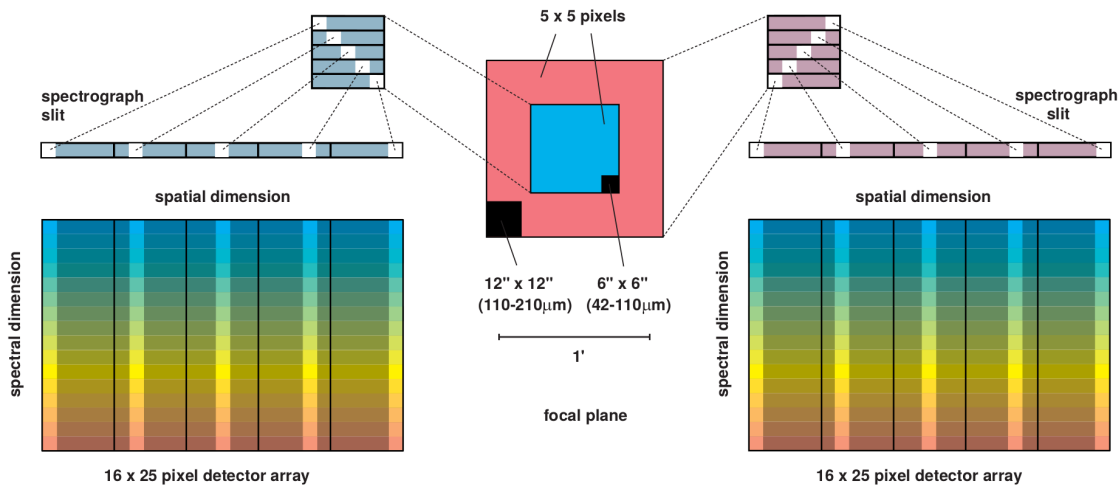


Fig. 3.6. The two channels of FIFI-LS. Figure from (Looney *et al.* 2003).

The diffraction-limited full width of half maximum (FWHM) beam size depends about linearly on the observed wavelength λ . As a rule of thumb, the FWHM in arcseconds is given by λ in μm divided by 10. Ground-based and in-flight FIFI-LS measurements towards point sources show that the beamsizes at $63 \mu\text{m}$ and $145 \mu\text{m}$ are $5.4''$ and $12.4''$, respectively (priv. comm.). The spatial sampling is specified by $1''$ per spaxel in the blue channel and $2''$ per spaxel in the red channel.

Depending on the specific scientific mission different observing strategies (e.g. single pointing vs. raster mapping) and observing modes (symmetric chopping, asymmetric chopping, bright object mode) can be realised with FIFI-LS. Protostellar outflows are extended targets and usually not very bright. Therefore, we chose to map these outflows along their jet axis close to the driving source in a two point symmetric chop mode. This observing strategy proved an advantage since the covered part of the outflow can be dynamically customised in subsequent SOFIA flights, if the [O I] $_{63}$ line detection turned out to be successful. This way, at different SOFIA flights other parts of the outflow can be observed and later put together to one data set.

The result of a SOFIA/FIFI-LS observation is a three dimensional raw data cube ($\text{RA} \times \text{DEC} \times \text{wavelength}$, see Fig. 3.7). Basically, the obtained data cubes can be reduced utilising the data reduction pipeline REDUX (Vacca 2016). This program includes several data reduction steps such as wavelength calibration, spatial calibration, flat fielding, flux calibration, and telluric correction (see Observer’s Handbook²).

The total uncertainty in the absolute flux calibration for the integrated line fluxes amounts to approximately 20 %.

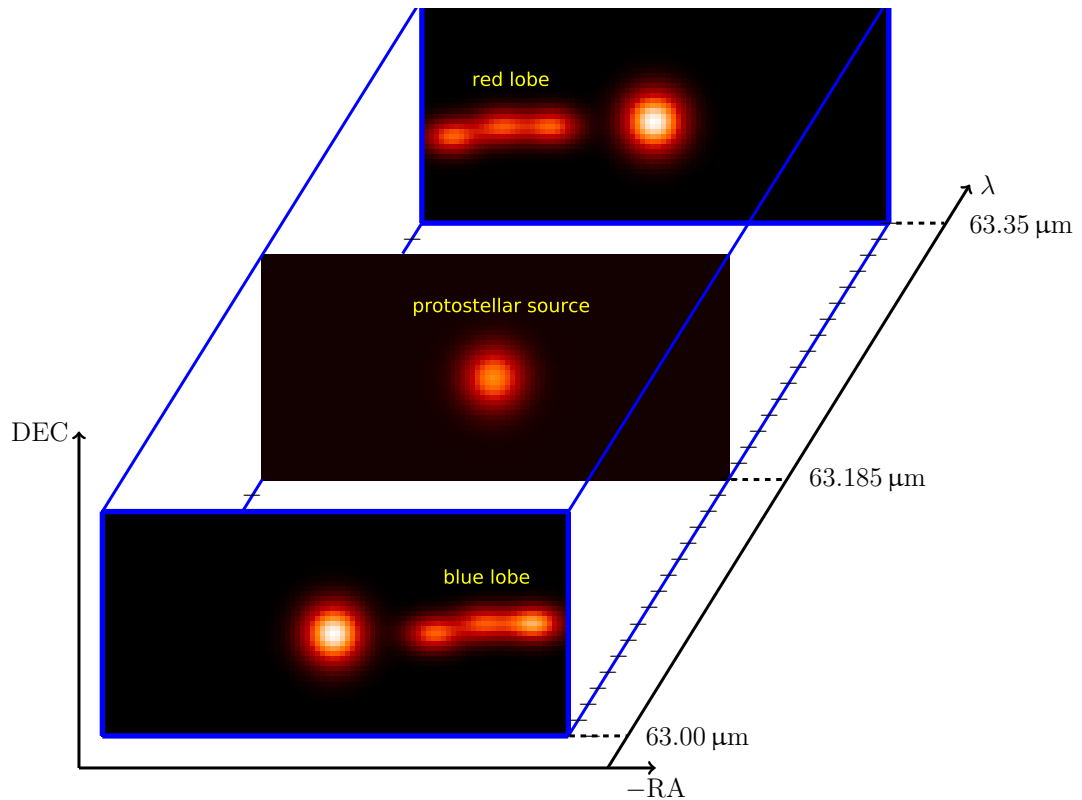


Fig. 3.7. A synthetic SOFIA/FIFI-LS observation towards a protostellar outflow. The final data product is a 3-dimensional data cube ($\text{RA} \times \text{DEC} \times \text{wavelength}$). The bipolar outflow associated with a continuum source – the driving source – should ideally be seen at different stacks of the data cube.

²<https://www.sofia.usra.edu/science/instruments/fifi-ls>

3.3 The sample of nine protostellar outflows

Nine protostellar outflows (Table 3.3) were selected to be mapped for the first time at the two far-infrared transitions of oxygen ($[\text{OI}]_{63,145}$) with the FIFI-LS instrument aboard SOFIA (proposal IDs: 03_073, 05_0200, 07_0069). Observations have been carried out via several SOFIA flights between 2015 and 2019.

Selection criteria

These nine targets are considered to be prototypical, bright protostellar outflows that are mainly driven by low-mass ($M_{\star} \lesssim 1 M_{\odot}$) protostars in their earliest evolutionary stage (Class 0/I). Additionally, all outflows are well studied at various other emission lines, so that in turn a comparative analysis can be carried out. Our targets are not considered to be externally irradiated by e.g. UV radiation from nearby OB stars (Bally and Reipurth 2001; Reipurth *et al.* 1998) and are observable through SOFIA flights in the northern hemisphere.

Tab. 3.1. The sample of nine protostellar outflows observed with SOFIA.

Target	Class	Cloud	RA (J2000) (h m s)	DEC (J2000) ($^{\circ}$ ' ")	D^b (pc)	L_{bol}^a (L_{\odot})
Cep E	0	Cepheus, OB3	23 03 12.8	+61 42 26	730	75
HH 1	0	Orion A, L1641	05 36 22.8	-06 46 06	430	45.7
HH 212	0	Orion B, L1630	05 43 51.4	-01 02 53	420	12.5
HH 26	I	Orion B, L1630	05 46 03.6	-00 14 50	420	$\sim 7^c$
HH 34	I	Orion A, L1641	05 35 29.8	-06 26 58	430	$\sim 15^c$
HH 111	I	Orion B, L1617	05 51 46.1	+02 48 30	420	20.8
L1551 IRS5	I	Taurus, L1551	04 31 34.2	+18 08 05	140	22.9
SVS 13	I	Perseus, L1450	03 29 03.7	+31 16 04	235	32^e
HH 30	I/II	Taurus, L1551	04 31 37.5	+18 12 24	140	$\sim 0.2^d$

^a taken from Karska *et al.* (2018) and van Dishoeck *et al.* (2011), if not stated otherwise; we correct the luminosities for our assumed distances with $L_{\text{bol}} = (D_{\text{adopted}}/D_{\text{paper}})^2 L_{\text{bol}}^{\text{paper}}$;

^b from Zucker *et al.* (2019); ^c Antoniucci *et al.* (2008); ^d Burrows *et al.* (1996); ^e Tobin *et al.* (2016).

CHAPTER 4

Data Reduction

4.1 Mitigating the residual Earth atmosphere

Even though SOFIA operates 12–14 kilometres above the ground the residual Earth atmosphere hinders the observation in the far-infrared. First and foremost the water vapour content in the line of sight between the telescope and the astronomical target determines the atmospheric transmissivity and therefore the contamination in the spectral domain. Thus, the actual flight parameters during observation are of essential importance in properly mitigating the atmosphere (Fig. 4.1).

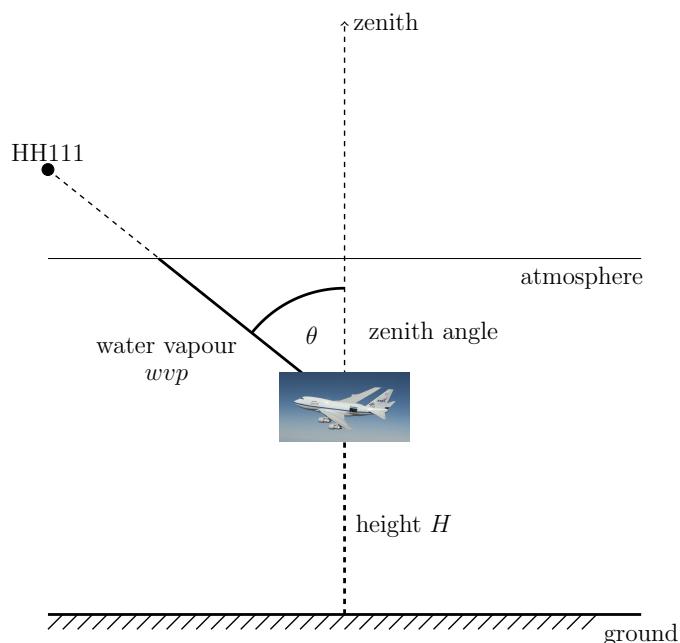


Fig. 4.1. SOFIA flight and relevant atmospheric parameters.

To make matters worse, the $[\text{O I}]_{63}$ emission line lies deep in an absorption feature, where the atmospheric transmission is below 60%. This in turn, causes difficulties in the telluric correction step of the REDUX data reduction pipeline. Bypassing this problematic issue, we wrote our own data reduction software *JENA.py* (abbreviation: Jet Emission Analysis) that mitigates the impact of the Earth's atmosphere as briefly described in the following.

In order to properly model the atmosphere during the observation we utilised synthetic spectra of the atmospheric transmission calculated with the ATRAN software (Lord 1992). Bill Vacca provided all relevant ATRAN models for our data reduction. With this tool in hand a decontamination of the observed spectra is possible and fairly easy to implement.

In detail, a specific ATRAN model, hereafter $\tau(\lambda; \mathbf{a})$, is a dimensionless function ranging between 0 (full absorption) and 1 (no absorption), and depending on wavelength λ and the three flight parameters $\mathbf{a} := \{H, \theta, wvp\}$. The quantities H , θ , and wvp denote the flight altitude, zenith angle, and water vapour overburden.

Fig. 4.2 depicts one randomly selected ATRAN model in the nearest surroundings of the two $[\text{O I}]_{63,145}$ emission lines. At both emission lines the diagram shows numerous complex atmospheric features in the transmission curve impeding the $[\text{O I}]_{63,145}$ line detection. Fortunately, former far-infrared observations of star forming regions indicate that both $[\text{O I}]_{63,145}$ emission lines are not blended by other prominent emission lines (Goicoechea *et al.* 2015; Lerate *et al.* 2006)¹ making them still proficient targets for spectroscopy.

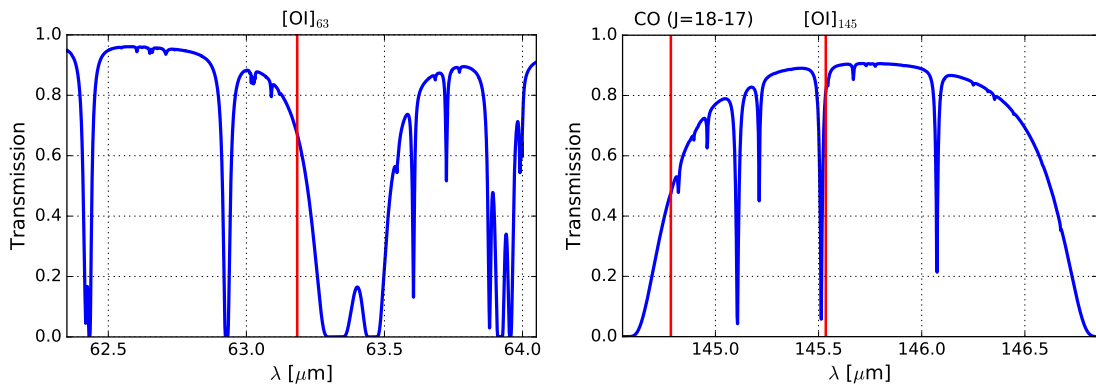


Fig. 4.2. A synthetic transmission curve of the Earth’s atmosphere at the two relevant far-infrared $[\text{O I}]_{63,145}$ emission lines. The depicted ATRAN model has the following parameters: $\mathbf{a} = \{H = 41 \text{ kft}, \theta = 35^\circ, wvp = 7 \mu\text{m}\}$.

We chose one specific ATRAN model for each SOFIA observation according to the actual flight parameters (Table 4.1).

The determination of the water vapour overburden proved to be a challenge in the data reduction step, since accurate in-flight measurements are only available since flight F524 (C. Fischer, private communication). The stated water vapour values for Cep E, HH 1, HH 212, and L1551 IRS5 in Table 4.1 represent actual in-flight measurements from the water vapour monitor (Fischer *et al.* in prep.). However, for the early observed outflows (HH 26, HH 34, HH 111, SVS 13, HH 30) they are reliable estimates undertaken by the SOFIA/FIFI-LS team.

¹The $^{12}\text{CO } J = 18-17$ line at $144.784 \mu\text{m}$ is situated outside of the obtained FIFI-LS coverage. In the case of the $[\text{O I}]_{63}$ line several water lines (e.g. $\text{HDO } 10_{65}-10_{56}$ at $62.231 \mu\text{m}$, $\text{p-H}_2\text{O } 8_{18}-7_{07}$ at $63.322 \mu\text{m}$, $\text{o-H}_2\text{O } 8_{08}-7_{17}$ at $63.457 \mu\text{m}$) are typically at least one order of magnitude weaker.

Tab. 4.1. SOFIA flight information and chosen ATRAN parameters for the nine observed targets.

Target	Obs. date	Flight(s)	Time (min)	θ (°)	H (kft)	wvp (μm)
Cep E	2019-10-30	631	52	50	44	4.00
HH 1	2018-11-09	527	84	45	43	4.00
HH 212	2018-11-08	526	49	40	43	4.25
HH 26	2015-03-12	199	39	50	41	6.00
HH 34	2015-10-22	249	71	55	42	7.00
HH 111	2017-03-07	383	73	40	40	8.00
L1551 IRS5	2019-11-07	637	21	45	43	4.50
SVS 13	2017-03-07	383	61	55	39	6.00
HH 30	2017-02-25	378	35	55	42	6.00

The selected ATRAN model represents an averaged version of the *true* atmospheric conditions during exposure, typically lasting about 1–2 hours per flight leg. SOFIA maintains altitude very accurately during exposure due to official flight level regularities. Experience has shown that it is reasonable to assume that the water vapour overburden (wvp) stays constant in that time. In fact, wvp measurements with the water vapour monitor before and after exposure support this notion (priv. communication). Thus, the only parameter steadily changing during observations is the zenith angle. However, even a change of a few degrees in zenith angle has no substantial influence on $\tau(\lambda; \mathbf{a})$ justifying the proposed method.

Given the medium spectral resolution of FIFI-LS, we assume a simple 1D Gaussian function for the [O I] line profiles, that is

$$\varphi(\lambda; \mathbf{b}) = \frac{A}{\sqrt{2\pi}\sigma} \exp\left[-\frac{1}{2}\left(\frac{\lambda - \mu}{\sigma}\right)^2\right] + B \quad (4.1)$$

with the four independent emission line parameters $\mathbf{b} := \{A, \sigma, \mu, B\}$. Thus, a continuum without additional [O I] line emission implies $A = 0$ and $B > 0$.

Conceptually, the emitted radiation from an astronomical target firstly has to go through the atmosphere, then through the optics of the SOFIA telescope and lastly through the FIFI-LS instrument. The first step in this sequential process is mathematically equivalent to a simple multiplication of $\tau(\lambda; \mathbf{a})$ and $\varphi(\lambda; \mathbf{b})$. The influence of the SOFIA/FIFI-LS instrument (second step) is modelled as a convolution (symbol: $*$) in the spectral domain with the instrumental function, hereafter $\text{SIF}(\lambda; R)$. The function $\text{SIF}(\lambda; R)$ depends on the wavelength λ and the spectral resolution R . Typically, $\text{SIF}(\lambda; R)$ is modeled by a 1D Gaussian filter function basically smoothing the received signal. Consequently, we expect to detect the discrete signal $y = \{y_k\}_{k=1, \dots, N}$ sampled at N spectral grid points λ_k , i.e.

$$y(\lambda_k; \mathbf{a}, \mathbf{b}, R) = S([\varphi(\lambda; \mathbf{b}) \cdot \tau(\lambda; \mathbf{a})] * \text{SIF}(\lambda; R)). \quad (4.2)$$

Here, we introduced the function S that samples the modelled signal to equidistant wavelength grid points λ_k predetermined by the individual FIFI-LS data cubes.

Figures 4.3 and 4.4 visualize the described mathematical fit procedure on the basis of synthetic FIFI-LS spectra at both relevant [O I] emission lines. The first column in Figs. 4.3 and 4.4 shows row by row $\varphi(\lambda; \mathbf{b})$ for three relevant astronomical cases: 1. a pure continuum contribution; 2. a continuum plus a red-shifted emission line ($v_r = +100 \text{ km s}^{-1}$); 3. a continuum plus a blue-shifted emission line ($v_r = -100 \text{ km s}^{-1}$). The second column plots the imprint of the atmosphere on the spectra, that is $\varphi(\lambda; \mathbf{b}) \cdot \tau(\lambda; \mathbf{a})$. Finally, the third column shows the convolution with the SOFIA/FIFI-LS instrumental function representing the expected signal in one FIFI-LS spaxel.

In order to extract the relevant emission line information \mathbf{b} from the obtained spectra, we applied a non-linear least-squares fit (Levenberg Marquard algorithm, Newville *et al.* 2016) in each spaxel of the preprocessed FIFI-LS datacubes. We were able to improve the quality of the fit by weighting the χ^2 in the minimizing procedure with the atmospheric transmission, that is defining

$$\chi^2 = \sum_{k=1}^N \tau(\lambda_k; \mathbf{a}) \cdot \left(\frac{\text{data}(\lambda_k) - y(\lambda_k; \mathbf{a}, \mathbf{b}, R)}{\epsilon(\lambda_k)} \right)^2 \quad (4.3)$$

with $\epsilon(\lambda_k)$ as individual flux errors. This way, we take into account the fact that parts of the spectra appeared noisier where the atmospheric transmission is comparably low.

The continuum subtracted flux f (units: $[f] = \text{erg s}^{-1} \text{ cm}^{-2}$) in one specific spaxel is solely determined by the parameter A , since

$$f := \int_{-\infty}^{\infty} (\varphi(\lambda, \mathbf{b}) - B) d\lambda = A. \quad (4.4)$$

The parameter B (units: $[B] = \text{erg s}^{-1} \text{ cm}^{-2} \mu\text{m}^{-1}$) represents the continuum flux in the given spaxel. Errors in the parameters \mathbf{b} are estimated from the covariance matrix.

In conclusion, the data reduction program JENA.py generates a continuum subtracted [O I] map together with continuum map for a given preprocessed SOFIA/FIFI-LS data cube. The optimal extraction subroutine implemented in JENA.py is not discussed here in detail (see description in Sperling *et al.* 2020).

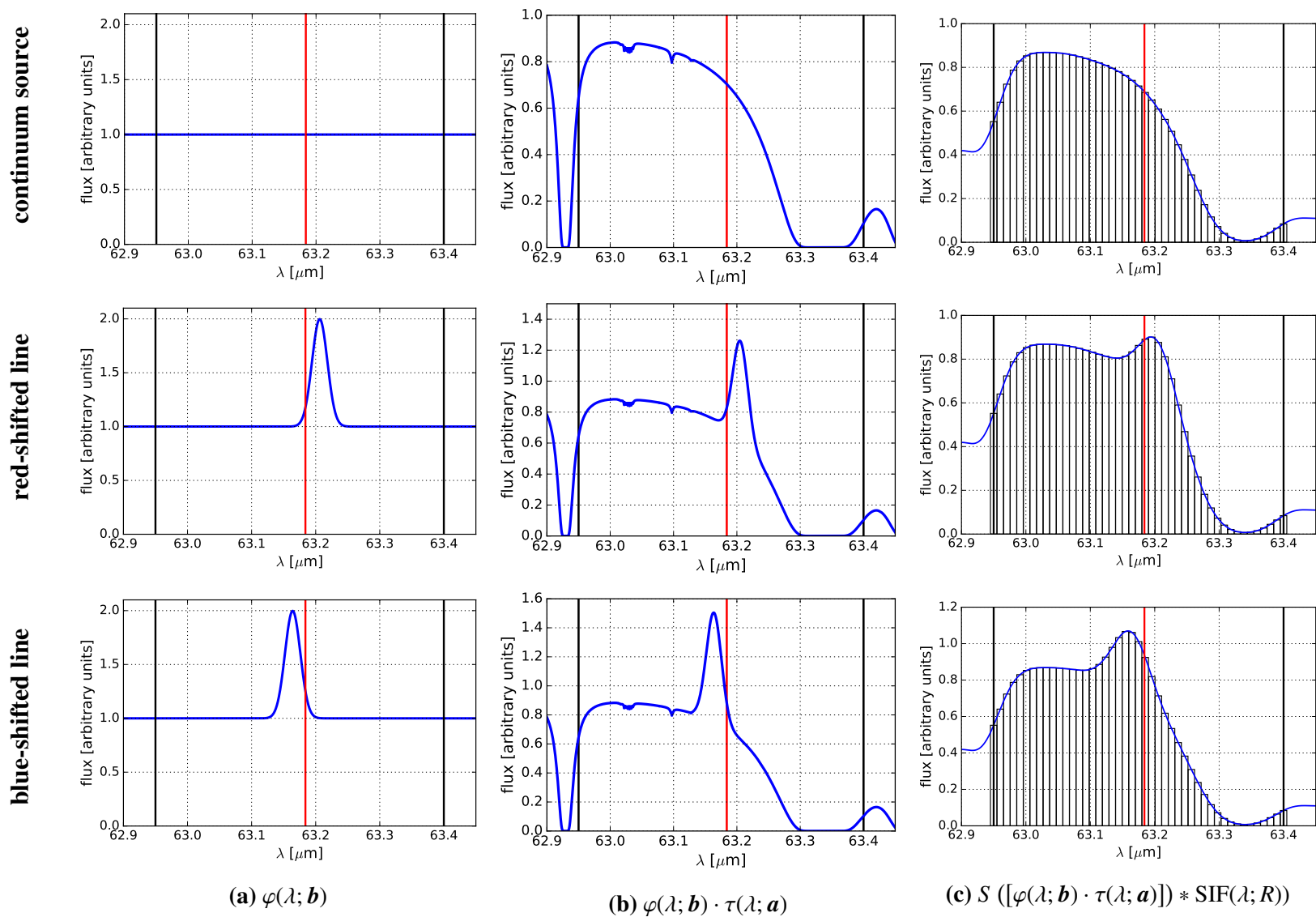
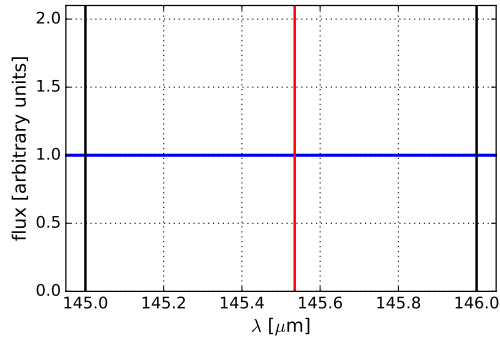
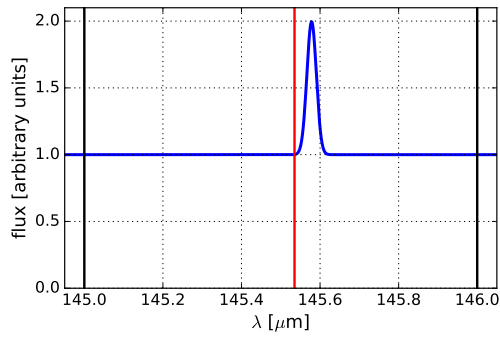


Fig. 4.3. Synthetic spectra and expected signals from protostellar outflows in the $[\text{O I}]_{63}$ emission line.

continuum source



red-shifted line



blue-shifted line

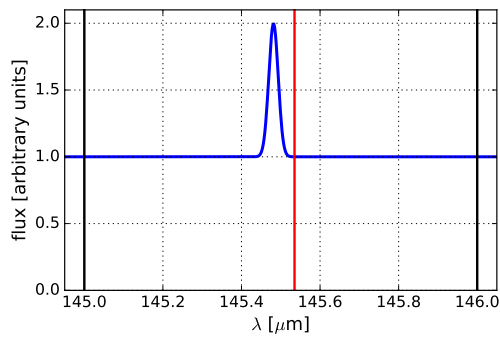
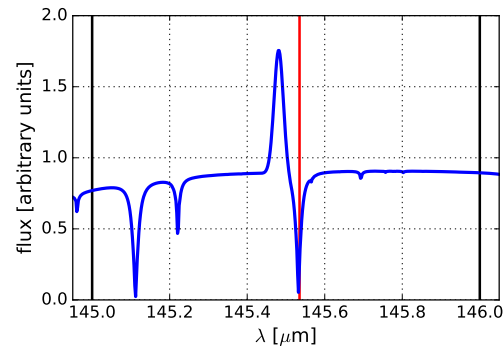
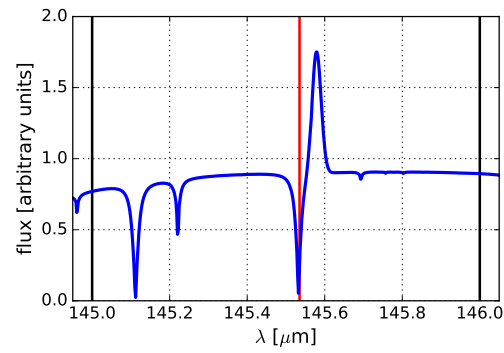
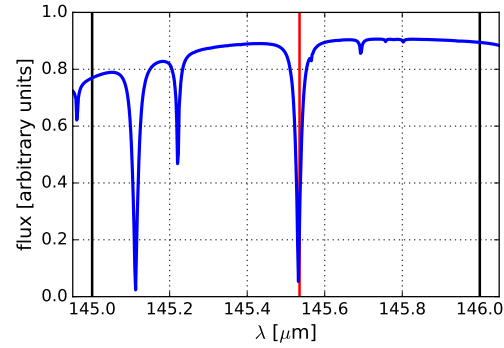
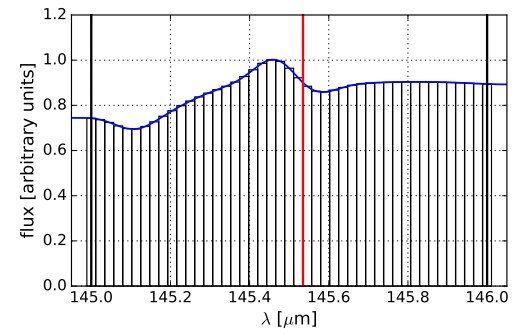
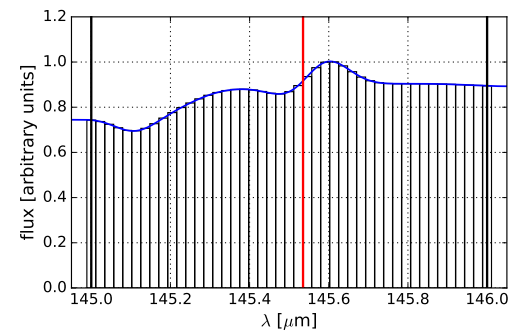
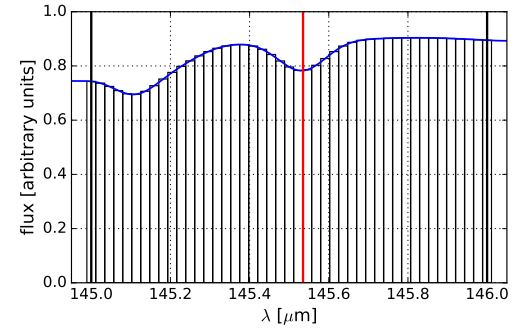
(a) $\varphi(\lambda; \mathbf{b})$ (b) $\varphi(\lambda; \mathbf{b}) \cdot \tau(\lambda; \mathbf{a})$ (c) $S([\varphi(\lambda; \mathbf{b}) \cdot \tau(\lambda; \mathbf{a})]) * \text{SIF}(\lambda; R)$

Fig. 4.4. Synthetic spectra and expected signals from protostellar outflows in the [O I]₁₄₅ emission line.

4.2 Mass-loss rate measurements

Mass-loss rates associated with protostellar outflows can be estimated via various observational strategies (see e.g. Dougados *et al.* 2010). Mainly they are:

- a) CO rotational lines are used to estimate the time-averaged mass-loss rate that is potentially associated with swept-up molecular gas (Bontemps *et al.* 1996; Hatchell *et al.* 2007; Hogerheijde *et al.* 1998; Tanabe *et al.* 2019; van Kempen *et al.* 2009; Yıldız *et al.* 2015).
- b) If the main outflow material is collimated in a spatially resolved jet, then the mass-loss may be estimated geometrically from the mean jet density n_{jet} , velocity v_{jet} , and the radius r_{jet} via $\dot{M}_{\text{jet}} \approx \pi r_{\text{jet}}^2 \times n_{\text{jet}} \times v_{\text{jet}}$ (e.g. Bacciotti and Eisloffel 1999; Bacciotti *et al.* 1999; Coffey *et al.* 2008; Nisini *et al.* 2005; Podio *et al.* 2006).
- c) Mass-loss rates can be determined solely from the jet luminosity in a bright emission line, that is without inferring assumptions on the jet radius. Hartigan *et al.* (1995) utilised the jet luminosity in optical lines ([S II] λ 6731 and [O I] λ 6300) to estimate mass-loss rates. This method can be extended using near-infrared emission lines of [Fe II] or H₂ (e.g. Antonucci *et al.* 2008; Caratti o Garatti *et al.* 2012; Nisini *et al.* 2005).
- d) Apart from the three standard methods mentioned in a)–c), Hollenbach (1985) and Hollenbach and McKee (1989) proposed a shock model, in which mass-loss rates towards protostellar outflows are solely determined from the far-infrared [O I]₆₃ line luminosity.

As discussed in detail by Cabrit (2002) all proposed methods have their specific limitations. Common to all of them is that only the observable part of the outflow is taken into account when calculating mass-loss rates. If some material flows without interaction with the ambient medium, is not excited, or is simply too diffuse to emit, mass-loss rates are being underestimated. Additionally, some detected emission can be caused by entrained or deflected material which complicates the situation.

The two suitable methods

Based on our SOFIA observations two approaches are worth considering here: 1) \dot{M}_{out} from the jet luminosity (c); 2) \dot{M}_{out} from a shock model (d). As described in detail in the corresponding Sections 4.2.1 and 4.2.2, both methods are based on the underlying premise that any PDR (Goldsmith 2019) or disk (Gorti and Hollenbach 2008; Gorti *et al.* 2011; Kamp *et al.* 2011) contribution to the observed [O I]₆₃

luminosity is negligible. If in turn a substantial amount of emission originates from PDRs or disk surfaces mass-loss rates derived from both methods only represent upper limits.

A potential contamination by PDRs can be evaluated with the $[\text{O I}]_{63}/[\text{C II}]_{158}$ line ratio, since $[\text{C II}]_{158}$ is thought to arise therefrom (Liseau *et al.* 1997). Values on the order of $[\text{O I}]_{63}/[\text{C II}]_{158} \lesssim 10$ indicate a substantial impact of PDRs, whereas in shock regions this line ratio typically exceeds the value of ~ 10 (Howard *et al.* 2013).

A possible disk contribution is quantified by a few observational studies (Alonso-Martínez *et al.* 2017; Podio *et al.* 2012; Watson *et al.* 2016). In detail, Podio *et al.* (2012) and Watson *et al.* (2016) estimate a disk contribution between 3–15 % for Class 0/I/II outflows. Higher disk contributions up to ~ 20 % and more are stated by Alonso-Martínez *et al.* (2017) for Class I outflows.

4.2.1 Mass-loss rates from a shock model

Hollenbach (1985) and Hollenbach and McKee (1989) put forward a sophisticated shock model, hereafter HM89, that may be utilised to derive mass-loss rates in an intriguingly comfortable way from an observers perspective. One of the main results of their shock model was that the $[\text{O I}]_{63}$ line luminosity, hereafter $L([\text{O I}]_{63})$, and the mass-loss rate ($\dot{M}_{\text{jet}}^{\text{shock}}$) are proportional to each other, that is

$$\dot{M}_{\text{jet}}^{\text{shock}} = 10^{-4} (L([\text{O I}]_{63})/L_{\odot}) M_{\odot} \text{ yr}^{-1}. \quad (4.5)$$

Essentially, the underlying shock scenario assumes the formation of a single decelerated wind shock, where the isotropically ejected material from the driving source impacts the ambient medium. If the material is fast enough to produce a dissociative J-shock the $[\text{O I}]_{63}$ emission line is predicted to be the dominant coolant in the postshock gas over a wide range of shock parameters (shock velocities: $v_s = 30\text{--}150 \text{ km s}^{-1}$, preshock densities: $n_0 = 10^3\text{--}10^6 \text{ cm}^{-3}$). Eq. 4.5 also applies, if the wind is collimated into a jet.

The $[\text{O I}]_{63}$ emission line in the HM89 model is excited collisionally and the emission is explicitly attributed to come from a wind shock. The shock is at the centre of the modelling and therefore many assumptions on shock physics (e.g. Rankine–Hugoniot relations), chemical networks, and the presence of other species (ionic, atomic, molecular) potentially contributing to the emission are inferred. In this framework, Eq. 4.5 is a numerical result (quasi-proportionality) alongside the prediction that among all considered atomic fine structure lines (e.g. $[\text{Si I}]_{25}$, $[\text{Si II}]_{35}$, $[\text{Fe II}]_{26}$, $[\text{C II}]_{158}$) the $[\text{O I}]_{63}$ line dominates the cooling in the decelerated wind shock.

Plausibility of the proportionality in Eq. 4.5

In the framework of the HM89 shock model Eq. 4.5 can be understood qualitatively by the following line of reasoning (Dougados *et al.* 2010; Hollenbach and McKee 1989): In the restframe of the locally plane-parallel shock front gas particles that have entered the shock cool via line emission in various species (Fig. 4.5). The $[\text{O I}]_{63}$ emission line dominates the total line cooling L_{cool} over large parts of the cooling zone with almost the same contributing fraction $1/\alpha$ ($\alpha > 1$). Thus, we can state

$$L_{\text{cool}} = \sum_{\text{all lines}} L(\text{line}) = L([\text{O I}]_{63}) + L([\text{Fe II}]_{26}) + L([\text{S I}]_{25}) + \dots \approx \alpha L([\text{O I}]_{63}). \quad (4.6)$$

Through the line cooling the gas loses internal energy ΔE over the cooling time t_{cool} , that is

$$L_{\text{cool}} = \frac{\Delta E}{t_{\text{cool}}} = \frac{3}{2} k_{\text{B}} (T_2 - T_1) \frac{N}{t_{\text{cool}}}. \quad (4.7)$$

In turn, the total number of particles N that have entered the shock and actually participated in the line cooling are connected to the mass-flow-rate

$$\dot{M}_{\text{flow}} = N \mu m_{\text{H}} / t_{\text{cool}}. \quad (4.8)$$

Finally, combining Eq. 4.6–4.8 leads to the relation

$$\dot{M}_{\text{flow}} = \frac{2 \alpha \mu m_{\text{H}}}{3 k_{\text{B}} (T_2 - T_1)} L([\text{O I}]_{63}), \quad (4.9)$$

that actually predicts the proportionality of between \dot{M}_{flow} and $L([\text{O I}]_{63})$.

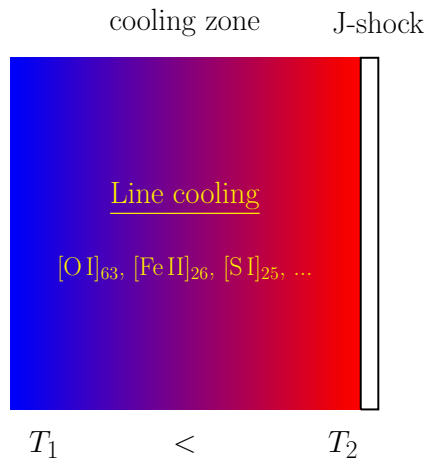


Fig. 4.5. The cooling zone behind a shock. This zone is expected to be only a few AU in size (e.g. Hartigan *et al.* 1994) and is therefore typically unresolved by observations.

We can estimate also the temperature T_2 directly behind the shock front from elementary school physics (Krumholz 2015). The outflow velocity v_{out} has to be on the order of the escape velocity

$$v_{\text{out}} \sim v_{\text{esc}} = \sqrt{\frac{2GM_{\star}}{R_{\star}}} \approx 620 \text{ km s}^{-1} \sqrt{\frac{M_{\star}}{M_{\odot}}} \sqrt{\frac{R_{\odot}}{R_{\star}}}. \quad (4.10)$$

When the outflow first hits the ambient medium, the kinetic energy of the entering particles is converted into internal energy of the gas, that is

$$\frac{v_{\text{out}}^2}{2} \mu m_{\text{H}} \approx \frac{3}{2} k_{\text{B}} T_2 \quad \longrightarrow \quad T_2 \approx \frac{\mu m_{\text{H}} v_{\text{out}}^2}{3 k_{\text{B}}}. \quad (4.11)$$

Note the similarity between Eq. 4.11 and the equation for the temperature of the postshock gas in the strong shock limit (see Tab. 2.2). With the fiducial values $M_{\star} = 0.5 M_{\odot}$ and $R_{\star} = 5 R_{\odot}$ we estimate $v_{\text{out}} \sim 200 \text{ km s}^{-1}$ and finally $T_2 \sim 10^6 \text{ K}$ (Eq. 4.10, Eq. 4.11).

Based on these arguments, an extension of the HM89 method utilising other emission lines may appear intriguing. Indeed, Watson *et al.* 2016 found the transitions of $[\text{Si II}]_{35}$ and $[\text{Fe II}]_{26}$ to be very promising proxies for the $[\text{O I}]_{63}$ emission line. However, not all emission lines may be exploited in the same way, since they might feature different contributing fractions at different parts of the cooling zone.

Over the last 30 years the HM89 relation has been applied extensively determining mass-loss rates in protostellar outflows (e.g. Ceccarelli *et al.* 1997; Cohen *et al.* 1988; Mottram *et al.* 2017; Nisini *et al.* 2015; Podio *et al.* 2012), even though a justification of the applicability can be quite delicate (Sperling *et al.* 2020). In this regard, Giannini *et al.* (2001) even argued that a posteriori confirmation of a dissociative J-shock as origin of the $[\text{O I}]_{63}$ line emission may be possible, if this line dominates the far-infrared line cooling.

The assumption of the shock origin of the $[\text{O I}]_{63}$ emission line detected towards protostellar outflows can be supported by several properties such as morphology or spatial correlations with other shock tracers (e.g. Benedettini *et al.* 2012; Karska *et al.* 2013; Podio *et al.* 2012; van Kempen *et al.* 2010). As an example, a spatial correlation of $[\text{O I}]$ and $[\text{Fe II}]$ emission indicates the presence of dissociative shocks. Furthermore, specific line ratios such as $[\text{O I}]_{63}/[\text{O I}]_{145}$, $[\text{O I}]_{63}/[\text{C II}]_{158}$, and $[\text{Si II}]_{26}/[\text{Fe II}]_{26}$ can be helpful to test the predictions of the HM89 shock model or to disentangle various other origins of the $[\text{O I}]_{63}$ emission (e.g. Alonso-Martínez *et al.* 2017; Giannini *et al.* 2001; Nisini *et al.* 1996, 2015; Watson *et al.* 2016). Line ratios of $[\text{O I}]_{63}/[\text{O I}]_{145} \sim 20 - 40$ are predicted in the HM89 J-shock model and are typically observed towards protostellar sources (e.g. Howard *et al.* 2013; Karska *et al.* 2013; Nisini *et al.* 2015).

However, similar $[\text{OI}]_{63}/[\text{OI}]_{145}$ line ratios are also reproduced by both C- and J-type shock models (Flower and Pineau des Forêts 2015) and PDR models (Kaufman *et al.* 1999). Howard *et al.* (2013) concluded that the $[\text{OI}]_{63}/[\text{OI}]_{145}$ line ratio does not help to discriminate between a jet or a disk origin.

Conclusively, the J-shock assumption in the HM89 shock model may not be undoubtedly verified from sole observations of both far-infrared O I lines or complementary observations in other shock tracers. If in turn the HM89 shock conditions do not prevail, mass-loss rates calculated via Eq. 4.5 may be meaningless.

In principle, the HM89 formula can be generalised for the case of multiple shocks present in the observed outflow region (Dougados *et al.* 2010). Indeed, high resolution HST observations in the optical demonstrate that multiple shocks (internal shocks, bow shocks, deflection shocks, etc.) are rather characteristic for protostellar outflows (e.g. Hartigan *et al.* 2011, 2019). However, comparable high-resolution maps ($\theta_{\text{res}} \lesssim 0.1''$) that clearly resolve individual shocks in the far-infrared [OI] transitions will not be available in the foreseeable future. Thus, in the likely case that the outflow material passes through several, spatially unresolved shocks, the HM89 formula overestimates the mass-loss rate. Nisini *et al.* (2015) concludes that a correction factor for this scenario is on the order of unity, since weaker internal shocks travelling along the outflow compensate for the presence of several shocks in the beam.

4.2.2 Mass-loss rates from the jet luminosity in $[\text{OI}]_{63}$

In this section we briefly derive an equation, first presented in Sperling *et al.* (2020), that connects the $[\text{OI}]_{63}$ line luminosity with the mass-loss rate associated with the outflow.

We start with counting all oxygen atoms N_2 in the $^3\text{P}_1$ state (see Fig. 2.6) that effectively contribute to the observed $[\text{OI}]_{63}$ line luminosity by emitting photons of energy $h\nu_{63} = 3.1438 \times 10^{-14}$ erg, that is

$$L([\text{OI}]_{63})/L_{\odot} = (h\nu_{63} A_{21}/L_{\odot}) \cdot N_2. \quad (4.12)$$

We can express N_2 in terms of useful astronomical quantities as follows

$$N_2 = \left(\frac{N_2}{N(\text{O})} \right) \left(\frac{N(\text{O})}{N(\text{H})} \right) \left(\frac{N(\text{H})}{N_{\text{tot}}} \right) \left(\frac{M_{\odot}}{\mu m_{\text{H}}} \right) \left(\frac{M_{\text{tot}}}{M_{\odot}} \right), \quad (4.13)$$

whereby $N(\text{O})$ represents the total number of oxygen atoms, $N(\text{H})$ is the total number of hydrogen atoms, N_{tot} stands for the total number of atoms, μ is the molecular weight ($\mu \approx 1.24$ for neutral atomic gas), m_{H} is the mass of a hydrogen atom and M_{tot} is the total mass. Reasonably, we assume solar element abun-

dances, i. e. $N(\text{O})/N(\text{H}) = 4.90 \times 10^{-4}$ (Asplund *et al.* 2009). In addition, we adopt $N(\text{H})/N_{\text{tot}} = 0.921$ from Hartigan *et al.* (1995). The term $N_2/N(\text{O})$ in Eq. 4.13 translates to a ratio of number densities $n_2/n(\text{O})$, since we assume the same relevant volume. Combining Eq. 4.12 and Eq. 4.13 we get

$$\left(\frac{M_{\text{tot}}}{M_{\odot}}\right) = 3.16 \times 10^{-3} \left(\frac{n_2}{n(\text{O})}\right)^{-1} \left(\frac{L([\text{OI}]_{63})}{L_{\odot}}\right). \quad (4.14)$$

A relation of M_{tot} to the mass loss rate \dot{M}_{out} is determined by the physical situation, namely the outflow geometry. The mass loss rate can be estimated in a simplistic hydrodynamical model depicted in Fig. 4.6. Denoting \mathbf{j}_{flow} as mass flux

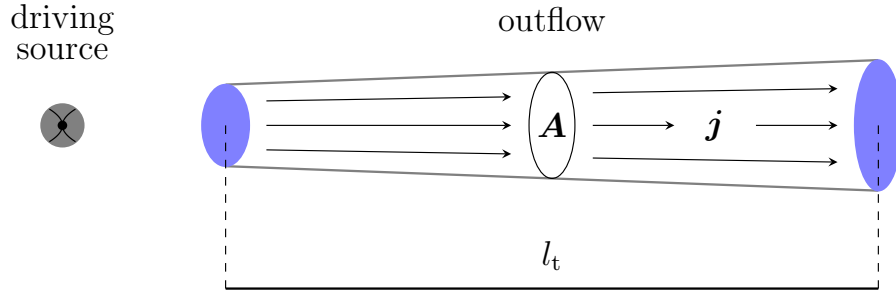


Fig. 4.6. A simple hydrodynamical outflow model, where the outflow material flows within a cylindrical volume with a cross section A . Highly collimated, astrophysical jets typically feature jet velocities on the order of the escape velocity (Livio 2004), that is in the case of jets from low-mass protostars $v_{\text{jet}} \sim 100\text{--}350 \text{ km s}^{-1}$.

(units: $\text{g cm}^{-2} \text{ s}^{-1}$), the local mass flow rate is given by

$$\dot{M}_{\text{out}} = \iint_A \mathbf{j}_{\text{flow}} dA. \quad (4.15)$$

Assuming a steady-flow ($\mathbf{j}_{\text{flow}} = \text{const}$) of the outflow material leads to the familiar relation (Hartigan *et al.* 1995)

$$\dot{M}_{\text{out}} = M_{\text{tot}} v_t / l_t. \quad (4.16)$$

Here, v_t is the component of the velocity on the plane of sky and $l_t \approx \theta \cdot D$ stands for the projected size of the outflow with θ as angular distance and D as physical distance. We combine Eq. 4.14 and Eq. 4.16 to obtain the following equation

$$\left(\frac{\dot{M}_{\text{out}}}{M_{\odot} \text{ yr}^{-1}}\right) = 6.66 \times 10^{-4} \left(\frac{v_t}{\text{km s}^{-1}}\right) \left(\frac{''}{\theta}\right) \left(\frac{\text{pc}}{D}\right) \left(\frac{L([\text{OI}]_{63})}{L_{\odot}}\right) \cdot \left(\frac{n_2}{n(\text{O})}\right)^{-1}. \quad (4.17)$$

With the exception of the ratio $n_2/n(\text{O})$ all other quantities in the above Eq. 4.17 are accessible via observations. Physically, $n_2/n(\text{O})$ represents a level population of the O I system and therefore strongly depends on the environmental conditions

such as gas temperature and density. It seems self-evident to get further insights on the decisive ratio $n_2/n(\text{O})$ utilising the atomic physics presented in Sec. 2.4. Non-LTE calculations performed by Nisini *et al.* (2015) demonstrate that a three level approximation is sufficient to describe the atomic oxygen system for temperatures below $T \sim 5\,000$ K. An analytic solution for such a three level system exists and we utilise it to constrain the ratio $n_2/n(\text{O})$. We label the number densities n_i ($[n_i] = 1\text{ cm}^{-3}$) and statistical weights g_i of the three lowest energy levels in the OI system in ascending order of energy with indices $i = 1, 2, 3$, that is "1" for $^3\text{P}_2$, "2" for $^3\text{P}_1$, and "3" for $^3\text{P}_0$. The statistical weights are specified as $g_1 = 2 \times 2 + 1 = 5$, $g_2 = 2 \times 1 + 1 = 3$, $g_3 = 2 \times 0 + 1 = 1$. Since $n(\text{O}) \approx n_1 + n_2 + n_3$ we wish to calculate

$$\left(\frac{n_2}{n(\text{O})}\right) = \left[1 + \left(\frac{n_1}{n_2}\right) + \left(\frac{n_3}{n_2}\right)\right]^{-1}. \quad (4.18)$$

In a statistical equilibrium ($\dot{n}_1 = \dot{n}_2 = \dot{n}_3 = 0$) without radiation fields the rate equations for the populations of the three energy levels are given in matrix form

$$\begin{pmatrix} 0 \\ 0 \\ 0 \end{pmatrix} = \begin{pmatrix} -(C_{12} + C_{13}) & C_{21} + A_{21} & A_{31} + C_{31} \\ C_{12} & -(C_{21} + C_{23} + A_{21}) & C_{32} + A_{32} \\ C_{13} & C_{23} & -(C_{31} + C_{32} + A_{31} + A_{32}) \end{pmatrix} \begin{pmatrix} n_1 \\ n_2 \\ n_3 \end{pmatrix}. \quad (4.19)$$

The analytic solution for the relevant population ratios in Eq. 4.18 can be obtained via basic algebraic manipulation (e.g. Liseau *et al.* 2006). They are:

$$\left(\frac{n_2}{n_3}\right) = \frac{C_{13}(C_{32} + A_{32}) + C_{12}(C_{31} + C_{32} + A_{31} + A_{32})}{C_{12}C_{23} + C_{13}(C_{21} + C_{23} + A_{21})}, \quad (4.20)$$

$$\left(\frac{n_1}{n_2}\right) = \frac{(C_{31} + A_{31})(C_{21} + C_{23} + A_{21}) + (C_{32} + A_{32})(A_{21} + C_{21})}{(C_{32} + A_{32})(C_{12} + C_{13}) + C_{12}(A_{31} + C_{31})}. \quad (4.21)$$

The Einstein coefficients for spontaneous emission A_{ul} are taken from the NIST Atomic Database². In general, the total collisional rates C_{ul} and C_{lu} record all collisional contributions from all potential collision partners p such as atomic hydrogen H, molecular hydrogen H_2 , helium He, electrons e^- , etc. Mathematically, we take them into account with the two equations

$$C_{ul} = \sum_p n_p q_{ul}^p(T_{\text{ex}}) \quad \text{and} \quad C_{lu} = \sum_p n_p q_{lu}^p(T_{\text{ex}}), \quad (4.22)$$

where the temperature dependent collisional excitation/de-excitation rate coefficients (q_{lu}^p and q_{ul}^p) are introduced. Consequently, the total number density of all collision partners is $n_{\text{coll}} = \sum_p n_p$. Both quantities q_{lu}^p and q_{ul}^p are linked via the

² $A_{21} = 8.91 \times 10^{-5} \text{ s}^{-1}$, $A_{32} = 1.75 \times 10^{-5} \text{ s}^{-1}$, $A_{31} = 1.34 \times 10^{-10} \text{ s}^{-1}$ from https://physics.nist.gov/PhysRefData/ASD/levels_form.html

Boltzmann statistics

$$q_{lu}^p(T_{\text{ex}}) = q_{ul}^p(T_{\text{ex}}) \left(\frac{g_u}{g_l} \right) \exp\left(-\frac{E_{ul}}{k_B T_{\text{ex}}}\right), \quad (4.23)$$

so that for a given (excitation) temperature T_{ex} one collisional rate coefficient can be calculated from the corresponding other one. Warm, interstellar gas at $T < 5000$ K is mostly composed of atomic hydrogen and shows very low ionisation fractions. Therefore, we naturally expect atomic hydrogen to be the sole decisive collisional partner, that is $n_{\text{coll}} \approx n_{\text{H}}$. Lique *et al.* (2018) provides a list of collisional rate coefficients for oxygen with atomic hydrogen (q_{lu}^{H} and q_{ul}^{H}) for $T_{\text{ex}} \sim 100$ – 8000 K, which are used in our calculations. With that, we can plot the analytical solution of $n_2/n(\text{O})$ for five selected temperatures and a density range of $n_{\text{coll}} \sim 10^3$ – 10^7 cm^{-3} (see Fig. 4.7).

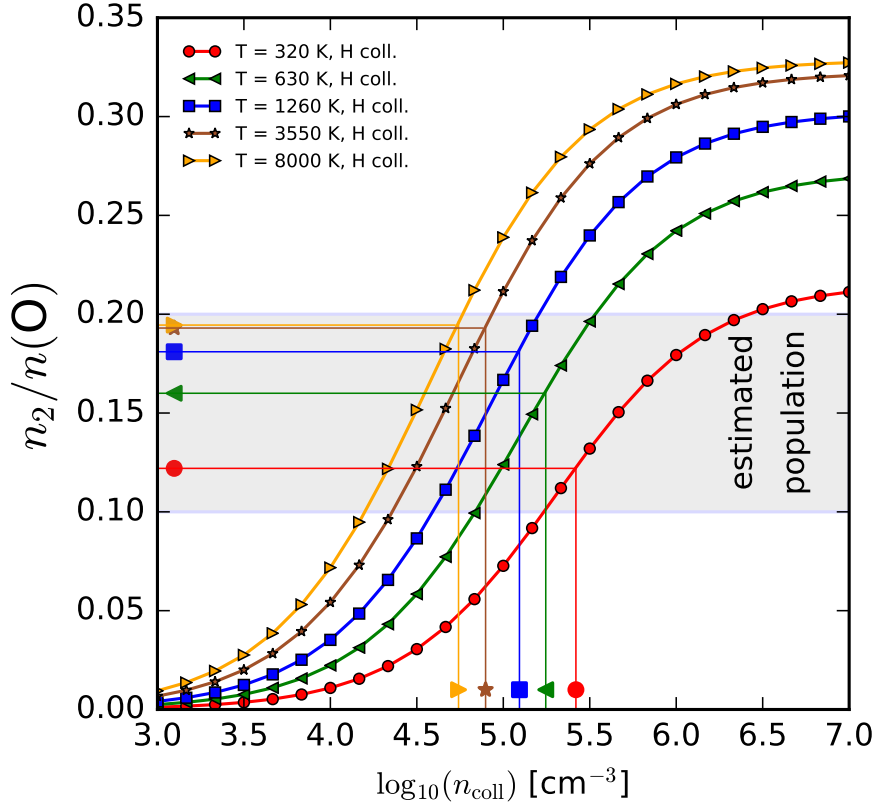


Fig. 4.7. The analytical solution of $n_2/n(\text{O})$ for five selected temperatures. Critical densities for each temperature are marked as straight lines. Under the assumption that the gas density of the warm outflow component traced by the $[\text{O}]\text{I}_{63}$ emission line is close to the critical density the ratio $n_2/n(\text{O})$ can be constrained to be in a narrow population stripe, that is $n_2/n(\text{O}) \sim 0.1$ – 0.2 .

The resulting graphs are monotonically increasing functions ranging between 0.00 (low-density limit) to about 0.35 (high-density limit). However, in regions where the $[\text{O}]\text{I}_{63}$ emission line is prominently detected extremely low level pop-

ulations (3P_1) close to 0.0 certainly do not prevail. A useful parameter constraining the level population in a sensible way is the critical density n_{crit} . The critical density is defined as density at which the rate of collisional de-excitation equals the rate of radiative de-excitation for a given excited state $E_k > E_i$, that is

$$n_{\text{crit,H}}(k; T_{\text{ex}}) = \frac{\sum_{i<k} A_{ki}}{\sum_{i\neq k} q_{ki}^{\text{H}}(T_{\text{ex}})}. \quad (4.24)$$

For $n \ll n_{\text{crit}}$ almost each collision leads to an emission of a photon, whereas for $n \gg n_{\text{crit}}$ the collisional de-excitation dominates and the emission is thermalised. It is reasonable to assume that the gas density in the warm, dense outflow component traced by the $[\text{O I}]_{63}$ emission line is close to the critical density.

If the gas density were much lower than the critical density, then the 3P_1 energy level would not be sufficiently populated and in turn the $[\text{O I}]_{63}$ emission line would not be detected. In addition, we expect the $[\text{O I}]_{63}$ emission line to be sub-thermally excited. Thermalisation of the $[\text{O I}]_{63}$ emission line becomes important at very high densities ($n_{\text{coll}} > 10^6 \text{ cm}^{-3}$), which are much higher than densities typically measured along protostellar jet beams (e.g. Bacciotti and Eisloffel 1999). Therefore, we constrain the population ratio $n_2/n(\text{O})$ to be in a narrow population stripe (see Fig. 4.7) that corresponds to the range of critical densities for $T \sim 300\text{--}8000 \text{ K}$. Hence, we estimate $n_2/n(\text{O}) \sim 0.1\text{--}0.2$ in Equ. 4.17 leading to the final equation

$$\left(\frac{\dot{M}_{\text{out}}}{M_{\odot} \text{yr}^{-1}} \right) = (3.3 - 6.7) \times 10^{-3} \cdot \left(\frac{v_t}{\text{km s}^{-1}} \right) \left(\frac{''}{\theta} \right) \left(\frac{\text{pc}}{D} \right) \left(\frac{L([\text{O I}]_{63})}{L_{\odot}} \right). \quad (4.25)$$

In conclusion, from the reasonable assumption that the $[\text{O I}]_{63}$ emission line is collisionally excited in the flowing material the outflow geometry itself dictates the mass-loss rate.

CHAPTER 5

First fully mapped [O I] outflows with SOFIA

5.1 Morphology and schematics

In this section we briefly describe the morphology of the obtained [O I]₆₃ maps of the observed targets. An even more detailed description is presented in Sperling *et al.* (2020) and Sperling *et al.* 2021 (submitted). In addition, we interpret these maps by putting forward schematics that illustrate the potential origin of the detected [O I]₆₃ emission. The underlying reason for this analysis is to evaluate the applicability of the Hollenbach and McKee (1989) shock model and ultimately to prevent a blind exploitation of Eq. 4.5.

In the Figures 5.1–5.8 green and yellow boxes enclose the carefully selected regions where the flux measurements were taken to derive mass-loss rates (see Section 5.3). The evidence of the [O I]₆₃ line detection towards all relevant emission regions is presented in Section 5.2.

5.1.1 Cep E

The continuum subtracted [O I]₆₃ map (Fig. 5.1) reveals a bright and extended [O I]₆₃ emission knot A located about 20'' south of the continuum source IRAS 23011+6126 (Lefloch *et al.* 1996), that drives the Cep E outflow (Ayala *et al.* 2000; Eislöffel *et al.* 1996). This emission coincides with the Herbig-Haro object HH 377 (Devine *et al.* 1997). HH 377 is a weak bow shock region (Ayala *et al.* 2000) featuring very bright H₂ and almost no [Fe II] emission in the near-infrared (Eislöffel *et al.* 1996). Thus, the bright [O I]₆₃ emission at knot A is connected to a mainly non-dissociative bow shock.

On the opposite side to knot A in north-east direction a prominent 35'' long jet like structure is detected in [O I]₆₃. However, the same region reveals a highly complex and knotty internal structure seen prominently in H₂ (Ladd and Hodapp 1997), but not in H α , optical [S II], or near-infrared [Fe II]. Therefore, this emission is likely connected to multiple, spatially unresolved, non-dissociative shocks.

At the location of IRAS 23011+6126 no significant [O I]₆₃ emission is detected. Together with lack of other emission lines such as H₂, [Fe II], and H α , we conclude that the Cep E driving source must be deeply embedded or currently inactive.

Giannini *et al.* (2001) analysed the $[\text{C II}]_{158}/[\text{O I}]_{63}$ line ratio towards both lobes of Cep E. They found values on the order of $[\text{C II}]_{158}/[\text{O I}]_{63} \sim 1$ indicating that some part of the observed $[\text{O I}]_{63}$ emission is not connected to shocks but to the presence of a PDR region.

5.1.2 HH 1

Most of the detected [O I] emission in Fig. 5.2 coincides with the location of the well-studied optical HH 1 jet (e.g. Bally *et al.* 2002a; Eisloffel *et al.* 1994; Raga *et al.* 2011). The HH 1 jet is a collimated outflow featuring a series of bright clumpy knots and complex filamentary internal structures (Hartigan *et al.* 2011). We therefore interpret the [O I] emission towards the HH 1 jet as coming from multiple internal shocks and their associated working surfaces.

The brightest [O I] emission knot about $5''$ north-west from the driving source VLA1 (Pravdo *et al.* 1985; Rodríguez *et al.* 2000) coincides with the location of HH 501 (Hester *et al.* 1998). Strong near-infrared [Fe II] emission has been found towards HH 501 Davis *et al.* (2000) indicating the presence of a dissociative J-shock. The driving source VLA1 is highly obscured by a dense molecular envelope, since faint [O I] emission and no near-infrared H_2 , [Fe II] has been detected towards it (Davis *et al.* 2000).

Some clumpy [O I] emission is detected about $65''$ north-west from VLA1, that is the location of HH 1. High-resolution observations in the optical in $\text{H}\alpha$ and [S II] with HST reveal that HH 1 features multiple bow shocks, internal emission knots, and filamentary structures (Hartigan *et al.* 2011). Thus, this [O I] emission may be directly connected to the cooling zones behind the existing leading bow shocks. Towards VLA1 and HH 1 line ratios on the order of $[\text{C II}]_{158}/[\text{O I}]_{63} \sim 1-2$ have been measured by Giannini *et al.* (2001) indicating that an unknown amount of the observed [O I] emission may originate from the impact of a PDR region.

5.1.3 HH 212

HH 212 is a highly symmetric, parsec-scale outflow prominently visible in the molecular transitions of H_2 (McCaughrean *et al.* 2002; Zinnecker *et al.* 1998), SiO (Cabrit *et al.* 2007; Codella *et al.* 2007), and CO (Gueth and Guilloteau 1999; Lee *et al.* 2006). Remarkably, this symmetry is reflected in our obtained continuum subtracted $[\text{O I}]_{63}$ maps (Fig. 5.3). Two bright $[\text{O I}]_{63}$ emission regions (knot A and knot B) are located opposite to each other with IRAS 05413–0104 (Froebrich 2005) roughly in the middle. The detected $[\text{O I}]_{63}$ emission matches very well the mid-infrared [Fe II] and [S I] emission (Anderson *et al.* 2013) and near-infrared [Fe II] emission (Caratti o Garatti *et al.* 2006; Smith *et al.* 2007) indicating the presence of dissociative J-shocks at both knots. Strong disk wind signatures have been de-

tected at the HH212 driving source (Lee *et al.* 2018) – some of the [O I]₆₃ emission may be connected to this disk wind. Further downstream in both lobes, that is towards knots SK2 and NK2 and beyond, the [O I]₆₃ emission rapidly fades out. The lack of [O I]₆₃ emission towards these regions indicates that non-dissociative shocks cause the bright H₂ emission at these knots.

5.1.4 HH 26

HH 26 is part of the complex region HH 24-26 that shows on-going star formation (e.g. Benedettini *et al.* 2000; Bontemps *et al.* 1995; Davis *et al.* 1997, 2002, 2011a). The Class I protostar HH 26 IR drives the HH 26A/C/D chain that is (in parts) prominently seen in our obtained [O I]₆₃ map, (Fig. 5.4).

We detect almost no [O I]₆₃ emission on the driving source HH 26 IR itself. A small-scale H₂ jet at HH 26 IR pointing towards HH 26A has been detected by Davis *et al.* (2002). However, this jet could not be detected in near-infrared [Fe II] emission (Antoniucci *et al.* 2008; Davis *et al.* 2011a). Our observations are consistent with the interpretation given by Antoniucci *et al.* (2008) that the small-scale jet driven by HH 26 IR is mainly molecular and the associated shocks are predominantly non-dissociative.

In Fig. 5.4, bright and extended [O I]₆₃ emission is detected at the location of K_1 and K_2 coinciding with knot C of the HH26A/B/C chain (see nomenclature in Chrysostomou *et al.* 2000). Chrysostomou *et al.* (2002) proposed that this emission represents a shock excited region, where the jet has struck the ambient medium. In this scenario HH 26C is interpreted as the deflected, terminal bow shock, which was not mapped here. Spectroscopic observations at different locations within the HH 26 region (Benedettini *et al.* 2000; Giannini *et al.* 2004) support this assumption that the observed [O I]₆₃ emission in the blue-lobe towards HH 26A is mainly due to shock excitation, i.e. not due to the presence of a strong FUV field (Benedettini *et al.* 2000).

The very faint blue-shifted [O I]₆₃ emission at K_3 appears to be rather non-physical, since it lies in the red-shifted outflow lobe (Davis *et al.* 1997; Dunham *et al.* 2014). Like in the case of HH 34 we therefore interpret this emission at K_3 as a noise feature.

5.1.5 HH 34

Three potentially interesting [O I]₆₃ emission regions (K_1 , K_2 , K_3) can be noticed towards HH 34 in Figure 5.5.

At the driving source of the HH 34 jet (knot K_1), we detected some clumpy [O I]₆₃ emission. This emission is potentially linked to shock-excited gas in a jet/counter jet outflow region. Near-infrared observations in [Fe II] and H₂ at the jet basis of

HH 34 support this conclusion (Davis *et al.* 2003, 2011a; Garcia Lopez *et al.* 2008). A potential disk around HH 34 IRS might contribute to the detected [O I]₆₃ emission (Rodríguez *et al.* 2014).

The HH 34 jet, that is located between the crosses E and L in Figure 5.5, is prominently visible in [SII] λ 6716, [O I] λ 6300, less bright in H α , and features numerous knots within the jet body (Bacciotti and Eisloffel 1999; Podio *et al.* 2006; Reipurth *et al.* 2002). The relatively strong optical [SII] λ 6716 emission in the HH 34 jet indicates low shock velocities in the emitting gas (Hartigan *et al.* 1994). Compared with HH 111 no far-infrared counterpart of the optical jet is seen between knot E and L in our obtained maps. This is surprising, since there are several demonstrable similarities between the HH 111 jet and the HH 34 jet (e.g. Reipurth *et al.* 2002). In the near-infrared the HH 34 jet is prominently seen in [Fe II] and H₂ (e.g. Antonucci *et al.* 2014b; Garcia Lopez *et al.* 2008; Podio *et al.* 2006), and [Fe II] peaks where [SII] λ 6716 peaks. So, both lines ([Fe II], [SII] λ 6716) are likely to be excited in J-shocks at the apices of the internal bow shocks (Antonucci *et al.* 2014b; Podio *et al.* 2006). The non-detection of a [O I]₆₃ jet can either be a result of the too low shock velocities within the HH 34 jet or the [O I]₆₃ jet is indeed present, but too faint to be detected.

Looking at the obtained spectra at the location of K_2 and K_3 (see Figure 5.5) we notice that the line fit suggests a red-shifted outflow towards HH 34S. Physically, this is puzzling, since the jet towards HH 34S is blue-shifted. The morphology of this [O I]₆₃ emission at K_2 and K_3 would be difficult to explain, if this emission is connected to the outflow. The most obvious explanation then could be that this emission is part of a backflow along the cocoon of material surrounding the jet (Cabrit 1995; Norman 1990). Alternatively, noise at 63 μ m towards longer wavelengths mimics an emission line so that the line fit procedure falsely identifies this noise feature as a red-shifted [O I]₆₃ line.

5.1.6 HH 111

Prominent [O I]₆₃ emission is detected towards the driving source of the HH 111 jet (see Fig. 5.6). This emission is slightly extended along the outflow axis and potentially originates from a quasi-spherical wind shock driven by HH 111IRS and the forming disk.

The far-infrared counterpart of the optical HH 111 jet is first detected in [O I]₆₃ in our maps and shows a clumpy internal structure with most emission coming from the innermost part of the jet. The extent of the detected jet body is about 45'' corresponding to a physical length of about ~ 0.1 pc at 420 pc. High resolution observations in the optical (Reipurth 1989; Reipurth *et al.* 1997) and in the near-infrared (Davis *et al.* 1994; Nisini *et al.* 2002) revealed the presence of mul-

multiple internal emission knots in the HH 111 jet. These knots are shock excited regions (unresolved in our maps) and cause the bright [O I]₆₃ emission towards HH 111. The spatial distribution of the [O I]₆₃ emission in HH 111 follows roughly the near-infrared [Fe II] emission (Nisini *et al.* 2002) indicating presence of several dissociative shocks.

5.1.7 L1551 IRS5

The infrared source IRS5 (Strom *et al.* 1976) in the molecular dark cloud L1551 drives powerful bipolar outflows, which are associated with various Herbig-Haro objects (e.g. Devine *et al.* 1999; Fridlund and Liseau 1994; Hayashi and Pyo 2009). At IRS 5 in Fig. 5.7, we detect bright and extended [O I]₆₃ emission stretching out alongside an axis of $\sim 250^\circ$ P.A. (position angle measured in an easterly direction from north), which is consistent with the directions of the northern and southern jets seen in near-infrared [Fe II] (Itoh *et al.* 2000; Pyo *et al.* 2009) or H₂ (Davis *et al.* 2002). A measured [O I]₆₃/[C II]₁₅₈ line ratio of about 7.3 towards IRS 5 (White *et al.* 2000) mainly excludes a significant PDR contribution to the [O I]₆₃ emission. Thus, most of the blue-shifted [O I]₆₃ emission is likely connected to the 5'' initial sector of the northern jet. This part of the jet is also prominently visible in H α and [S II] (Fridlund *et al.* 2005). Conclusively, most of the detected [O I]₆₃ is caused by mostly dissociative shocks, which are likely of J-type (Lee *et al.* 2014b). A very faint counter jet northeast of IRS 5 was first detected in [Fe II] by Hayashi and Pyo (2009). Some spaxels in this region show a redshifted [O I]₆₃ emission line indicating that this small-scale counter jet is tentatively detected in our maps.

5.1.8 SVS 13

The SVS 13 region in NGC 1333 is associated with a chain of feature-rich Herbig-Haro objects (HH 7-HH 11, e.g. Bachiller *et al.* 2000; Dionatos and Güdel 2017; Herbig 1974). Fortunately, this region has been mapped in great detail with HST revealing a consistent schematic view of the HH 7-11 outflow (see Fig. 12 in Hartigan *et al.* 2019).

Since Dionatos and Güdel (2017) detected only faint [C II]₁₅₈ emission towards SVS 13, we interpret the [O I]₆₃ emission in Fig. 5.8 as mostly coming from shock excited gas connected to the outflow.

We detect extended and very strong [O I]₆₃ emission at the driving source of HH 7-11 (IRAS 03259+3105). This innermost region at SVS 13 is associated with multiple outflows (e.g. Lefèvre *et al.* 2017; Noriega-Crespo *et al.* 2002). Hodapp and Chini (2014) revealed the presence of a microjet traced by shock-excited [Fe II] and a series of expanding bubble fragments seen in H₂. Since we detect most of

the [O I]₆₃ emission from that inner region, we interpret this originating from bow shock fronts of the bubble and the interaction zone, where the microjet potentially pierces the bubble. However, strong wind shocks from one or more continuum sources can also be responsible for the [O I]₆₃ emission at SVS 13.

HH 11 is not detected in [O I]₆₃, which is consistent with it being a high excitation region mostly visible in H α . The detection of bright [O I]₆₃ emission at the location of HH 7 strongly supports the notion of it being the terminal bow shock region of the HH 7-11 outflow (e.g. Hartigan *et al.* 2019; Smith *et al.* 2003). HH 7 has a remarkable complex internal substructure (HH 7A, 7B, 7C, spatially unresolved in our maps) from which the detected [O I]₆₃ emission in principle can arise. Based on near-infrared H₂ observations, Smith *et al.* (2003) offer two shock model predictions for imaging of the HH 7 region at [O I]₆₃ (see Fig. 13 and 14 in Smith *et al.* 2003). The observed [O I]₆₃ emission, i.e. an intense compact knot together with a slightly blue-shifted line profile at HH 7, are consistent with the dissociative J-type paraboloidal bow shock model. However, recent spectroscopic observations of pure rotational H₂ lines at HH 7 are more in agreement with a non-dissociative C-type molecular shock (Neufeld *et al.* 2019). Molinari *et al.* (2000) reported signatures of both, C-type and J-type, shocks in the HH 7-11 region illustrating the complex shock structure of the HH 7-11 outflow.

The diffuse and extended [O I]₆₃ emission in our obtained maps at HH 8 and HH 10 can be interpreted as a jet deflection region (Bachiller *et al.* 2000; Hartigan *et al.* 2019), i.e. a location where the outflow strikes the ambient medium leading to a substantial change in direction. In this scenario HH 7 appears to be off the HH 11-HH 10-HH 8 chain due to that deflection.

The HH 9 knot features no [Fe II] and only very faint H₂ emission (Khanzadyan *et al.* 2003). We detect some [O I]₆₃ emission vaguely around HH 9. Due to its location at the cavity wall around the HH 7-11 outflow (Hartigan *et al.* 2019) we suspect that some entrained or deflected material turbulently shocks the ambient medium.

5.1.9 HH 30

The prototypical jet/disk system associated with HH 30 is situated in the molecular dark cloud L1551 in Taurus (Mundt and Fried 1983). Observations in the optical reveal a prominent jet/counterjet structure (e.g. Estalella *et al.* 2012; Graham and Heyer 1990; Mundt *et al.* 1988). In the near-infrared transitions of H₂ and [Fe II] no clear sign of large-scale jet emission is seen towards HH 30 (Hayashi and Pyo 2009). Only very faintly [Fe II] emission has been detected close to HH 30 IRS. We detect no continuum and [O I]₆₃ emission towards HH 30. This seems unsurprising, since HH 30 is the least luminous and most evolved target in our sample.

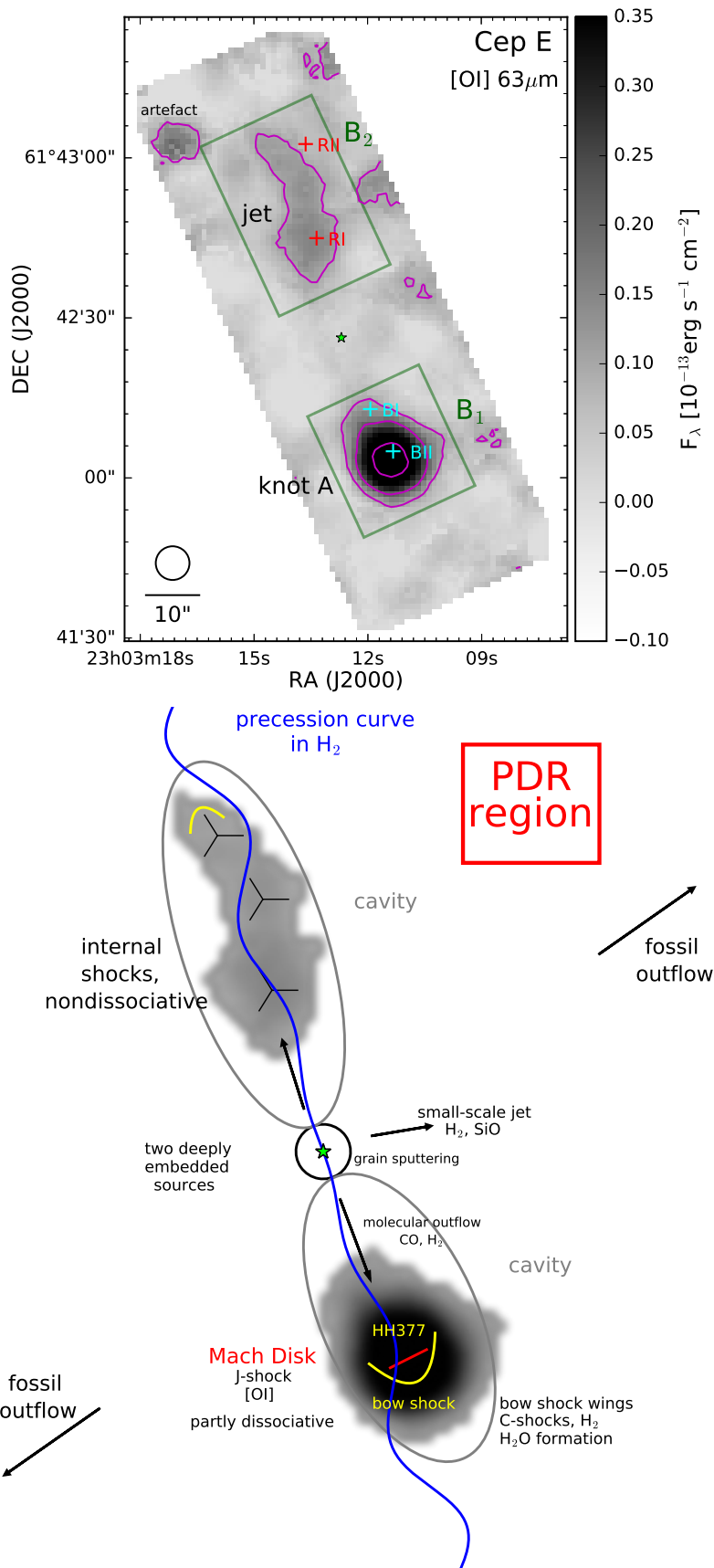


Fig. 5.1. The continuum subtracted [O I]₆₃ map of Cep E (top) and a corresponding schematic of the detected emission (bottom). For better orientation we mark the positions of the known blue-shifted (BI, BII Gómez-Ruiz *et al.* 2012) and red-shifted (RI, RII Gusdorf *et al.* 2017) emission knots, which are detected in the Spitzer-IRAC band-two (4.5 μm) image.

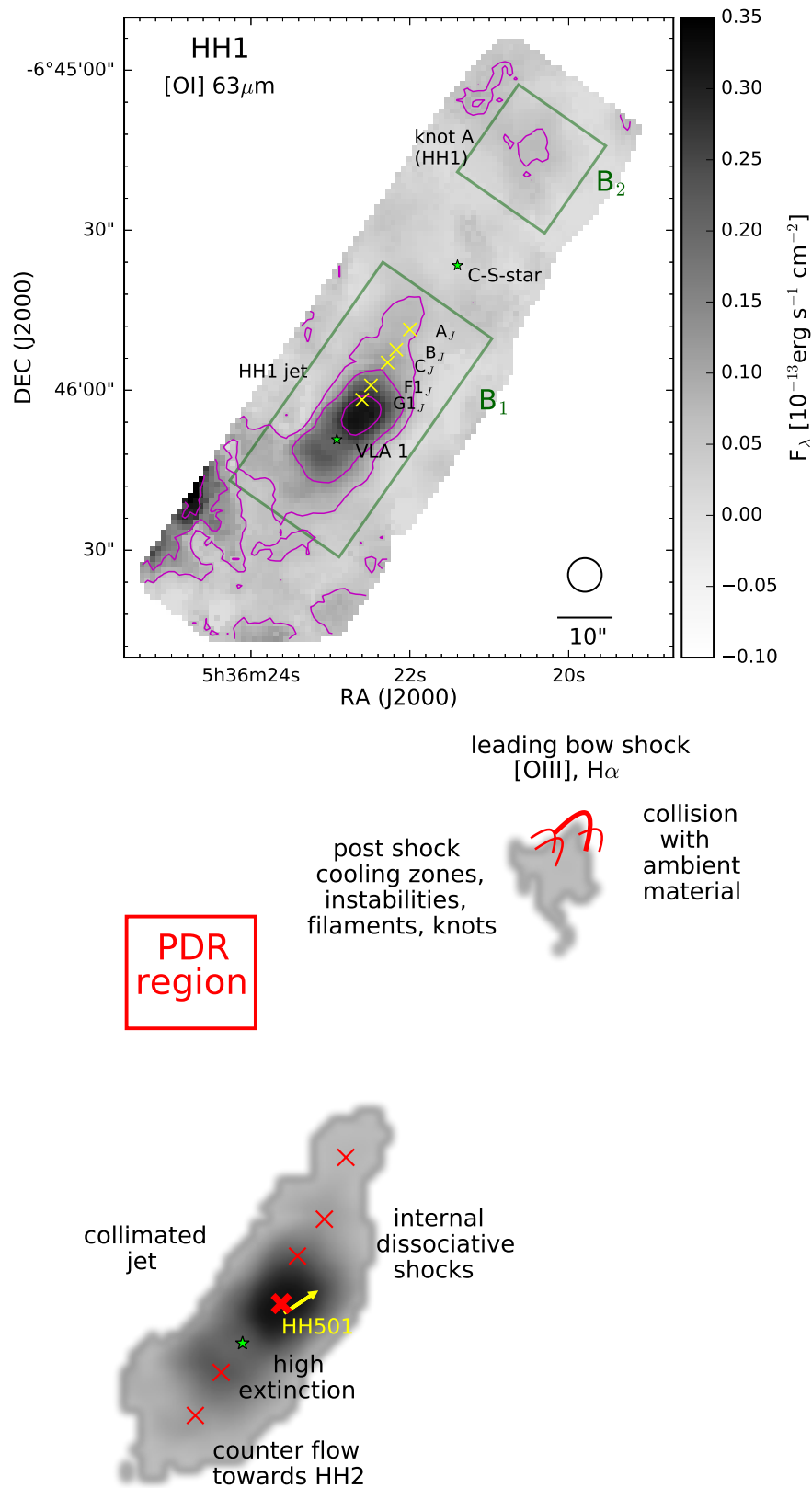
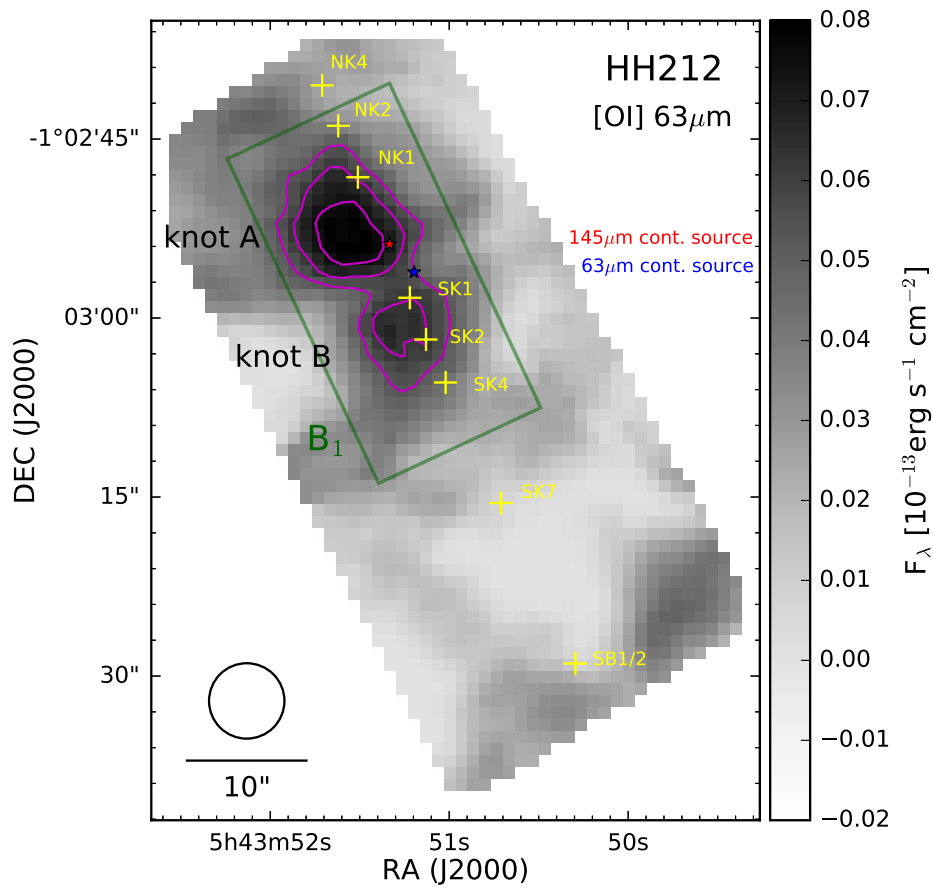


Fig. 5.2. The continuum subtracted [OI]₆₃ map of HH 1 (top) and a corresponding schematic of the detected emission (bottom). Yellow crosses indicate the positions of a few selected optical knots (Bally *et al.* 2002a).



nondissociative
shocks at NK2–NK4

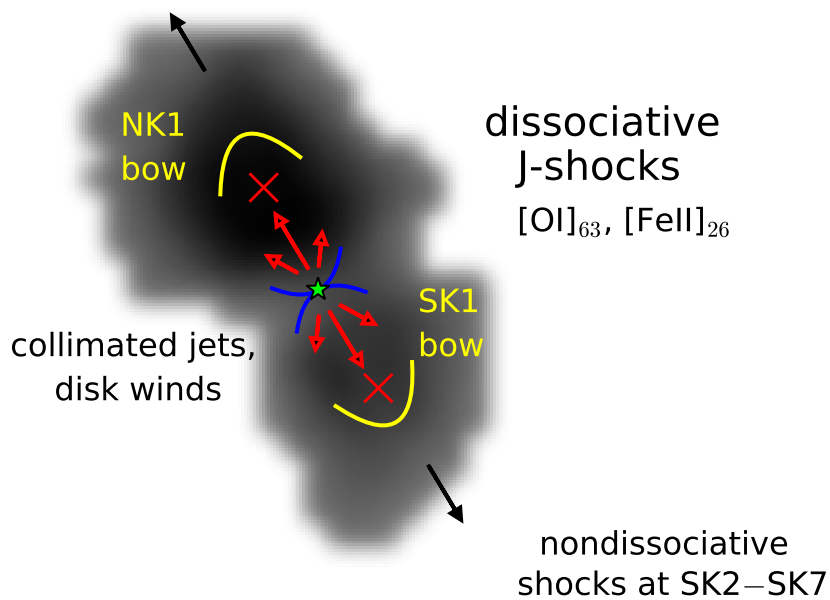


Fig. 5.3. The continuum subtracted [O I]₆₃ map of HH 212 (top) and a corresponding schematic of the detected emission (bottom). Yellow crosses indicate the positions of the prominent H₂ knots (Zinnecker *et al.* 1998).

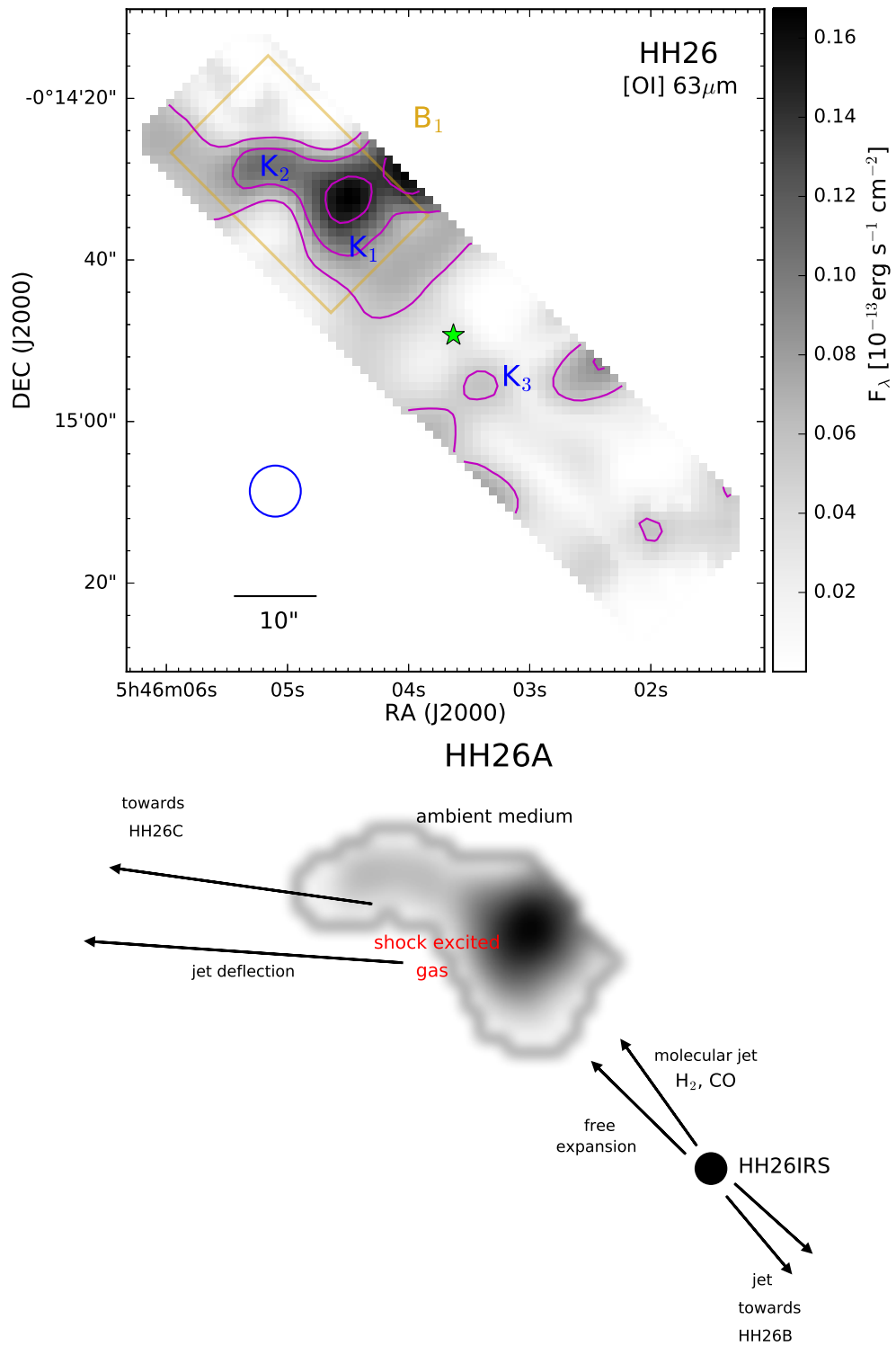


Fig. 5.4. The continuum subtracted [OI]₆₃ map of HH 26 (top) and a corresponding schematic of the detected emission (bottom).

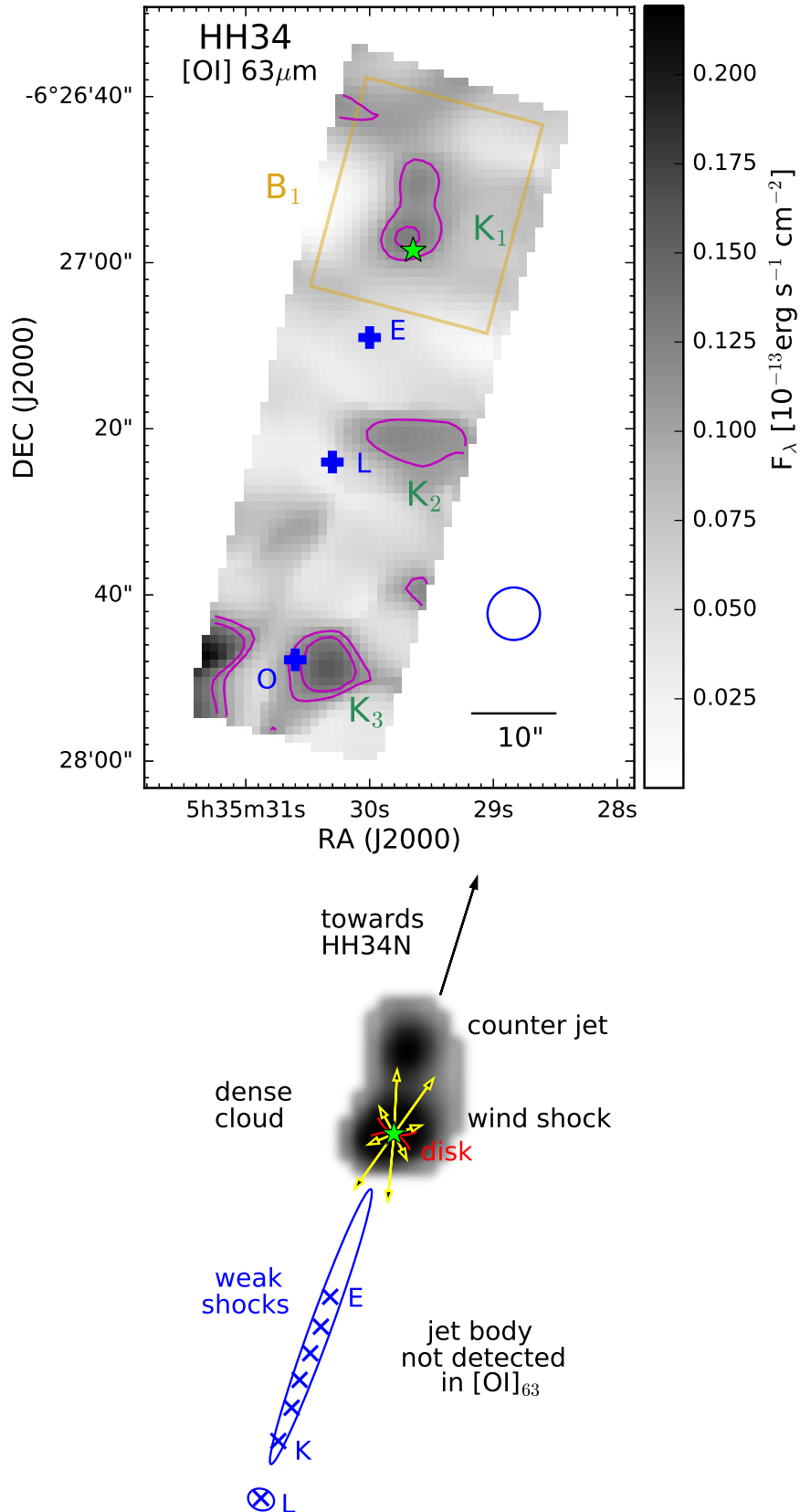


Fig. 5.5. The continuum subtracted [OI]₆₃ map of HH 34 (top) and a corresponding schematic of the detected emission (bottom). Serving as orientation, we mark the positions of knots E and L in between which the well-known optical jet is located (Heathcote and Reipurth 1992).

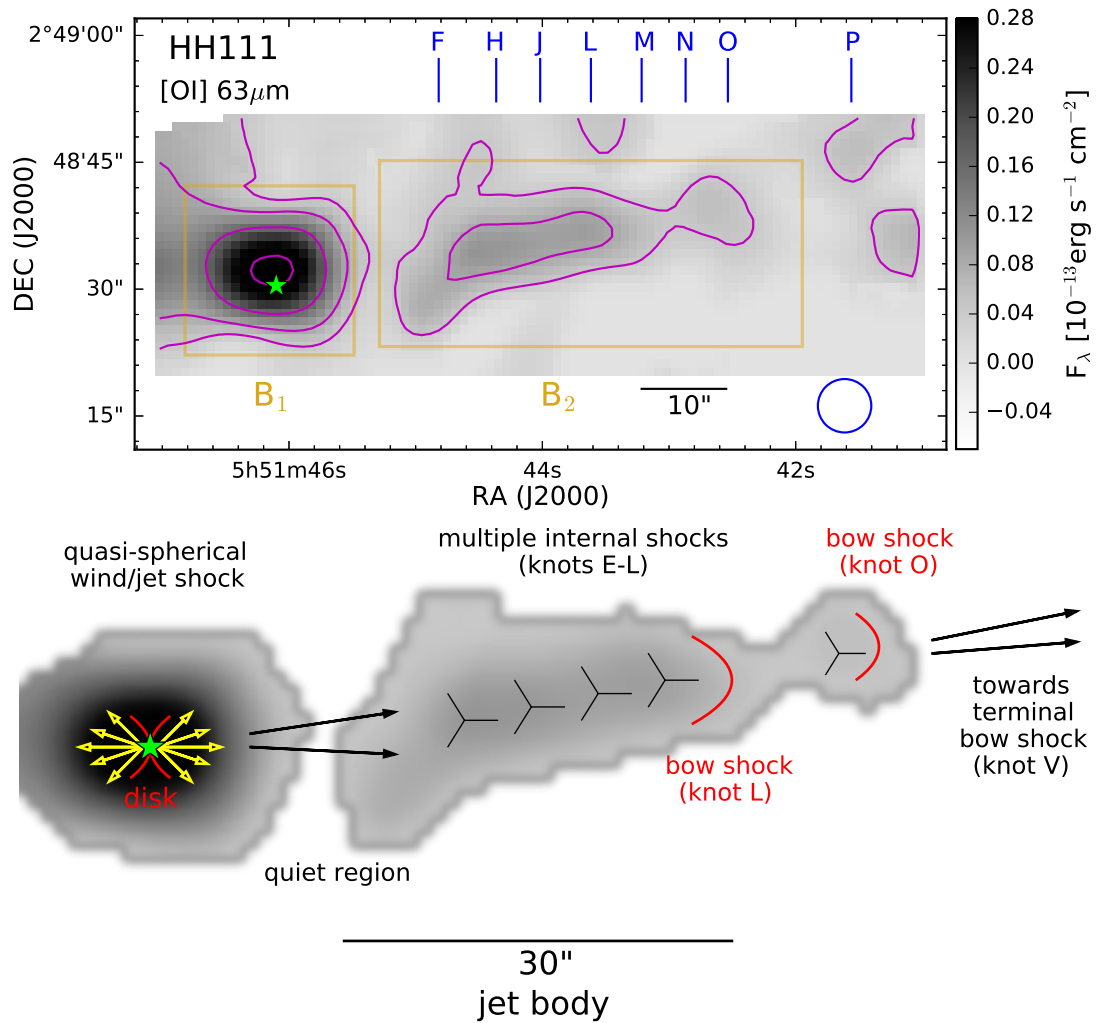


Fig. 5.6. The continuum subtracted [OI]₆₃ map of HH 111 (top) and a corresponding schematic of the detected emission (bottom). For better orientation we mark the positions in right ascension of a few bright optical knots as blue lines (notation from Reipurth 1989).

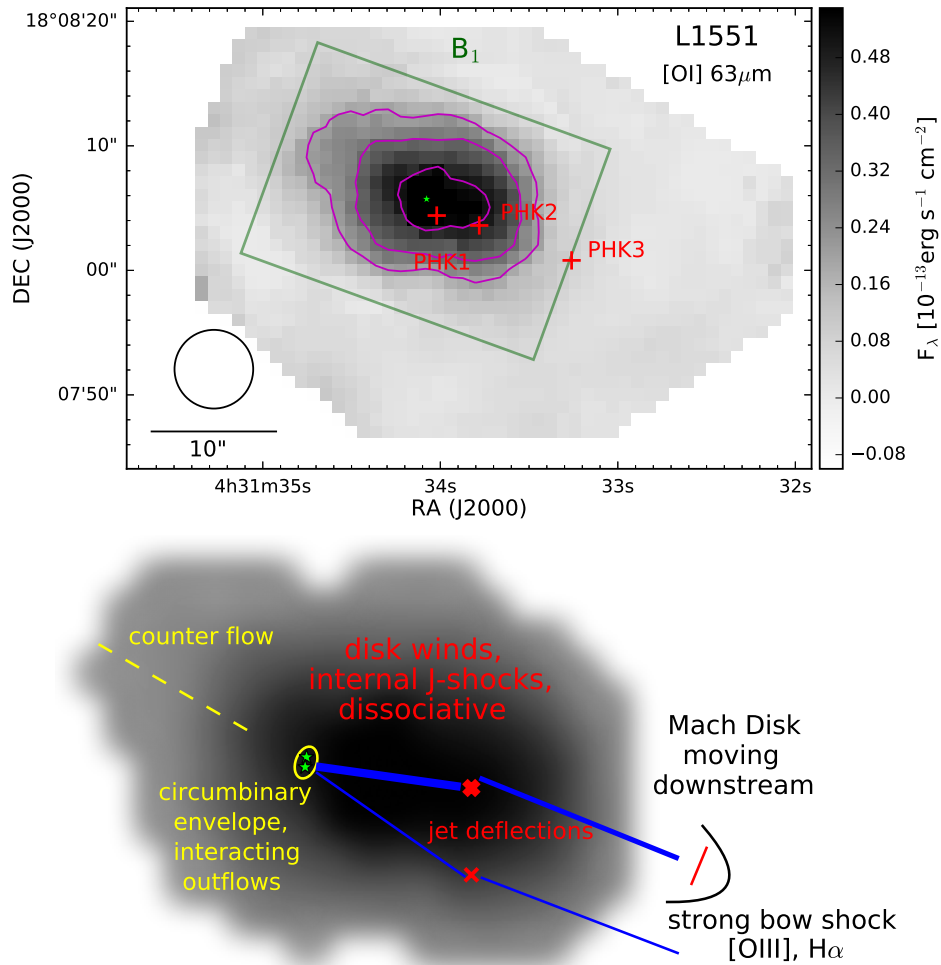


Fig. 5.7. The continuum subtracted [OI]₆₃ map of L1551 IRS5 (top) and a corresponding schematic of the detected emission (bottom). Serving as orientation, we marked the positions of the [Fe II] emission knots PHK2 and PHK3 (red crosses) as well as the brightest parts of the northern and southern jets (blue lines, Pyo *et al.* 2009).

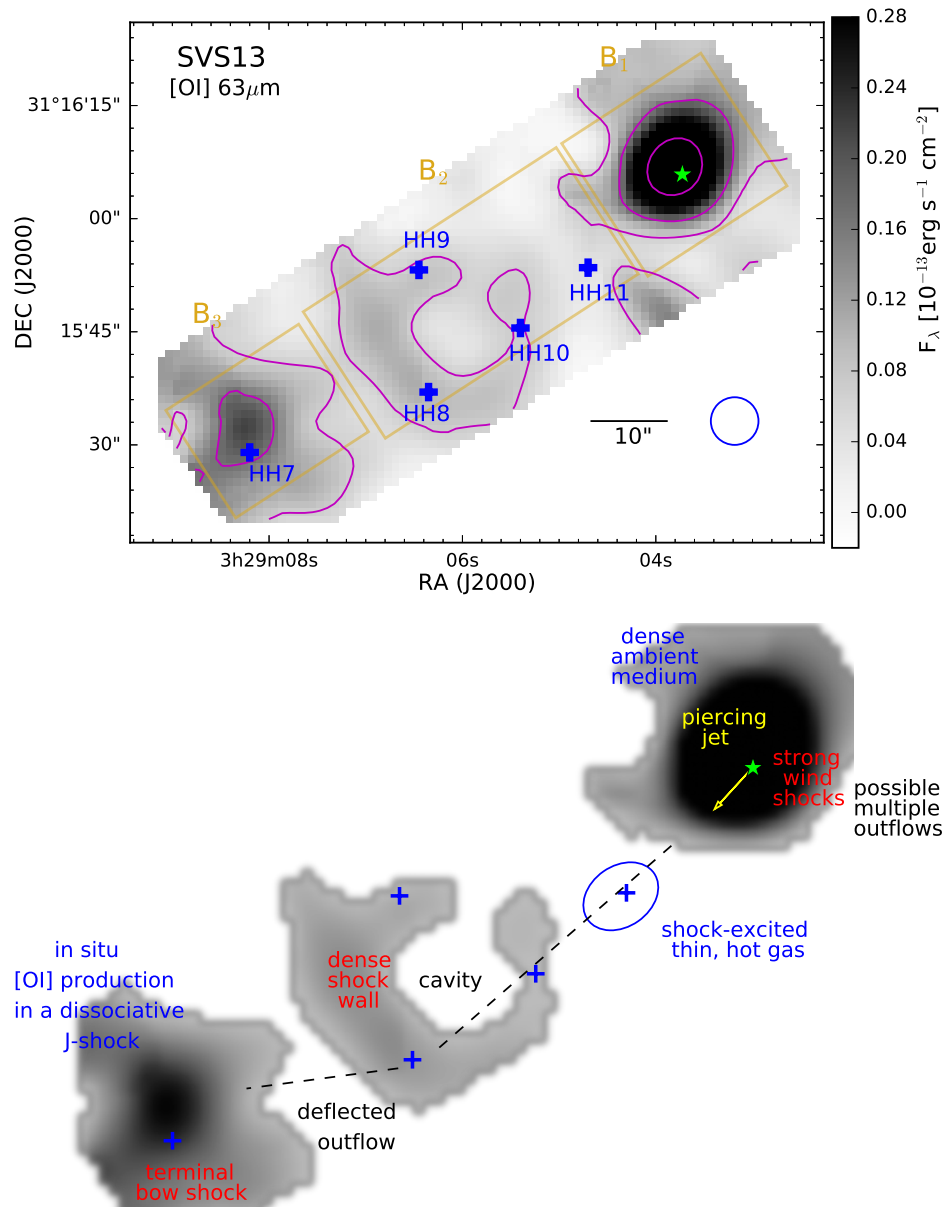


Fig. 5.8. The continuum subtracted [OI]₆₃ map of SVS 13 (top) and a corresponding schematic of the detected emission (bottom). Blue crosses in the [OI]₆₃ map indicate the positions of HH 7-11 (coordinates taken from Bally *et al.* 1996).

5.2 Line Detections

Sample spectra of the detected [OI] lines in different regions towards the observed outflows are presented in Figs. 5.9–5.17. Green solid lines indicate the atmospheric transmission at both relevant oxygen transitions. The fitted model function (Eq. 4.1) is plotted as a solid blue line in each spaxel. Vertical dashed red lines mark the position of the rest wavelengths of the [OI] emission lines. The spaxel coordinates are marked in the top right corner.

On account of the medium spectral resolution of FIFI-LS we did not extract any velocity information from the fitted emission line parameters. The observed [OI]₆₃ linewidths ΔV_{obs} are on the order of 180–350 km s⁻¹ indicating that this line is spectrally unresolved in all our targets. Typical signal-to-noise (SNR) ratios for the [OI]₆₃ emission line are on the order of SNR \sim 3–30. In contrast, the [OI]₁₄₅ line is at noise level in most spaxels of our maps.

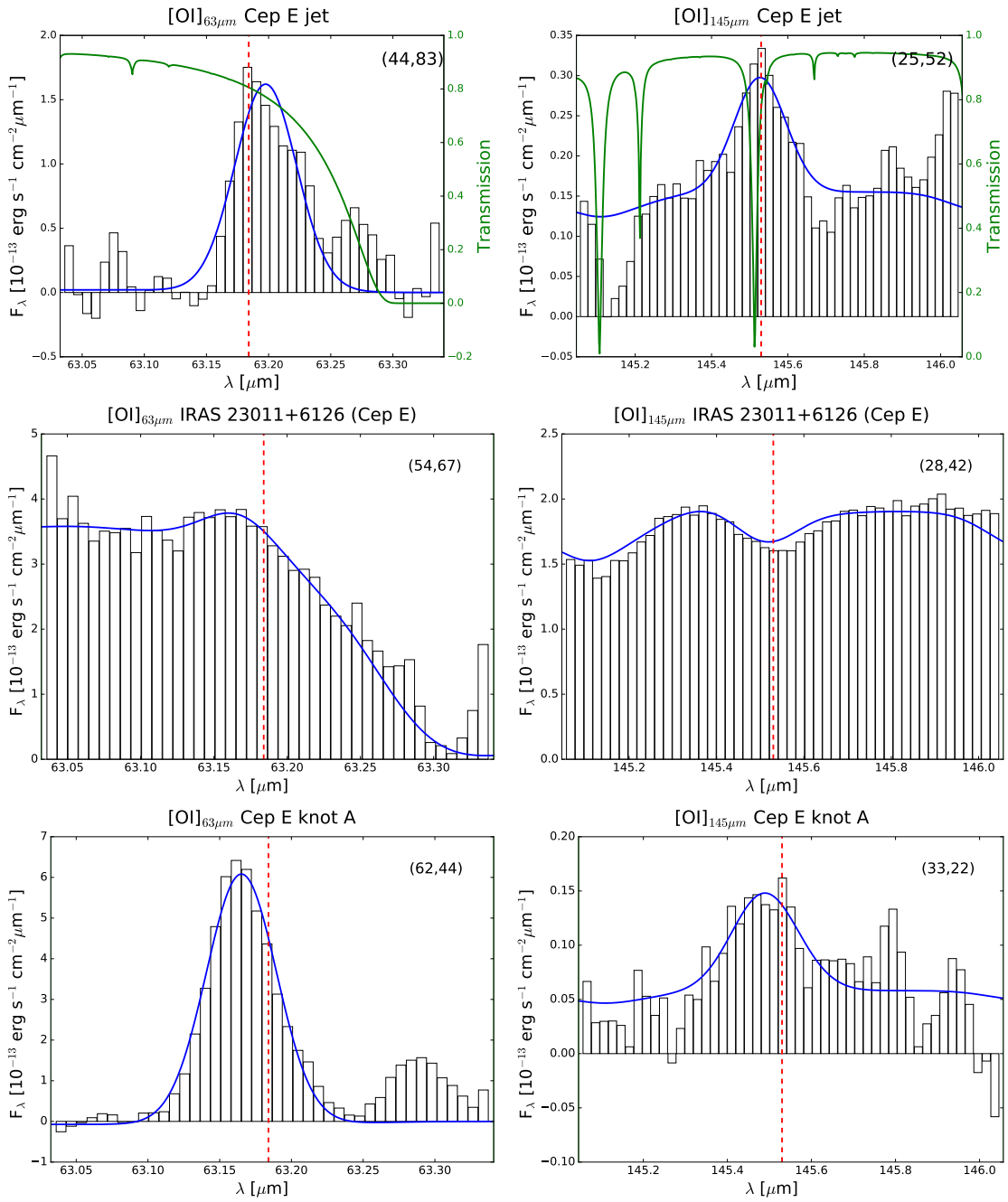
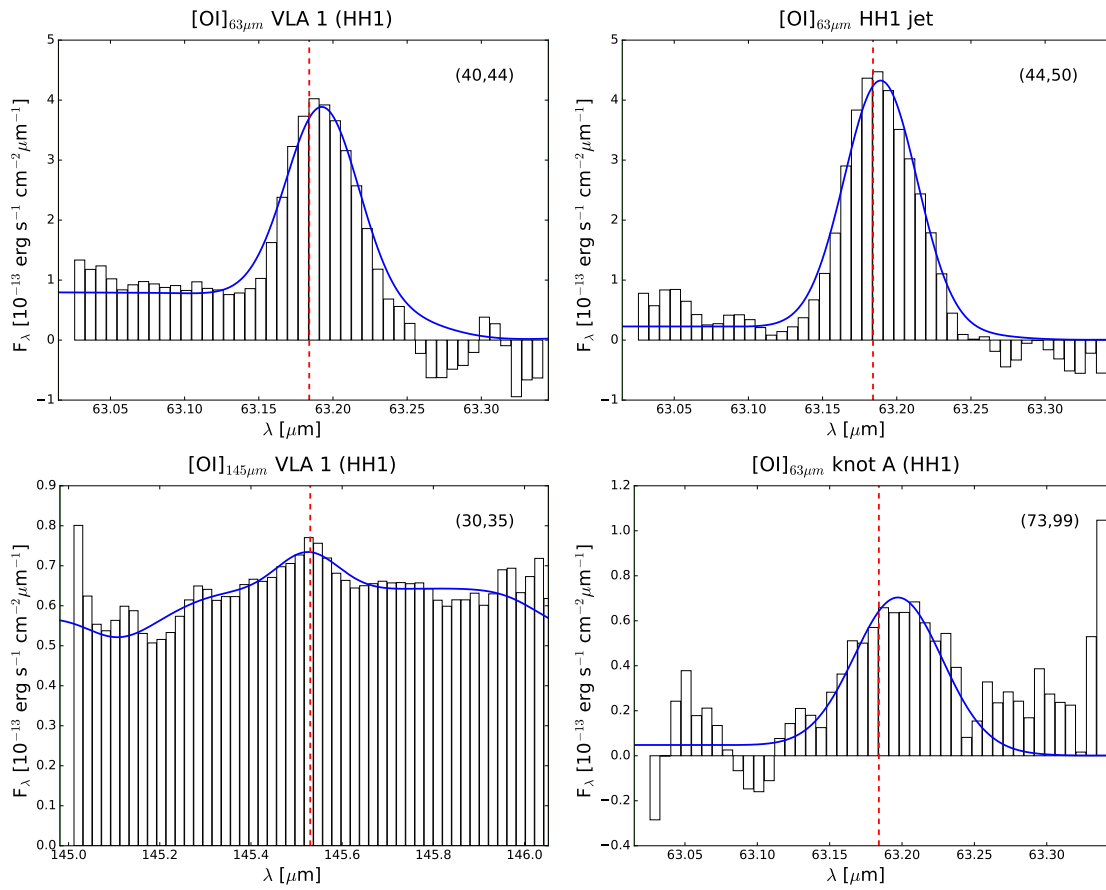
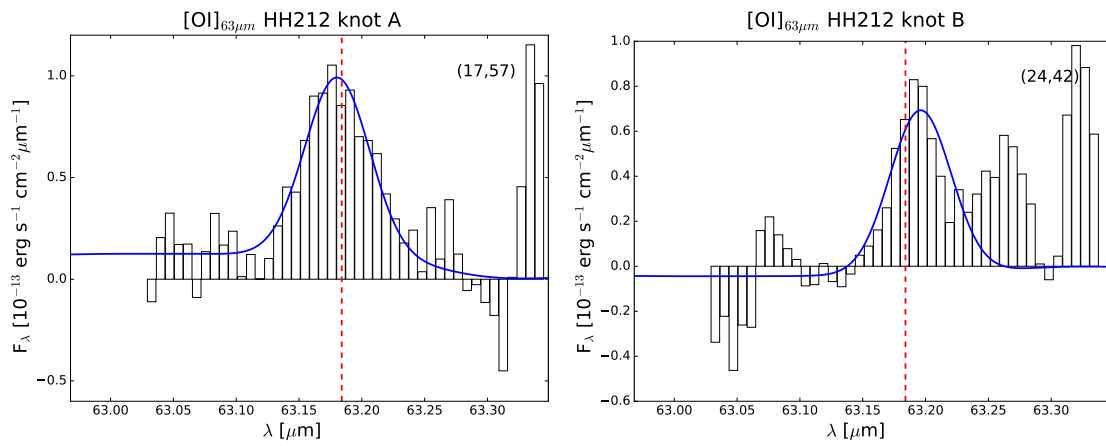
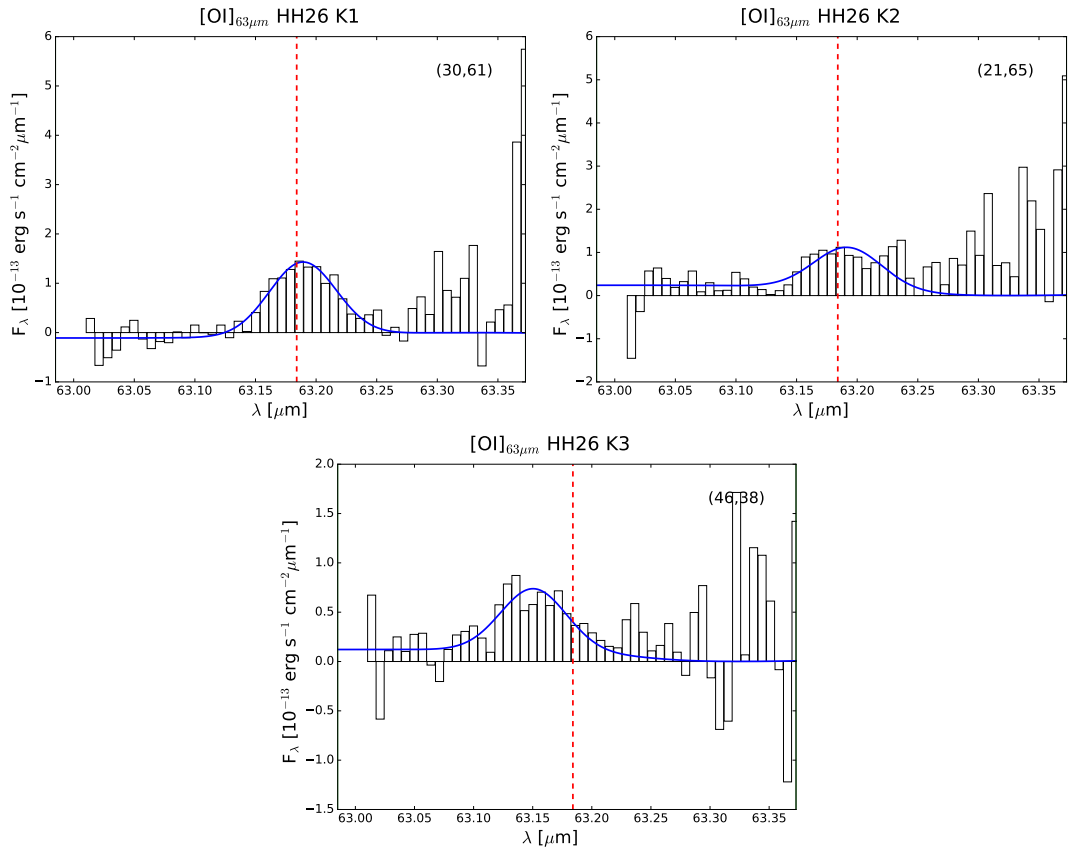
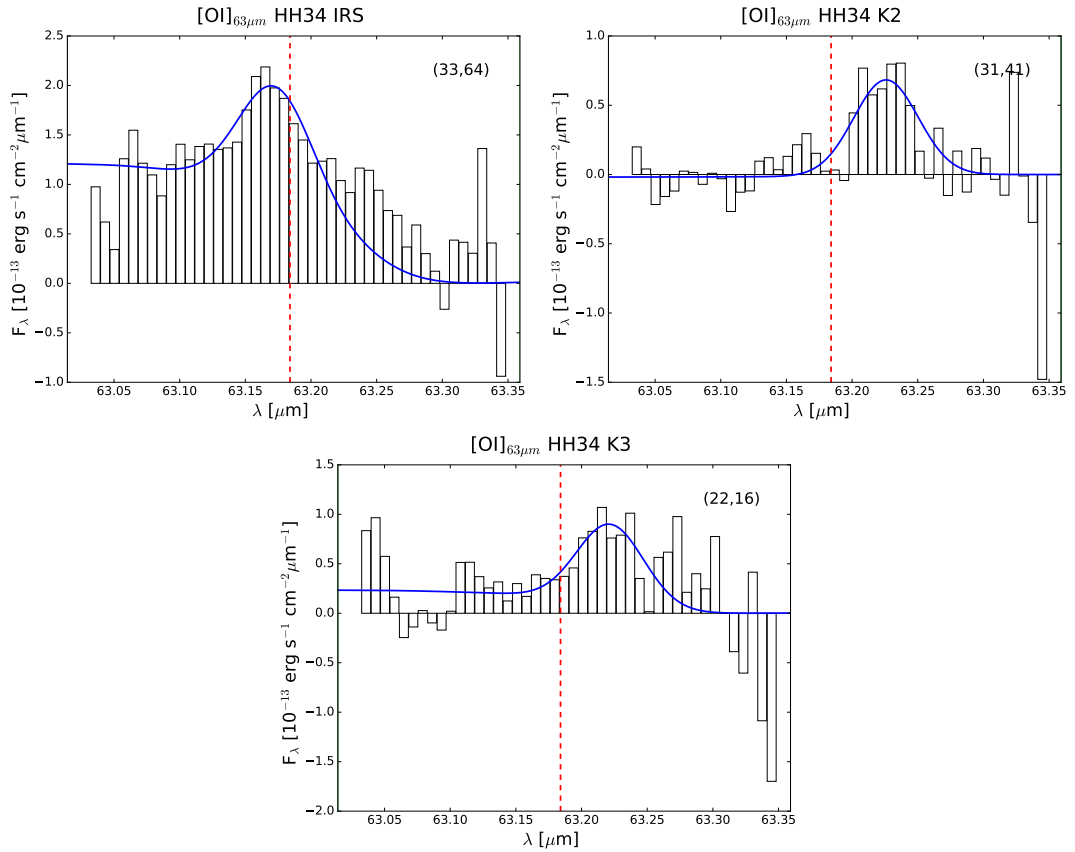


Fig. 5.9. Sample spaxels of Cep E.


Fig. 5.10. Sample spaxels of HH 1.

Fig. 5.11. Sample spaxels of HH 212.


Fig. 5.12. Sample spaxels of HH 26.

Fig. 5.13. Sample spaxels of HH 34.

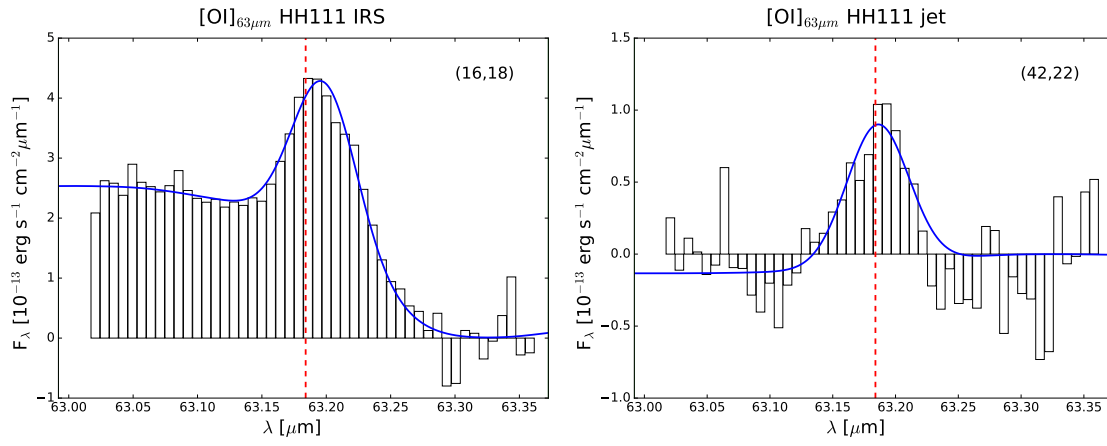


Fig. 5.14. Sample spaxels of HH 111.

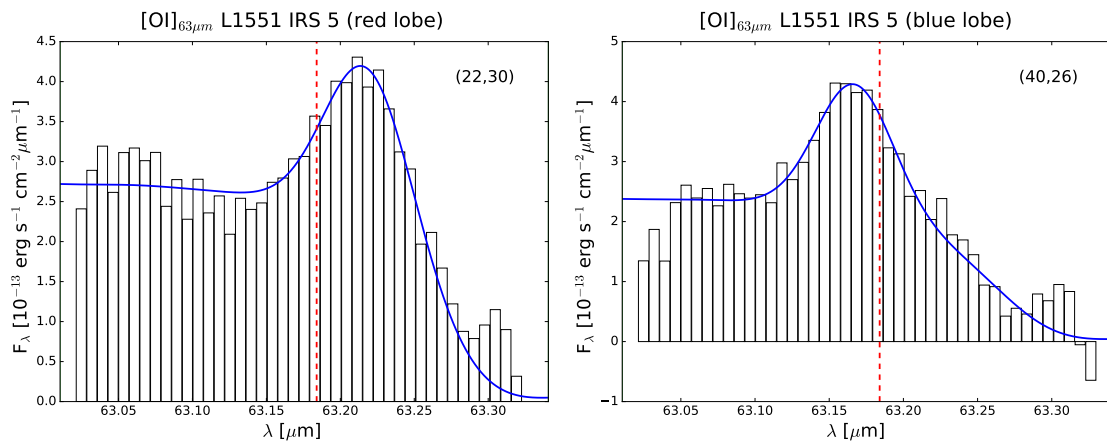
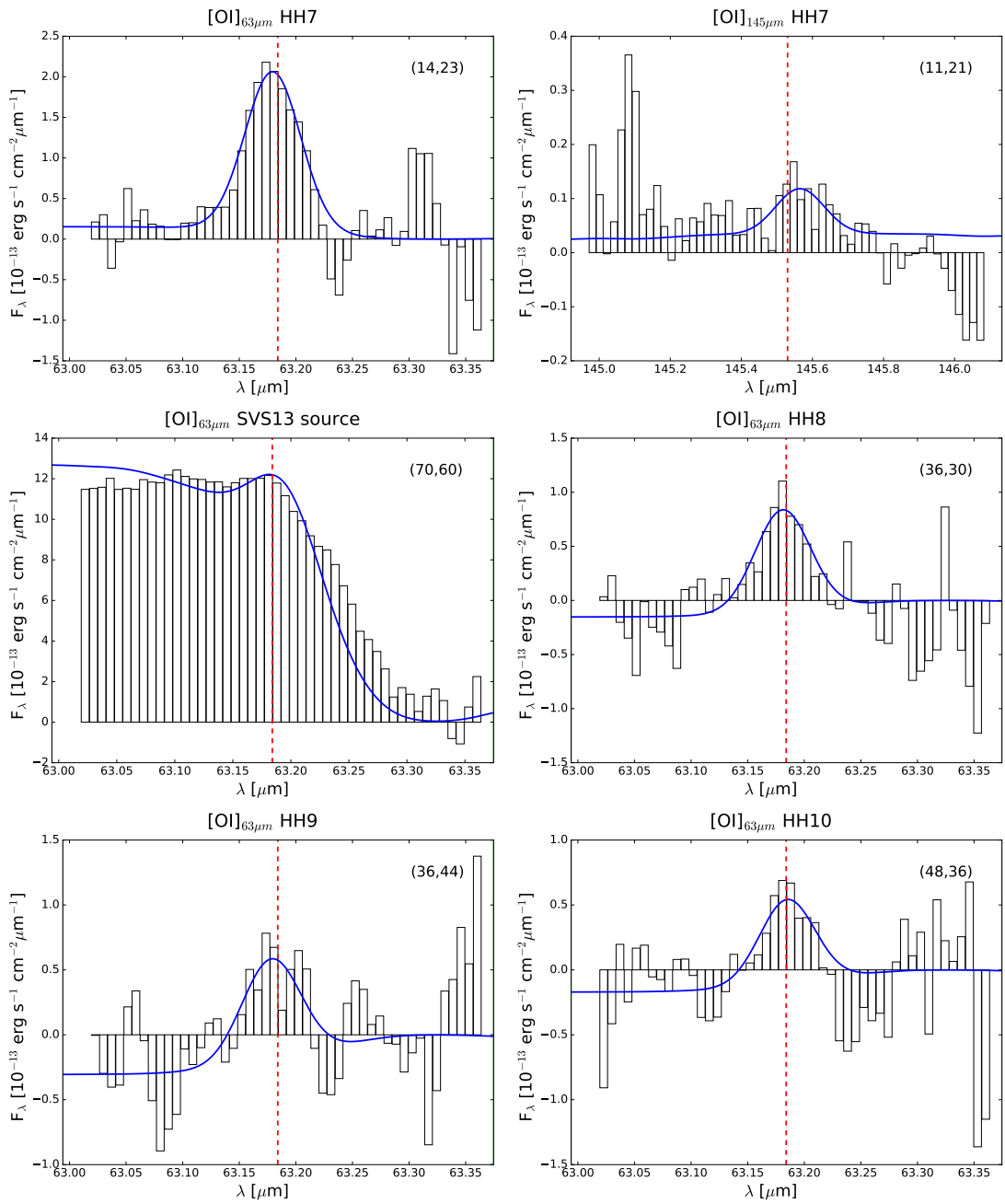
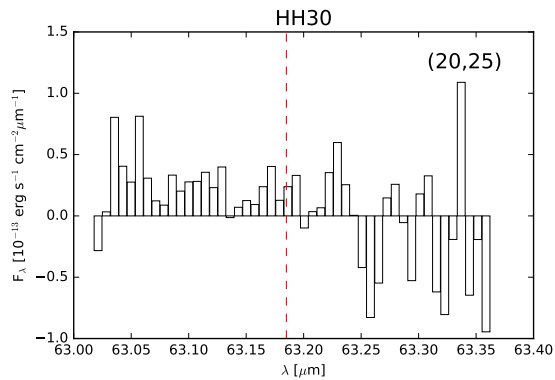


Fig. 5.15. Sample spaxels of L1551 IRS5.


Fig. 5.16. Sample spaxels of SVS 13.

Fig. 5.17. Sample spaxel of HH 30.

5.3 Flux and mass-loss rate measurements

We determined the flux within each aperture (yellow and green boxes in Figs. 5.1–5.8) by averaging all enclosed spaxels to a representative spaxel on which the model function (Eq. 4.1) is fitted. The parameter A (and its error) from this fit is then scaled with the box dimensions to get the reported flux values in Table 5.1.

Tab. 5.1. Flux measurements for the relevant aperture boxes, which are sketched in the continuum subtracted [O I]₆₃ maps. Fluxes are listed in units of 10^{-13} erg s⁻¹ cm⁻².

Target	Region	Size	$F_{63\mu\text{m}}$	$L([\text{O I}]_{63})/L_{\odot}^{\text{b}}$	$F_{145\mu\text{m}}$
Cep E	knot A	25'' × 23''	78.38 ± 3.69	13.06 ± 0.62 × 10 ⁻²	< 7.1 ^a
	jet	35'' × 23''	55.99 ± 3.43	9.33 ± 0.57 × 10 ⁻²	2.39 ± 0.82
HH 1	VLA 1	50'' × 25''	97.50 ± 2.59	5.63 ± 0.15 × 10 ⁻²	< 56.3 ^a
	knot A	20'' × 20''	10.74 ± 1.79	6.21 ± 1.04 × 10 ⁻³	< 3.0 ^a
HH 212	knot A and B	30'' × 15''	17.90 ± 3.47	9.87 ± 1.92 × 10 ⁻³	< 6.6 ^a
HH 26	HH 26A	28'' × 17''	29.18 ± 4.44	1.61 ± 0.24 × 10 ⁻²	< 3.7 ^a
HH 34	HH 34IRS	26'' × 22''	41.66 ± 5.87	2.41 ± 0.34 × 10 ⁻²	< 3.0 ^a
HH 111	HH 111IRS	20'' × 20''	44.76 ± 3.17	2.47 ± 0.18 × 10 ⁻²	< 10.1 ^a
	jet	50'' × 22''	23.49 ± 5.40	1.29 ± 0.30 × 10 ⁻²	< 8.4 ^a
L1551	IRS5	25'' × 18''	83.70 ± 4.52	5.13 ± 0.28 × 10 ⁻³	< 18.7 ^a
SVS 13	SVS 13A	22'' × 21''	84.38 ± 8.47	1.46 ± 0.15 × 10 ⁻²	< 3.7 ^a
	HH 8-11	40'' × 20''	41.08 ± 5.47	7.09 ± 0.94 × 10 ⁻³	< 5.1 ^a
	HH 7	21'' × 17''	39.69 ± 2.09	6.85 ± 0.36 × 10 ⁻³	< 3.4 ^a
HH 30	HH 30IRS	20'' × 20''	< 7.2 ^a	< 4.5 × 10 ⁻⁴	< 3.1 ^a

^a The listed value corresponds to the 3σ upper limit. ^b calculated via $L([\text{O I}]_{63}) = 4\pi D^2 F_{63\mu\text{m}}$.

We wish to derive reliable mass-loss rates from the stated [O I]₆₃ luminosities via both methods presented in Sec. 4.2. First of all we make use of the findings of the previous Section and discuss a potential PDR contamination and the applicability of the HM89 shock model. Finally, mass-loss rates estimated via both methods (Eq. 4.5 and 4.25) are listed in Tables 5.2 and 5.3.

PDR contamination

From the discussion in Section 5.1 we conclude that the observed [O I]₆₃ luminosities towards Cep E and HH 1 are contaminated by the presence of a PDR. In the case of Cep E Moro-Martín *et al.* (2001) estimate that about 20 % of the observed [O I]₆₃ emission (in both lobes) comes from the presence of a PDR region and 90–95 % of the residual [O I]₆₃ shock component is due to a J-shock. Towards HH 1

and its driving source VLA1, Giannini *et al.* (2001) and Molinari and Noriega-Crespo (2002) estimate that about 50 % may not originate from shocks but from the impact of a PDR. In conclusion, mass-loss rates for Cep E and HH 1 derived from both methods are upper limits at best.

Applicability of the HM89 shock model

The crucial assumption in the HM89 shock model is that all the observed [O I]₆₃ emission comes from one decelerated wind shock (J-type). Again, from the discussion in Section 5.1 we conclude that the HM89 shock conditions most probably prevail towards: HH 212, HH 34 IRS, HH 111 IRS, L1551 IRS5, SVS 13 (IRAS 03259+3105). The jet-like structures towards Cep E, HH 1, and HH 111 are caused by multiple internal shocks, that are spatially unresolved in our maps. The optically bright emission regions HH 7 and HH 1 are likely terminal bow-shocks, whereas HH 26A and HH 8-10 may be interpreted as a deflection zone.

5.4 Accretion rates

In order to evaluate the jet efficiency, that is the ratio between the mass-loss in the outflow and the mass accretion onto the source, we calculate instantaneous accretion rates for the observed targets from their bolometric luminosities and additional stellar parameters (Gullbring *et al.* 1998; Hartmann *et al.* 1998; White and Hillenbrand 2004).

In the underlying framework of magnetospheric accretion (Bouvier *et al.* 2007; Camenzind 1990; Hartmann *et al.* 2016) material flows along stellar magnetic field lines from the accretion disk onto the forming star causing potentially detectable emission lines to appear in the spectrum (Antoniucci *et al.* 2014a; Muzerolle *et al.* 1998; Rigliaco *et al.* 2012) or an excess of emitted UV flux (Gullbring *et al.* 1998; Herczeg and Hillenbrand 2008). Typically, in the case of Class 0/I sources fiducial values for their stellar parameters are inferred, since observationally based estimates using evolutionary tracks are considered unreliable (see discussion in Contreras Peña *et al.* 2017). The most direct measurements of L_{acc} may be obtained from UV-spectra, which would probably fail for any of the considered outflow sources, since they are highly embedded.

Following Mottram *et al.* (2017) we estimate accretion rates \dot{M}_{acc} uniformly via (R_{\star} stellar radius, M_{\star} stellar mass, L_{acc} accretion luminosity)

$$\dot{M}_{\text{acc}} = \frac{L_{\text{acc}} R_{\star}}{GM_{\star}}. \quad (5.1)$$

Depending on the evolutionary state of the outflow source we infer the fiducial values (see discussion in Mottram *et al.* 2017)

$$\text{Class 0: } M_{\star} = 0.2 M_{\odot}, R_{\star} = 4 R_{\odot}, L_{\text{acc}} = L_{\text{bol}}$$

$$\text{Class I: } M_{\star} = 0.5 M_{\odot}, R_{\star} = 4 R_{\odot}, L_{\text{acc}} = 0.5 L_{\text{bol}}.$$

Karska *et al.* (2018) and van Dishoeck *et al.* (2011) provide consistent measurements for L_{bol} for all the observed objects. Mass accretion rates for Cep E and SVS 13 are estimated separately in Appendix A. The calculated accretion rates are listed in Tables 5.2 and 5.3.

Tab. 5.2. Calculated mass-loss and accretion rates for the observed targets of this study. $\dot{M}_{\text{out}}^{\text{lum}}([\text{O I}])$ and $\dot{M}_{\text{out}}^{\text{shock}}([\text{O I}])$ are calculated via Eq. 4.25 and Eq. 4.5, respectively.

Target	Region	[O I] ₆₃ origin	θ ($''$)	v_t (km s^{-1})	$\dot{M}_{\text{out}}^{\text{lum}}([\text{O I}])$	$\dot{M}_{\text{out}}^{\text{shock}}([\text{O I}])$ ($10^{-7} M_{\odot} \text{ yr}^{-1}$)	$\dot{M}_{\text{out}}^{\text{other}}$ & component	\dot{M}_{acc}^e ($10^{-7} M_{\odot} \text{ yr}^{-1}$)
Cep E	knot A	PDR, partly dissociative J-shocks	25	95 ^a	$\lesssim 22.4 - 45.5$	$\lesssim 124.4 - 136.7$	$\sim 200^j$ & CO	170 ^f
	jet	PDR, few internal shocks (mostly non-dissociative)	35	60 ^a	$\lesssim 7.2 - 14.7$	$\lesssim 87.5 - 99.0$		
HH 1	VLA 1	PDR, dissociative J-shocks	50	300 ^b	$\lesssim 25.9 - 52.6$	$\lesssim 54.9 - 57.8$	$\sim 6^k$ & [Fe II]	290 ^g
	knot A	PDR, bow shocks	20	400 ^b	$\lesssim 9.5 - 19.4$	$\lesssim 5.2 - 7.2$	$\sim 4^k$ & [S II] $\sim 0.1^k$ & H ₂ $\sim 15^l$ & CO	
HH 212	knot A and B	dissociative J-shocks	30	150 ^c	3.9 – 7.9	8.0 – 11.8	$\sim 10^m$ & CO, SO, SiO $\leq 3^n$ & CO, SiO $\sim 1^o$ & H ₂	80 ^h
L1551	IRS 5	dissociative J-shocks, disk winds, disk winds, deflections	25	120 ^d	5.8 – 11.8	4.9 – 5.4	$\gtrsim 100^p$ & CO, HCO ⁺ (swept-up gas) $\sim 8.6^q$ & HI $\sim 1.7^r$ & [Fe II] $\sim 0.4^r$ & H ₂	30 ⁱ

^a proper motions from Noriega-Crespo *et al.* (2014); ^b proper motions from Bally *et al.* (2002b); ^c proper motions from Noriega-Crespo *et al.* (2020); ^d proper motions from Fridlund and Liseau (1994); ^e calculated from their bolometric luminosities; ^f our estimate (see Appendix A); ^g the stated value is in good agreement with Fischer *et al.* (2010), HOPS 203 therein; ^h the stated value is in good agreement with Lee *et al.* (2014a); ⁱ the stated value is in good agreement with e.g. Gramajo *et al.* (2007), Liseau *et al.* (2005), and Osorio *et al.* (2003); ^j Lefloch *et al.* (2015), this material is directly connected to the Cep E jet and not to swept-up gas; ^k Nisini *et al.* (2005); ^l from CO (J=1-0) observations undertaken by Tanabe *et al.* (2019), i.e. rather entrained material; ^m Lee (2020), Lee *et al.* (2007a, 2015), and Podio *et al.* (2015); ⁿ Cabrit *et al.* (2012); ^o Davis *et al.* (2000); ^p Fridlund *et al.* (2002), Hogerheijde *et al.* (1998), and Yıldız *et al.* (2015); ^q Giovanardi *et al.* (2000); ^r Davis *et al.* (2003).

Tab. 5.3. Estimated mass-loss and accretion rates for the observed targets of this study. $\dot{M}_{\text{out}}^{\text{lum}}([\text{O I}])$ and $\dot{M}_{\text{out}}^{\text{shock}}([\text{O I}])$ are calculated via Eq. 4.25 and Eq. 4.5, respectively.

Target	Region	[O I] ₆₃ origin	θ ($''$)	v_t (km s^{-1})	$\dot{M}_{\text{out}}^{\text{lum}}([\text{O I}])$	$\dot{M}_{\text{out}}^{\text{shock}}([\text{O I}])$ ($10^{-7} M_{\odot} \text{ yr}^{-1}$)	$\dot{M}_{\text{out}}^{\text{other}}$ & component	$\dot{M}_{\text{acc}}^{\text{p}}$ ($10^{-7} M_{\odot} \text{ yr}^{-1}$)
HH 26	HH 26A	deflection shocks	28	100 ^b	–	–	0.2 – 0.5 ^h & H ₂	~ 8.5 ^h
HH 34	HH 34IRS	wind shock, disk, jet shock	26	160 ^c	11 – 23	20.7 – 27.5	0.7 ^g & [Fe II] 0.03 ^g & H ₂ ~ 1.5 ^e & [O I] λ 6300	35 – 115 ^k
HH 111	HH 111IRS	quasi-spherical wind shock	20	270 ^a	26 – 53	22.9 – 26.4	4 ^d & CO	27 ⁱ
	jet (knots F-O)	few internal shocks	45	260 ^a	6 – 12	$\lesssim 10$ – 16	2 – 6 ^e & [O I] λ 6300	
SVS 13	SVS 13A	wind shock, jet shock	22	270 ^b	25 – 51	13.1 – 16.0	30 ^f & HI	140 – 170 ^j
	HH 8-11	deflection shocks	40	340 ^b	–	–	8.9 ^g & [Fe II]	
	HH 7	bow shock	21	400 ^b	–	–	7.0 ^g & H ₂	
HH 30	HH 30 IRS	no [O I] ₆₃ detection	20	200 ^m	< 0.2	–	~ 0.02 & optical lines (BE) 170 ⁿ & CO (entrained gas)	$\lesssim 0.04^{\circ}$

^a Hartigan *et al.* (2001); ^b Chrysostomou *et al.* (2000); ^c Eisloffel and Mundt (1992); ^d Lefloch *et al.* (2007), the high-velocity outflowing gas is detected therein in the CO $J = 7 - 6$ transition. We therefore think that the stated mass-loss rate is connected to the jet itself and not to swept-up gas; ^e Hartigan *et al.* (1994); ^f Lizano *et al.* (1988); ^g Davis *et al.* (2003); ^h Antonucci *et al.* (2008); ⁱ the stated accretion rate is in good agreement with Lee (2010), Yang *et al.* (1997) estimate a higher value of $6.9 \times 10^{-6} M_{\odot} \text{ yr}^{-1}$; ^j estimated from the Bry line (see Appendix A); ^k based on measurements of accretion-induced emission lines Antonucci *et al.* (2008) estimate an accretion rate of $\dot{M}_{\text{acc}} \sim 41.1 \times 10^{-7} M_{\odot} \text{ yr}^{-1}$, whereas Nisini *et al.* (2016) $\dot{M}_{\text{acc}} \sim 75 \pm 40 \times 10^{-7} M_{\odot} \text{ yr}^{-1}$. Hartigan *et al.* (1994) states $\dot{M}_{\text{acc}} \sim 110 \times 10^{-7} M_{\odot} \text{ yr}^{-1}$. We combine the mentioned values to a range of $(35 - 115) \times 10^{-7} M_{\odot} \text{ yr}^{-1}$; ^m Bacciotti *et al.* (1999); ⁿ Louvet *et al.* (2018); ^o Wood *et al.* (2002); ^p calculated from their bolometric luminosities, if not stated otherwise.

CHAPTER 6

The evolutionary role of the atomic outflow component

6.1 Efficiencies of fully mapped Class 0/I outflow sources

Apart from the newly observed targets in this study, only seven other protostellar outflows have been mapped in the far-infrared $[\text{O I}]_{63}$ emission line in a comparable way (see Table 6.1) with Herschel/PACS:

- Nisini *et al.* (2015) observed five Class 0/I sources and their outflows, namely L1448-C (Class 0), NGC 1333-IRS4 (Class 0), HH 46 (Class I), BHR 71 (Class 0), and VLA 1623 (Class 0).
- Dionatos *et al.* (2018) mapped the HH 211 protostellar system driven by HH 211-MM (Class 0) in $[\text{O I}]_{63}$ and various molecular transitions (CO, H₂O, and OH).
- Dionatos and Güdel (2017) mapped the IRAS 2A S-N outflow in the NGC 1333 star forming region in $[\text{O I}]_{63}$ and $[\text{C II}]_{158}$.

Tab. 6.1. Comparison of capabilities of the SOFIA/FIFI-LS and the Herschel/PACS instruments.

Property	SOFIA/FIFI-LS	Herschel/PACS
Beam size at 63 μm	$\sim 5.4''$	$\sim 5''$
Spatial sampling	$6'' \text{ spaxel}^{-1\text{a}}$	$9.4'' \text{ spaxel}^{-1}$
FOV ^b	$30'' \times 30''^{\text{a}}$	$47'' \times 47''$
#Spaxels in IFU ^c	$5 \times 5^{\text{a}}$	5×5
Spectral resolution at 63 μm	~ 1300	~ 3500

^a in blue channel; ^b total field of view; ^c number of spatial pixels in the corresponding integral field unit.

We include these outflows to our set of altogether 14 protostellar outflows, for which the jet efficiency can be evaluated. Given the uncertainty of the applicability of the HM89 shock model, we calculate the mass-loss rates for the seven additional outflows from their $[\text{O I}]_{63}$ jet luminosities (Eq. 4.25). This way, all mass-loss rates for the 14 outflow sources have been determined uniformly using the same method. In Table 6.2 the newly calculated mass-loss and accretion rates are listed.

Tab. 6.2. Mass-loss rates and accretion rates for outflow sources that have been mapped extensively with Herschel/PACS in [O I]₆₃.

Target	Class	D	θ ($''$)	v_t (km s^{-1})	$L([\text{O I}])$ (L_\odot)	$\dot{M}_{\text{out}}^{\text{lum}}([\text{O I}])$	$\dot{M}_{\text{out}}^{\text{shock}}([\text{O I}])$ ($10^{-7} M_\odot \text{ yr}^{-1}$)	$\dot{M}_{\text{out}}^{\text{other}} \& \text{ comp.}$	\dot{M}_{acc}^1 ($10^{-7} M_\odot \text{ yr}^{-1}$)	Ref.
L1448-C	0	232	45	170	1.8×10^{-3}	1 – 2	2 – 4	$\sim 24^a$ & SiO, SO, CO	35	Ni15
IRAS 4A	0	235	38	100 – 140	9.1×10^{-4}	0.3 – 1.0	1 – 2	$\geq 18^b$ & CO	58	Ni15
HH 46	I	450	59	300	2.0×10^{-2}	7 – 15	20 – 40	15 – 28 & CO	34 ^f	Ni15
BHR 71	0	200	33	50 – 100	3.2×10^{-3}	1 – 3	3 – 6	21 ^j & CO	73 ^g	Ni15
VLA 1623	0	120	78	60	2.1×10^{-3}	0.5 – 1	2 – 4	16 – 160 & CO	21	Ni15
HH 211 SE lobe	0	250	51	115	3.92×10^{-3}	1.2 – 2.4	3.9			
HH 211 NW lobe	0	250	45	115	3.57×10^{-3}	1.2 – 2.4	3.6			
HH 211 both lobes						2.4 – 4.8	7.5	7 – 28 ^c & SiO, CO, SO $\sim 20 - 28^d$ & H ₂	14 ^h	Di18
IRAS 2A, blue lobe SN	0	235	188	50	3.5×10^{-3}	0.1 – 0.3	3.5	200 ^k & CO		
IRAS 2A, red lobe SN	0	235	133	50	4.1×10^{-3}	0.2 – 0.4	4.1	400 ^k & CO		
IRAS 2A, both lobes SN						0.3 – 0.7	7.6	6 ^e & H ₂ $> 6.7^b$ & SiO, CO, SO	234 ⁱ	Di17

^a Lee (2020), Podio *et al.* (2020), and Yoshida *et al.* (2021); ^b Podio *et al.* (2020); ^c Lee (2020) and Lee *et al.* (2007b, 2010); ^d Dionatos *et al.* (2010); ^e Maret *et al.* (2009); ^f Antoniucci *et al.* (2008) estimate $2.2 \times 10^{-7} M_\odot \text{ yr}^{-1}$ based on a substantially lower bolometric luminosity; ^g Yang *et al.* (2017) estimate $1.2 \times 10^{-5} M_\odot \text{ yr}^{-1}$; ^h the stated accretion rate is about a factor of six lower than the value estimated by Lee *et al.* (2007c), who however assume a substantially lower mass for the HH 211 protostar $M_\star = 0.06 M_\odot$; ⁱ the stated value lies in-between the values estimated by Brinch *et al.* (2009) and Hsieh *et al.* (2019), that are $94 \times 10^{-7} M_\odot \text{ yr}^{-1}$ and $500 \times 10^{-7} M_\odot \text{ yr}^{-1}$ respectively; ^j Yang *et al.* (2017); ^k based of CO J=6-5 observations (Yildiz *et al.* 2015); ^l calculated from their bolometric luminosities; **References:** Ni15: Nisini *et al.* (2015); Di18: Dionatos *et al.* (2018); Di17: Dionatos and Güdel (2017).

Figure 6.1 shows the mass-loss rate $\dot{M}_{\text{out}}([\text{OI}])$ derived from the $[\text{OI}]_{63}$ jet luminosity as a function of the accretion rate \dot{M}_{acc} for the fully mapped outflows. Half of the sources feature efficiency ratios between $\dot{M}_{\text{out}}([\text{OI}])/\dot{M}_{\text{acc}} \sim 0.05\text{--}0.5$. This range for the outflow efficiency ratio is consistent with a) proposed jet launching models, that is the X-wind scenario (Shu *et al.* 1994; Shu *et al.* 1988) or magnetohydrodynamical disc wind models (Casse and Ferreira 2000; Ferreira 1997), and b) other observational studies such as Ellerbroek *et al.* (2013), Lee (2020), Mottram *et al.* (2017), Podio *et al.* (2020), and Yoshida *et al.* (2021). Similar efficiency ratios are also found in massive protostellar outflows (e.g. Beuther *et al.* 2002) and towards more evolved outflows from T-Tauri stars (Coffey *et al.* 2008). Since $\dot{M}_{\text{out}}([\text{OI}])/\dot{M}_{\text{acc}} \lesssim 1.0$ for all our observed targets except for HH 111 we conclude that they are accretion-dominated. Geometric means of the mass-accretion rates for Class 0 and Class I outflow sources are almost the same, that is $\sim 10^{-5} M_{\odot} \text{ yr}^{-1}$. The geometric mean of the mass-ejection rates for the fully mapped Class 0 and Class I outflows are $3 \times 10^{-7} M_{\odot} \text{ yr}^{-1}$ and $2 \times 10^{-6} M_{\odot} \text{ yr}^{-1}$, respectively.

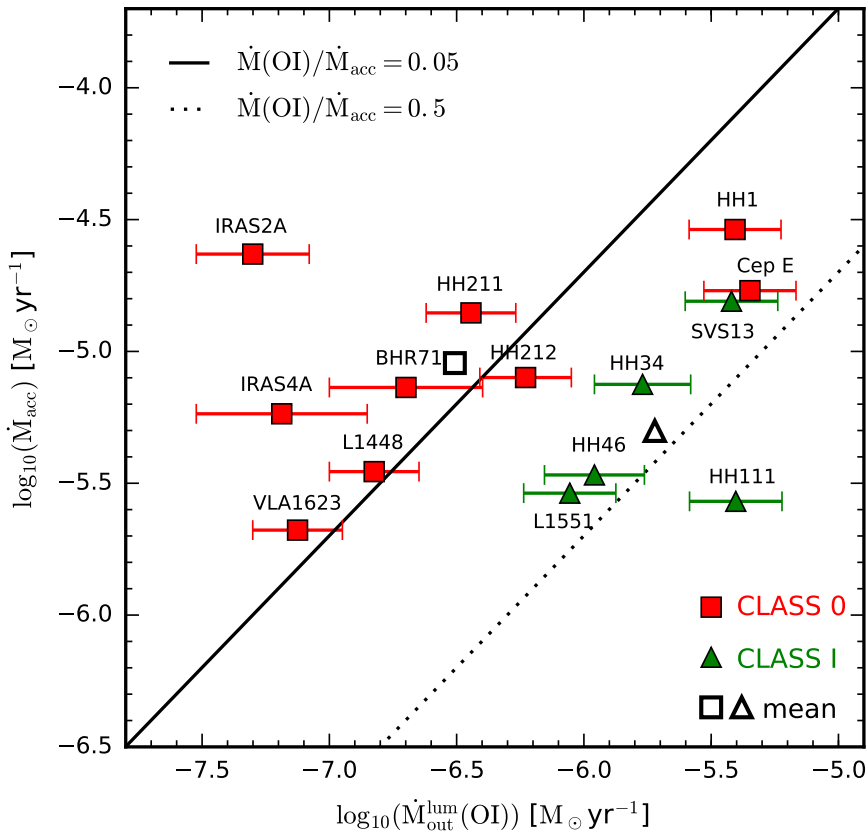


Fig. 6.1. The $\dot{M}_{\text{out}}^{\text{lum}}([\text{OI}])$ vs. \dot{M}_{acc} diagram for the extensively mapped outflow sources. The adopted mass-loss rate for Cep E is the sum of both contributions coming from knot A and the jet, that is $(29.6 - 60.2) \times 10^{-7} M_{\odot} \text{ yr}^{-1}$. In the case of HH 1 we considered the measurement at the HH 1 jet to be the best representation of the instantaneous mass-loss rate. Geometric means for Class 0/I outflows are plotted as non-filled black markers. Errorbars in accretion rates are not depicted, but can be on the order of one magnitude.

However, the noticed separation in Class 0 and Class I outflow sources in Fig. 6.1 might be an artefact from calculating the individual accretion-rates. In fact, accretion rates attributed to Class 0 sources in Eq. 5.1 are per se five times higher than accretion rates from Class I outflow sources with the same bolometric luminosity. A physical explanation for the trend in Fig. 6.1 could be that the mass-ejection rates in Class 0 sources are underestimated. So far only the atomic component traced by $[\text{OI}]_{63}$ is considered in Fig. 6.1. A comparative analysis of the other outflow components and their contributions to the total mass-loss rate is necessary here and will be covered in Section 6.2.

Given the low number of analysed outflow targets, a deep statistical cluster analysis of Fig. 6.1 would not be very meaningful and in addition to that our SOFIA sample may be biased since we selected the brightest and actively accreting known Class I outflow sources. However, it would be interesting to have similar observations of Class II outflows. So far, only very few Class II outflows have been observed spatially resolving the $[\text{OI}]_{63}$ emission along the outflow (Podio *et al.* 2012). Fortunately, jets from Class II sources are usually very compact ($\sim 10''$ – $20''$) potentially rendering extensive mapping redundant.

6.2 Other outflow components

In Tables 5.2, 5.3, and 6.2 we compare mass-loss rates derived from the $[\text{OI}]_{63}$ line with mass-loss rates estimated via other tracers.

In seven out of nine Class 0 outflows the bulk mass-loss resides in the molecular component. Only in two cases of Class 0 outflows the atomic component traced by $[\text{OI}]_{63}$ is either dominant (HH 1) or comparable (HH 212) to the molecular component.

Among the five Class I outflows four are predominantly atomic (HH 111, HH 34, SVS 13, L1551) and in the case of HH 46 both components contribute a comparable amount to the mass-loss. In this analysis, we ignored mass-losses that are likely associated with entrained material.

In fact, mass-loss rates that have been derived from CO emission may trace entrained material. In this regard we point out that Tables 5.2, 5.3, and 6.2 contain recent mass-loss rate measurements for the molecular component at high angular resolution (Lee 2020; Podio *et al.* 2020; Yang *et al.* 2017; Yoshida *et al.* 2021). In detail, the stated mass-loss rates for the CO, SiO, and SO outflow components of L1448-C, IRAS 4A, BHR 71, IRAS 2A, HH 211, HH 212, and Cep E can be considered as reliable estimates. In comparison, Yıldız *et al.* (2015) utilised CO observations (CO 3-2 and CO 6-5) at lower angular resolution to estimate mass-loss rates. Among both CO transitions the CO 3-2 emission line traces entrained material and mass-loss rates derived from it are usually by a factor of ~ 100 higher

than the values stated in Lee (2020), Podio *et al.* (2020), Yang *et al.* (2017), and Yoshida *et al.* (2021). Yıldız *et al.* (2015) have speculated that the CO 6-5 transition potentially traces not entrained material and may allow more reliable estimates of mass-loss rates. However, mass-loss rates derived from the CO 6-5 line are almost always on the same order of magnitude as mass-loss rate estimates based on the CO 3-2 transition. We therefore think, that mass-loss rates derived from CO 6-5 observations are still heavily affected by entrained gas.

In conclusion, there is evidence that the mass-loss rates of the considered Class 0 outflow sources in Fig. 6.1 are significantly underestimated, since the molecular component contributes predominantly to the mass-loss.

6.3 A comparison with outflows with unresolved mapping

In order to compare the results from the fully mapped outflows with other studies, we compile a list of Class 0/I/II outflow sources that have been observed with Herschel/PACS as part of the WISH+DIGIT+WILL+GASPS surveys, that is providing a single footprint with a $47'' \times 47''$ field of view in 5×5 spatial pixels of $9.4'' \times 9.4''$ each. For these outflow sources the $[\text{O I}]_{63}$ line is either spatially unresolved or not resolved enough (e.g. the sample of Podio *et al.* 2012) to infer relevant properties of the jet geometry. Under the given circumstances, mass-loss rates utilising the $[\text{O I}]_{63}$ line are derived from the HM89 shock model and not from the $[\text{O I}]_{63}$ jet luminosity. Watson *et al.* (2016) did a similar analysis in their survey of 84 YSOs using the Spitzer Infrared Spectrograph. Their mass-loss rate measurements are, however, not directly based on the HM89 shock model, since the $[\text{Si II}]_{35}$ and $[\text{Fe II}]_{26}$ lines are used as a proxy for the $[\text{O I}]_{63}$ line. This introduces new uncertainties as discussed therein. Therefore, we do not include their sources here.

From the Herschel/PACS surveys we selected 72 additional outflow sources (28 Class 0, 23 Class I, 21 Class II, see Tables 6.3–6.5) for which the $[\text{O I}]_{63}$ line is prominently detected, but mostly – unlike in our study – spatially unresolved. In detail, our selection comprises:

- Mottram *et al.* (2017) compiles a list of 91 protostellar sources that were observed as part of the WILL, WISH, and DIGIT surveys. From the 49 WILL sources we selected only the 26 (15 Class 0, 11 Class I) outflow sources, for which \dot{M}_{out} and \dot{M}_{acc} are specified in table A.7 therein. From the remaining 42 DIGIT+WISH sources we excluded the sources: a) for which \dot{M}_{out} is not given in table A.7; b) that have been analysed in much more detail in our spatially resolved sample; c) that could not be classified fairly unambiguously as Class 0 or Class I sources. That gives 25 (13 Class 0, 12 Class I) supplementary sources.
- To complete our sample with even more evolved outflow sources we included twenty-one Class II targets from the GASPS survey (Alonso-Martínez *et al.* 2017). In this study 26 outflow sources are listed from which we excluded four sources for which no accretion rates were specified or the classification was unsure. Amongst the selected 21 targets the Podio *et al.* (2012) sample is included with the exception of DG Tau B (TAU04 in Mottram *et al.* 2017). However, we took the newly determined $[\text{O I}]_{63}$ line fluxes specified in Alonso-Martínez *et al.* (2017) to recalculate the mass-loss rates via Eq. 4.5.

The [O I]₆₃ line fluxes have changed since the Herschel/PACS data were reduced using HIPEv10 in Alonso-Martínez *et al.* (2017), whereas Podio *et al.* (2012) used HIPE 4.0.1467. For discussion of this data reduction issue see e.g. Howard *et al.* (2013). The stated accretion rates for these more evolved sources are determined from the U band excess.

Tab. 6.3. Source sample from Alonso-Martínez *et al.* (2017) (GASPS survey), hereafter abbreviated AM17. Sources have been selected with the following selection criteria: a) Class II outflow sources (see Table 2 in Howard *et al.* 2013); b) \dot{M}_{acc} is given in Table A.1 therein; c) integrated [O I]₆₃ line fluxes over 3×3 spaxels are stated with error margins in Table C.3 therein.

Source	Class	$\dot{M}_{\text{out}}([\text{O I}])$ ($M_{\odot} \text{ yr}^{-1}$)	$\dot{M}_{\text{acc}}^{\text{f}}$ ($M_{\odot} \text{ yr}^{-1}$)	Main Ref.
AA Tau	II	$1.29 \pm 0.37 \times 10^{-9\text{a}}$	2.51×10^{-8}	AM17
CW Tau	II	$6.68 \pm 1.72 \times 10^{-9\text{a}}$	5.27×10^{-8}	AM17
DF Tau	II	$3.74 \pm 0.37 \times 10^{-9\text{c}}$	10.05×10^{-8}	AM17
DG Tau	II	$1.01 \pm 0.04 \times 10^{-7\text{a}}$	2.53×10^{-7}	AM17
DL Tau	II	$1.35 \pm 0.12 \times 10^{-9\text{c}}$	2.48×10^{-8}	AM17
DO Tau	II	$1.23 \pm 0.29 \times 10^{-8\text{a}}$	3.12×10^{-8}	AM17
DP Tau	II	$8.39 \pm 1.23 \times 10^{-9\text{a}}$	0.04×10^{-8}	AM17
DQ Tau	II	$1.29 \pm 0.25 \times 10^{-9\text{c}}$	0.59×10^{-8}	AM17
FS Tau	II	$3.27 \pm 0.12 \times 10^{-8\text{a}}$	$(2 - 3) \times 10^{-7\text{b}}$	AM17
GG Tau	II	$3.25 \pm 0.74 \times 10^{-9\text{a}}$	7.95×10^{-8}	AM17
Haro 6-13	II	$3.12 \pm 0.86 \times 10^{-9\text{a}}$	$2.88 \times 10^{-8\text{d}}$	AM17
HL Tau	II	$3.14 \pm 0.03 \times 10^{-8\text{c}}$	0.35×10^{-8}	AM17
HN Tau	II	$3.68 \pm 0.55 \times 10^{-9\text{a}}$	0.49×10^{-8}	AM17
IRAS04385+2550 ^e	II	$4.72 \pm 0.74 \times 10^{-9\text{a}}$	$7.76 \times 10^{-9\text{d}}$	AM17
RW Aur	II	$1.43 \pm 0.28 \times 10^{-8\text{a}}$	$(0.034 - 1.6) \times 10^{-6}$	AM17
SU Aur	II	$8.03 \pm 0.74 \times 10^{-9\text{a}}$	18.03×10^{-8}	AM17
T Tau	II	$1.12 \pm 0.02 \times 10^{-6\text{a}}$	2.36×10^{-7}	AM17
UY Aur	II	$2.24 \pm 0.09 \times 10^{-8\text{a}}$	6.74×10^{-8}	AM17
UZ Tau	II	$2.76 \pm 0.86 \times 10^{-9\text{c}}$	0.45×10^{-8}	AM17
V773 Tau	II	$5.57 \pm 0.74 \times 10^{-9\text{a}}$	11.95×10^{-8}	AM17
XZ Tau	II	$5.90 \pm 0.36 \times 10^{-8\text{a}}$	0.71×10^{-8}	AM17

^a Calculated via Eq. 4.5 from the given line [O I]₆₃ fluxes stated in Table C.3 in AM17;

^b Accretion rates from Podio *et al.* (2012); ^c Calculated via Eq. 4.5 from the given line [O I]₆₃ fluxes stated in Table 1 in Aresu *et al.* (2014); ^d White and Hillenbrand (2004);

^e other name Haro 6-33; ^f Accretion rates are calculated from the U band excess (see description in Alonso-Martínez *et al.* 2017).

Tab. 6.4. Source sample from the DIGIT, WILL, and WISH surveys. We took 25 sources (13 Class 0 and 12 Class I) from Table A.7 in Mottram *et al.* (2017), hereafter abbreviated Mo17, with the following selection criteria: a) \dot{M}_{acc} and \dot{M}_{out} are given in Table A.7; b) sources are not part of the spatially resolved Nisini *et al.* (2015) sample, which have been analysed in much more detail; c) flat sources are excluded (IRAS03301+3111, IRAS12496, RNO91) d) we exclude RCRA IRS5A, RCRA-I7A and RCRA-I7B since they are ambiguously classified.

Source	Class ^a	$\dot{M}_{\text{out}}([\text{O I}])$ ($M_{\odot} \text{ yr}^{-1}$)	$\dot{M}_{\text{out}}(\text{mol})$ ($M_{\odot} \text{ yr}^{-1}$)	$\frac{\dot{M}_{\text{out}}([\text{O I}])^{\text{f}}}{\dot{M}_{\text{out}}(\text{mol})}$	$\dot{M}_{\text{acc}}^{\text{d}}$ ($M_{\odot} \text{ yr}^{-1}$)	Main Ref.
IRAS03245+3002	0	6.4×10^{-8}			4.2×10^{-6}	Mo17
L1455-ISR3	I	5.0×10^{-8}			4.7×10^{-8}	Mo17
NGC 1333-IRAS 4B	0	1.3×10^{-8}	$\sim 3.8 \times 10^{-6\text{b}}$	3.4×10^{-3}	2.9×10^{-6}	Mo17
B1a	I	1.9×10^{-8}			3.5×10^{-7}	Mo17
L1489	I	2.2×10^{-8}	$\sim 6.1 \times 10^{-7\text{b}}$	3.6×10^{-2}	4.9×10^{-7}	Mo17
TMR1	I	1.1×10^{-7}	$\sim 4.1 \times 10^{-7\text{b}}$	2.6×10^{-1}	4.9×10^{-7}	Mo17
TMC1A	I	3.3×10^{-7}	$\sim 7.3 \times 10^{-7\text{b}}$	4.5×10^{-1}	3.5×10^{-7}	Mo17
L1527	0	1.8×10^{-7}	$\sim 4.5 \times 10^{-6\text{b}}$	4.0×10^{-2}	1.2×10^{-6}	Mo17
TMC1	I	1.5×10^{-7}	$\sim 1.6 \times 10^{-6\text{b}}$	9.4×10^{-2}	1.2×10^{-7}	Mo17
IRAM04191+1522	0	2.4×10^{-8}			7.1×10^{-8}	Mo17
Ced110-IRS4	0	1.3×10^{-7}	$\sim 3.3 \times 10^{-7\text{b}}$	3.4×10^{-1}	5.2×10^{-7}	Mo17
IRAS15398-3359	0	3.0×10^{-7}	$\sim 3.2 \times 10^{-6\text{b}}$	9.4×10^{-2}	1.0×10^{-6}	Mo17
GSS30 IRS1	I	5.1×10^{-7}	$\sim 1.3 \times 10^{-5\text{b}}$	3.9×10^{-3}	1.8×10^{-6}	Mo17
WL12	I	7.9×10^{-8}			2.1×10^{-7}	Mo17
Elias29	I	4.0×10^{-7}	$\sim 1.6 \times 10^{-6\text{b}}$	2.5×10^{-1}	1.8×10^{-6}	Mo17
IRS44	I	4.8×10^{-8}			6.6×10^{-7}	Mo17
IRS46	I	1.5×10^{-8}			6.5×10^{-8}	Mo17
IRS63	I	3.3×10^{-8}	$\sim 1.3 \times 10^{-5\text{c}}$		1.3×10^{-7}	Mo17
L483 MM	0	1.1×10^{-7}	$\sim 1.1 \times 10^{-5\text{b}}$	1.0×10^{-2}	6.6×10^{-6}	Mo17
Ser-SMM1	0	4.0×10^{-7}	$\sim 2.2 \times 10^{-5\text{b}}$	1.8×10^{-2}	7.1×10^{-5}	Mo17
Ser-SMM4	0	1.8×10^{-6}	$\sim 2.6 \times 10^{-5\text{b}}$	6.9×10^{-2}	4.4×10^{-6}	Mo17
Ser-SMM3	0	1.1×10^{-6}	$\sim 3.9 \times 10^{-5\text{b}}$	2.8×10^{-2}	1.2×10^{-5}	Mo17
L723 MM	0	1.3×10^{-8}	$\sim 1.5 \times 10^{-5\text{b}}$	8.7×10^{-4}	2.3×10^{-6}	Mo17
B335	0	2.5×10^{-8}	$\sim 2.9 \times 10^{-6\text{b}}$	8.6×10^{-3}	2.1×10^{-6}	Mo17
L1157	0	3.3×10^{-8}	$\sim 1.2 \times 10^{-4\text{e}}$		3.0×10^{-6}	Mo17

^a Classification from Green *et al.* (2013), Karska *et al.* (2013), Nisini *et al.* (2002), and Yang *et al.* (2018); ^b Yıldız *et al.* (2015) from CO 6–5 observations; the listed values are the sum of the mass-loss rates of both lobes. As stated therein, CO 6–5 potentially traces shocked gas in the outflow rather than entrained material; ^c Tanabe *et al.* (2019) from CO 1–0 observations, i.e. rather entrained material; ^d From Mottram *et al.* (2017) we adopt their method calculating the mass-accretion rates; ^e Yıldız *et al.* (2015) from CO 3–2 observations; the listed values are the sum of the mass-loss rates of both lobes. As stated therein, CO 3–2 potentially traces entrained material; ^f Ratio of column 7 and 8, not calculated in cases where the swept-up material is traced by CO.

Tab. 6.5. Source sample from the WILL survey (Mottram *et al.* 2017). We took only the 26 (15 Class 0 and 11 Class I) outflow sources, for which \dot{M}_{acc} is presented in Table A.7 therein.

Source ^a	Class	$\dot{M}_{\text{out}}([\text{OI}])$ ($M_{\odot} \text{ yr}^{-1}$)	$\dot{M}_{\text{out}}(\text{mol})^{\text{b}}$ ($M_{\odot} \text{ yr}^{-1}$)	$\dot{M}_{\text{acc}}^{\text{c}}$ ($M_{\odot} \text{ yr}^{-1}$)	Main Ref.
AQU 01	0	8.3×10^{-8}	8.5×10^{-5}	1.7×10^{-6}	Mo17
AQU 02	0	8.2×10^{-8}	1.3×10^{-5}	5.9×10^{-6}	Mo17
CRA 01	0	1.2×10^{-7}	2.3×10^{-6}	1.6×10^{-6}	Mo17
OPH 02	I	5.2×10^{-8}	2.5×10^{-8}	1.1×10^{-6}	Mo17
PER 01	0	3.4×10^{-7}	8.1×10^{-5}	2.9×10^{-6}	Mo17
PER 02	0	7.8×10^{-7}	–	6.0×10^{-6}	Mo17
PER 04	0	5.3×10^{-8}	7.1×10^{-7}	7.6×10^{-7}	Mo17
PER 05	I	2.8×10^{-8}	1.2×10^{-7}	1.4×10^{-6}	Mo17
PER 06	I	1.6×10^{-7}	–	9.2×10^{-7}	Mo17
PER 07	0	1.2×10^{-7}	3.8×10^{-6}	4.6×10^{-7}	Mo17
PER 08	I	1.1×10^{-6}	1.4×10^{-5}	2.2×10^{-6}	Mo17
PER 14	I	4.6×10^{-8}	3.7×10^{-6}	2.4×10^{-7}	Mo17
PER 15	0	2.1×10^{-8}	2.4×10^{-6}	1.1×10^{-6}	Mo17
PER 16	0	2.6×10^{-8}	7.6×10^{-6}	7.4×10^{-7}	Mo17
PER 17	I	1.4×10^{-8}	1.5×10^{-5}	2.3×10^{-8}	Mo17
PER 18	0	1.8×10^{-7}	3.4×10^{-6}	3.4×10^{-7}	Mo17
PER 19	I	1.8×10^{-7}	1.7×10^{-6}	1.4×10^{-7}	Mo17
PER 21	0	8.6×10^{-8}	7.8×10^{-6}	1.2×10^{-6}	Mo17
PER 22	0	1.0×10^{-7}	1.5×10^{-6}	1.6×10^{-6}	Mo17
SERS 01	0	2.8×10^{-7}	1.8×10^{-5}	1.1×10^{-5}	Mo17
TAU 01	I	7.6×10^{-8}	1.7×10^{-6}	2.0×10^{-7}	Mo17
TAU 02	I	1.1×10^{-8}	2.1×10^{-7}	6.1×10^{-8}	Mo17
TAU 04	I	4.5×10^{-8}	7.1×10^{-7}	1.8×10^{-7}	Mo17
TAU 06	I	9.6×10^{-9}	1.8×10^{-7}	7.3×10^{-8}	Mo17
W40 02	0	5.4×10^{-6}	1.0×10^{-5}	2.1×10^{-5}	Mo17
W40 07	0	5.4×10^{-8}	6.5×10^{-6}	2.3×10^{-6}	Mo17

^a Source names adopted from Mottram *et al.* (2017); ^b Calculated via the same method presented in Yıldız *et al.* (2015), however based on low-J CO observations, that is CO 3-2 measuring the entrained material; ^c From Mottram *et al.* (2017) we adopt their method calculating the mass-accretion rates.

Figure 6.2 shows $\dot{M}_{\text{out}}^{\text{shock}}(\text{[OI]})$ versus \dot{M}_{acc} for the selected 72 sources. For a better comparison we mark the coverage of the same plot for the fully mapped outflow sources (Fig. 6.1) with a grey rectangle. Mass-loss rates $\dot{M}_{\text{out}}^{\text{shock}}(\text{[OI]})$ in Figure 6.2 have been determined via the HM89 shock model, that is they potentially suffer from large uncertainties.

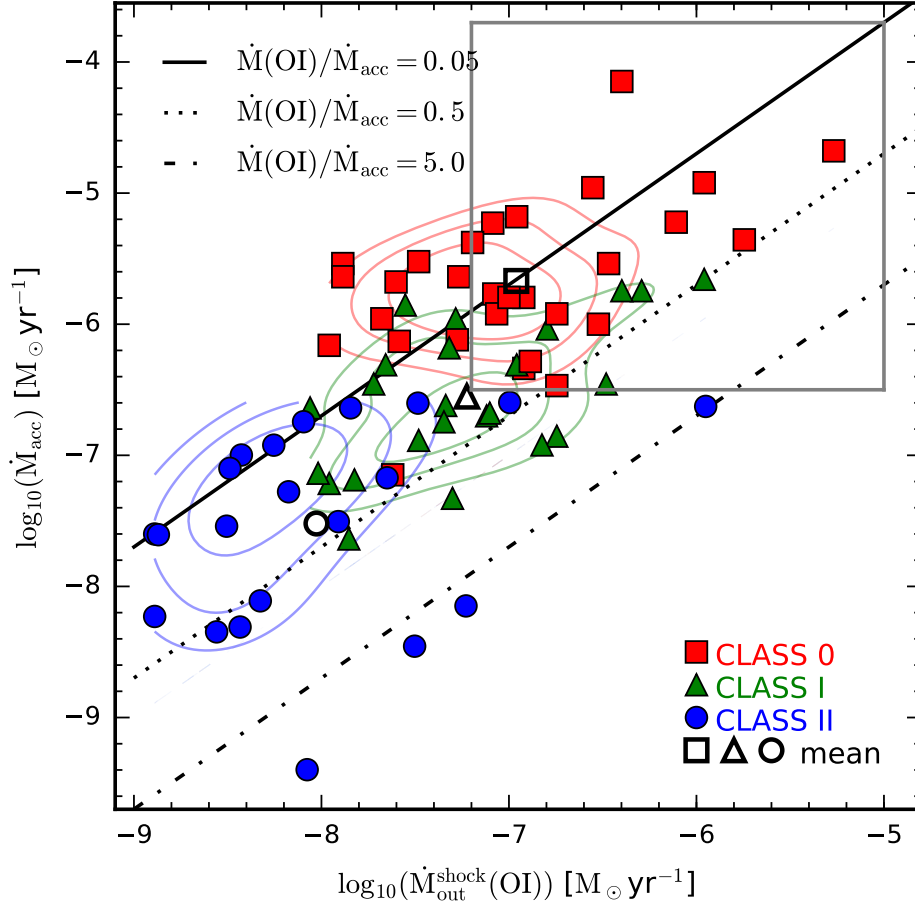


Fig. 6.2. Mass-loss rates $\dot{M}_{\text{out}}^{\text{shock}}(\text{[OI]})$ versus accretion rates \dot{M}_{acc} of protostellar outflow sources at different evolutionary stage observed with a single Herschel/PACS footprint. Mass-outflow rates have been determined assuming that the HM89 shock model conditions prevail. Geometric means for Class 0/I/II outflows are plotted as non-filled black markers. Thin coloured lines are contour lines based on a kernel-density estimate using Gaussian kernels. The grey box in the upper right corner indicates the extend of the similar diagram for the fully mapped outflows (Fig. 6.1).

From Fig. 6.2 four principal tendencies can be recognised:

1. Most sources are roughly located within the efficiency stripe of $f \sim 0.05\text{--}0.5$, which is in line with our previous findings. However, four Class I sources feature $f \gtrsim 1.0$ and four Class II sources show even higher efficiencies $f \gtrsim 5.0$ indicating that they are rather outflow dominated. In these sources a contribution from PDRs or disks could be more relevant.
2. Many Class 0 outflows show conspicuously low efficiency ratios $f < 0.05$.

The same trend is seen in the outflow sample of Fig. 6.1. For these targets, the total mass-loss rate from the $[\text{O I}]_{63}$ emission line could have been underestimated due to a significant molecular contribution. In this context, Yıldız *et al.* (2015) and Mottram *et al.* (2017) utilised CO observations to measured mass-loss rates residing in the molecular outflow component (values are listed in Tables 6.3 and 6.4). In particular, the mass-loss rates traced by CO J=6-5 in Yıldız *et al.* (2015) are insightful, since this gas may not be entrained material but part of the actual outflow. However, the analysis in Sec. 6.2 indicates that mass-loss rates based on CO J=6-5 observations are still substantially affected by entrained material. In this regard, observations at higher angular resolution as undertaken by Lee (2020), Podio *et al.* (2020), Yang *et al.* (2017), and Yoshida *et al.* (2021) may provide more robust mass-loss rate estimates. A comparison of both outflow components (atomic and molecular) is presented in Table 6.3. The notion that in Class 0 outflow sources the molecular component is dominant as compared to the atomic is well supported by these data. However, the comparison also shows, that limitedly mapped Class I outflow sources not necessarily show a dominant atomic outflow component. Extensive mapping in $[\text{O I}]_{63}$ might be necessary to draw meaningful conclusions.

3. Sources from the same Class are grouping in overlapping clusters as indicated by coloured contour lines in Fig. 6.2 representing a kernel-density estimate. In agreement with the findings of Ellerbroek *et al.* (2013) and Watson *et al.* (2016), there is a trend for which both mass-accretion and mass-loss rates evolve from higher to lower values passing from Class 0 to Class II. A similar conclusion cannot be drawn from the fully mapped outflows alone, since the sample is too small and biased towards brightest outflow sources.
4. There is a broad scatter in the \dot{M}_{out} vs. \dot{M}_{acc} diagram. Various reasons play a role here: a) Accretion rates of the younger sources might have been underestimated due to higher obscuration (Bacciotti *et al.* 2011); b) Time variability (Watson *et al.* 2016); c) The $[\text{O I}]$ emission line is exclusively used as a proxy to estimate the total instantaneous mass-loss rate. However, several other outflow components might contribute with an unknown amount to the total mass-loss rate or the underlying assumed shock conditions might not entirely prevail (Sperling *et al.* 2020).

Fig. 6.2 is not the first plot that shows \dot{M}_{out} vs. \dot{M}_{acc} for YSOs. The most recent studies of Ellerbroek *et al.* (2013) and Watson *et al.* (2016) include a similar diagram. Compared to these two studies the really new thing about Fig. 6.2 is that

- it includes only outflow sources – Watson *et al.* (2016) took into account

compact sources (the association with outflows was not a selection criterion), whereas the sample of Ellerbroek *et al.* (2013) comprises many different classes of objects (FU Ori objects, HAeBe stars, brown dwarfs, and continuum stars), but only a handful of Class 0/I sources

- it lays the focus on three earliest evolutionary Classes (Class 0/I/II outflow sources) – Ellerbroek *et al.* (2013) combine Class 0 and Class I sources to a single category
- mass-loss rates are determined uniformly from the $[\text{O I}]_{63}$ emission line – Watson *et al.* (2016) used two other emission lines ($[\text{Si II}]_{35}$ and $[\text{Fe II}]_{26}$) as a proxy for the $[\text{O I}]_{63}$ line and combined them to evaluate mass-loss rates; mass-loss rates in Ellerbroek *et al.* (2013) are partly taken from other papers and are based on different methods
- the age of the driving source has an influence on the accretion rate (see Sec. 5.4) – Watson *et al.* (2016) and Ellerbroek *et al.* (2013) calculate mass accretion rates regardless of age. It is, however, reasonable to assume that older sources have already accreted more material from their envelope, that is the relation of \dot{M}_{acc} and L_{bol} is different for different Classes.

Nevertheless, Fig. 6.2 exhibits defects when compared to Fig. 6.1. In Fig. 6.2 the mass-loss rates are purely based on the HM89 shock model. However, the applicability of the HM89 shock model has not been evaluated for any of the included sources. It is possible, that for many sources in Fig. 6.2 the derived mass-loss rates are of only limited informative value, if the HM89 shock conditions do not prevail. In this regard Fig. 6.1 is more meaningful since the $[\text{O I}]_{63}$ jet luminosity and the individual geometric properties of the outflows are taken into account. Such a detailed analysis became possible with our new SOFIA observations that spatially resolve the $[\text{O I}]_{63}$ emission line. However, the comparison with other outflow contributions demonstrated clearly that $[\text{O I}]_{63}$ maps alone are not enough to evaluate the evolution of protostellar outflows.

CHAPTER 7

Conclusions

There is a growing number of observational studies showing that the low-excitation, atomic outflow component traced by $[\text{OI}]_{63}$ plays a crucial role in the overall outflow evolution (e.g. Alonso-Martínez *et al.* 2017; Nisini *et al.* 2015; Watson *et al.* 2016). In fact, as protostellar outflow sources evolve from Class 0 to Class II their accretion rates and mass-loss rates tend to decrease (Watson *et al.* 2016) while the decisive ratio $\dot{M}_{\text{out}}/\dot{M}_{\text{acc}}$ may even remain constant (Podio *et al.* 2012). In this context, it is sometimes speculated, that the mass-loss rate determined via the $[\text{OI}]_{63}$ emission line may bona fide represent the bulk ejected material reflecting the anticipated outflow evolution (Dionatos and Güdel 2017). However, our observations and the comparison with other surveys suggest, as already pointed out by Nisini *et al.* (2015), that this hypothesis is barely true in outflows from Class 0 sources, where the bulk ejected material resides mainly in the molecular component. Thus, for these outflows mass-loss rates determined via $[\text{OI}]_{63}$ can be significantly underestimated. Qualitatively, these jets are largely not fast enough and too dense to be dissociative, and therefore they show very low excitation. As the source evolves towards the Class II stage, temperatures increase, densities decrease, winds become faster, and dissociative shocks connected to internal or wind shocks cause prominent atomic and ionic emission features depending on the specific excitation conditions in the flow material. These more evolved outflows become prominently detectable in e.g. $[\text{Fe II}]$, $[\text{S II}]$, $[\text{Si II}]$, and $[\text{OI}]$ tracing actually the same gas component at low excitation. As a result, the low-excitation outflow component associated with Class I/II sources and traced by $[\text{OI}]_{63}$ potentially represents the dominant contribution to the total mass-loss, but not necessarily. It would be interesting to see a \dot{M}_{out} vs. \dot{M}_{acc} diagram that considers all relevant outflow components to get a clear picture on the importance of the mass-loss traced by $[\text{OI}]_{63}$.

It becomes clear that the importance of $[\text{OI}]$ emission as a tracer of mass-loss is changing over time during the formation of the protostar, and that the far-infrared $[\text{OI}]_{63}$ emission alone cannot be used as a sole tracer to study the evolution of $\dot{M}_{\text{out}}/\dot{M}_{\text{acc}}$ during the whole star formation process.

Bibliography

- Abrahamsson, E. *et al.* (2007). “Fine-Structure Excitation of O I and C I by Impact with Atomic Hydrogen”. In: *ApJ* 654.2, pp. 1171–1174. doi: 10.1086/509631.
- Adams, Fred C. *et al.* (1987). “Spectral Evolution of Young Stellar Objects”. In: *ApJ* 312, p. 788. doi: 10.1086/164924.
- Alcalá, J. M. *et al.* (2017). “X-shooter spectroscopy of young stellar objects in Lupus. Accretion properties of class II and transitional objects”. In: *A&A* 600, A20, A20. doi: 10.1051/0004-6361/201629929. arXiv: 1612.07054 [astro-ph.SR].
- Alonso-Martínez, M. *et al.* (2017). “Herschel GASPS spectral observations of T Tauri stars in Taurus. Unraveling far-infrared line emission from jets and discs”. In: *A&A* 603, A138, A138. doi: 10.1051/0004-6361/201629005. arXiv: 1704.04834 [astro-ph.SR].
- Anderson, Dana E. *et al.* (2013). “New Constraints on the Sulfur Reservoir in the Dense Interstellar Medium Provided by Spitzer Observations of S I in Shocked Gas”. In: *ApJ* 779.2, 141, p. 141. doi: 10.1088/0004-637X/779/2/141.
- Andre, P. *et al.* (2000). “From Prestellar Cores to Protostars: the Initial Conditions of Star Formation”. In: *Protostars and Planets IV*. Ed. by V. Mannings *et al.*, p. 59. arXiv: astro-ph/9903284 [astro-ph].
- Andre, Philippe *et al.* (1993). “Submillimeter Continuum Observations of rho Ophiuchi A: The Candidate Protostar VLA 1623 and Prestellar Clumps”. In: *ApJ* 406, p. 122. doi: 10.1086/172425.
- Antoniucci, S. *et al.* (2008). “Accretion and ejection properties of embedded protostars: the case of HH26, HH34, and HH46 IRS”. In: *A&A* 479.2, pp. 503–514. doi: 10.1051/0004-6361:20077468. arXiv: 0710.5609 [astro-ph].
- Antoniucci, S. *et al.* (2014a). “POISSON project. III. Investigating the evolution of the mass accretion rate”. In: *A&A* 572, A62, A62. doi: 10.1051/0004-6361/201423929. arXiv: 1410.0181 [astro-ph.SR].
- Antoniucci, S. *et al.* (2014b). “The HH34 outflow as seen in [Fe ii] 1.64 μm by LBT-LUCI”. In: *A&A* 566, A129, A129. doi: 10.1051/0004-6361/201423944. arXiv: 1406.0761 [astro-ph.SR].
- Aresu, G. *et al.* (2014). “[O I] disk emission in the Taurus star-forming region”. In: *A&A* 566, A14, A14. doi: 10.1051/0004-6361/201322455. arXiv: 1402.2488 [astro-ph.SR].
- Armitage, Philip J. (2015). “Physical processes in protoplanetary disks”. In: *arXiv e-prints*, arXiv:1509.06382, arXiv:1509.06382. arXiv: 1509.06382 [astro-ph.SR].

- Asplund, Martin *et al.* (2009). “The Chemical Composition of the Sun”. In: *ARA&A* 47.1, pp. 481–522. doi: 10.1146/annurev.astro.46.060407.145222. arXiv: 0909.0948 [astro-ph.SR].
- Ayala, S. *et al.* (2000). “Optical and Near-Infrared Study of the Cepheus E Outflow, A Very Low-Excitation Object”. In: *AJ* 120.2, pp. 909–919. doi: 10.1086/301500. arXiv: astro-ph/0004298 [astro-ph].
- Bacciotti, F. and J. Eislöffel (1999). “Ionization and density along the beams of Herbig-Haro jets”. In: *A&A* 342, pp. 717–735.
- Bacciotti, F. *et al.* (2011). “The First X-shooter Observations of Jets from Young Stars”. In: *ApJ* 737.2, L26, p. L26. doi: 10.1088/2041-8205/737/2/L26. arXiv: 1106.3860 [astro-ph.SR].
- Bacciotti, Francesca *et al.* (1999). “The physical properties of the HH 30 jet from HST and ground-based data”. In: *A&A* 350, pp. 917–927.
- Bacciotti, Francesca *et al.* (2002). “Hubble Space Telescope/STIS Spectroscopy of the Optical Outflow from DG Tauri: Indications for Rotation in the Initial Jet Channel”. In: *ApJ* 576.1, pp. 222–231. doi: 10.1086/341725. arXiv: astro-ph/0206175 [astro-ph].
- Bachiller, R. *et al.* (2000). “The origin of the HH 7-11 outflow”. In: *A&A* 362, pp. L33–L36. eprint: astro-ph/0009439.
- Bally, J. *et al.* (1996). “A Burst of Herbig-Haro Flows in NGC 1333”. In: *ApJ* 473, p. L49. doi: 10.1086/310381.
- Bally, J. *et al.* (2007). “Observations of Jets and Outflows from Young Stars”. In: *Protostars and Planets V*. Ed. by Bo Reipurth *et al.*, p. 215.
- Bally, John (2016). “Protostellar Outflows”. In: *ARA&A* 54, pp. 491–528. doi: 10.1146/annurev-astro-081915-023341.
- Bally, John and Bo Reipurth (2001). “Irradiated Herbig-Haro Jets in the Orion Nebula and near NGC 1333”. In: *ApJ* 546.1, pp. 299–323. doi: 10.1086/318258. arXiv: astro-ph/0009376 [astro-ph].
- Bally, John *et al.* (2002a). “Hubble Space Telescope Observations of Proper Motions in Herbig-Haro Objects 1 and 2”. In: *AJ* 123.5, pp. 2627–2657. doi: 10.1086/339837.
- (2002b). “Hubble Space Telescope Observations of Proper Motions in Herbig-Haro Objects 1 and 2”. In: *AJ* 123.5, pp. 2627–2657. doi: 10.1086/339837.
- Benedettini, M. *et al.* (2000). “The ISO spectroscopic view of the HH 24-26 region”. In: *A&A* 359, pp. 148–158.
- Benedettini, M. *et al.* (2012). “The CHESS survey of the L1157-B1 shock: the dissociative jet shock as revealed by Herschel-PACS”. In: *A&A* 539, L3, p. L3. doi: 10.1051/0004-6361/201118732. arXiv: 1202.1451 [astro-ph.GA].
- Beuther, H. *et al.* (2002). “Massive molecular outflows”. In: *A&A* 383, pp. 892–904. doi: 10.1051/0004-6361:20011808. arXiv: astro-ph/0110372 [astro-ph].

- Bittner, Hermann *et al.* (1998). “Optical system of the SOFIA Telescope”. In: *Space Telescopes and Instruments V*. Ed. by Pierre Y. Bely and James B. Breckinridge. Vol. 3356. Society of Photo-Optical Instrumentation Engineers (SPIE) Conference Series, pp. 512–521. doi: 10.1117/12.324474.
- Blandford, R. D. and D. G. Payne (1982). “Hydromagnetic flows from accretion disks and the production of radio jets.” In: *MNRAS* 199, pp. 883–903. doi: 10.1093/mnras/199.4.883.
- Bodenheimer, Peter H. (2011). *Principles of Star Formation*. doi: 10.1007/978-3-642-15063-0.
- Bontemps, S. *et al.* (1995). “Deep VLA search for the youngest protostars: A Class 0 source in the HH24-26 region”. In: *A&A* 297, pp. 98–102.
- Bontemps, S. *et al.* (1996). “Evolution of outflow activity around low-mass embedded young stellar objects”. In: *A&A* 311, pp. 858–872.
- Bouvier, J. *et al.* (2007). “Magnetospheric accretion-ejection processes in the classical T Tauri star AA Tauri”. In: *A&A* 463.3, pp. 1017–1028. doi: 10.1051/0004-6361:20066021. arXiv: astro-ph/0611787 [astro-ph].
- Bowen, I. S. (1927). “The Origin of the Nebulium Spectrum”. In: *Nature* 120.3022, p. 473. doi: 10.1038/120473a0.
- Brinch, C. *et al.* (2009). “The kinematics of NGC 1333-IRAS2A - a true Class 0 protostar”. In: *A&A* 502.1, pp. 199–205. doi: 10.1051/0004-6361/200810831. arXiv: 0905.4575 [astro-ph.GA].
- Bührke, T. *et al.* (1988). “A detailed study of HH 34 and its associated jet.” In: *A&A* 200, pp. 99–119.
- Burrows, Christopher J. *et al.* (1996). “Hubble Space Telescope Observations of the Disk and Jet of HH 30”. In: *ApJ* 473, p. 437. doi: 10.1086/178156.
- Cabrit, S. (1995). “Models of Molecular Outflows”. In: *Ap&SS* 233.1-2, pp. 81–96. doi: 10.1007/BF00627337.
- (2002). “Constraints on accretion-ejection structures in young stars”. In: *EAS Publications Series*. Ed. by Jerome Bouvier and Jean-Paul Zahn. Vol. 3. EAS Publications Series, pp. 147–182. doi: 10.1051/eas:2002049.
- Cabrit, S. *et al.* (2007). “PdBI sub-arcsecond study of the SiO microjet in HH212. Origin and collimation of class 0 jets”. In: *A&A* 468.3, pp. L29–L32. doi: 10.1051/0004-6361:20077387. arXiv: 0704.2685 [astro-ph].
- Cabrit, S. *et al.* (2012). “High SiO abundance in the HH212 protostellar jet”. In: *A&A* 548, L2, p. L2. doi: 10.1051/0004-6361/201219784. arXiv: 1211.1258 [astro-ph.GA].
- Camenzind, M. (1990). “Magnetized Disk-Winds and the Origin of Bipolar Outflows.” In: *Reviews in Modern Astronomy* 3, pp. 234–265. doi: 10.1007/978-3-642-76238-3_17.
- Caratti o Garatti, A. *et al.* (2006). “H₂ active jets in the near IR as a probe of protostellar evolution”. In: *A&A* 449, pp. 1077–1088. doi: 10.1051/0004-6361:20054313.

- Caratti o Garatti, A. *et al.* (2012). “POISSON project. II. A multi-wavelength spectroscopic and photometric survey of young protostars in L 1641”. In: *A&A* 538, A64, A64. doi: 10.1051/0004-6361/201117781. arXiv: 1111.2455 [astro-ph.SR].
- Carrasco-González, Carlos *et al.* (2010). “A Magnetized Jet from a Massive Protostar”. In: *Science* 330.6008, p. 1209. doi: 10.1126/science.1195589. arXiv: 1011.6254 [astro-ph.GA].
- Caselli, P. *et al.* (1997). “Grain-grain collisions and sputtering in oblique C-type shocks.” In: *A&A* 322, pp. 296–301.
- Casse, F. and J. Ferreira (2000). “Magnetized accretion-ejection structures. V. Effects of entropy generation inside the disc”. In: *A&A* 361, pp. 1178–1190. eprint: astro-ph/0008244.
- Ceccarelli, C. *et al.* (1997). “O I 63 Micron-determined Mass-Loss Rates in Young Stellar Objects”. In: *ApJ* 476, pp. 771–780. doi: 10.1086/303643.
- Ceccarelli, Cecilia *et al.* (1996). “Far-Infrared Line Emission from Collapsing Protostellar Envelopes”. In: *ApJ* 471, p. 400. doi: 10.1086/177978.
- Cerqueira, Adriano H. and Elisabete M. de Gouveia Dal Pino (1999). “Magnetic Field Effects on the Structure and Evolution of Overdense Radiatively Cooling Jets”. In: *ApJ* 510.2, pp. 828–845. doi: 10.1086/306615. arXiv: astro-ph/9808195 [astro-ph].
- Chen, H. *et al.* (1995). “Bolometric Temperature and Young Stars in the Taurus and Ophiuchus Complexes”. In: *ApJ* 445, p. 377. doi: 10.1086/175703.
- Chrysostomou, A. *et al.* (2000). “High-resolution near-infrared observations of Herbig-Haro flows - I. H₂ imaging and proper motions”. In: *MNRAS* 314, pp. 229–240. doi: 10.1046/j.1365-8711.2000.03304.x.
- Chrysostomou, A. *et al.* (2002). “High Resolution H[2] Observations of Herbig-Haro Flows”. In: *Revista Mexicana de Astronomia y Astrofisica Conference Series*. Ed. by W. J. Henney *et al.* Vol. 13. Revista Mexicana de Astronomia y Astrofisica Conference Series, pp. 16–20.
- Ciardi, A. *et al.* (2007). “The evolution of magnetic tower jets in the laboratory”. In: *Physics of Plasmas* 14.5, pp. 056501–056501. doi: 10.1063/1.2436479. arXiv: astro-ph/0611441 [astro-ph].
- Ciardi, Andrea *et al.* (2009). “Episodic Magnetic Bubbles and Jets: Astrophysical Implications from Laboratory Experiments”. In: *ApJ* 691.2, pp. L147–L150. doi: 10.1088/0004-637X/691/2/L147. arXiv: 0811.2736 [astro-ph].
- Clarke, David A. (1996). “A Consistent Method of Characteristics for Multidimensional Magnetohydrodynamics”. In: *ApJ* 457, p. 291. doi: 10.1086/176730.
- Codella, C. *et al.* (2007). “A highly-collimated SiO jet in the HH212 protostellar outflow”. In: *A&A* 462, pp. L53–L56. doi: 10.1051/0004-6361:20066800. eprint: astro-ph/0612482.

- Coffey, Deirdre *et al.* (2008). “T Tauri Jet Physics Resolved Near the Launching Region with the Hubble Space Telescope”. In: *ApJ* 689.2, pp. 1112–1126. doi: 10.1086/592343. arXiv: 0808.0617 [astro-ph].
- Cohen, M. *et al.* (1988). “Observations of the 63 micron forbidden O I line in Herbig-Haro objects”. In: *ApJ* 329, pp. 863–873. doi: 10.1086/166430.
- Colditz, S. *et al.* (2018). “Spectral and Spatial Characterization and Calibration of FIFI-LS —The Field Imaging Spectrometer on SOFIA”. In: *Journal of Astronomical Instrumentation* 7, 1840004, p. 1840004. doi: 10.1142/S2251171718400044.
- Contreras Peña, C. *et al.* (2017). “Infrared spectroscopy of eruptive variable protostars from VVV”. In: *MNRAS* 465.3, pp. 3039–3100. doi: 10.1093/mnras/stw2802. arXiv: 1602.06269 [astro-ph.SR].
- Davis, C. J. *et al.* (1997). “Near-IR imaging of the molecular outflows in HH24-26, L1634(HH240-241), L1660(HH72) and RNO15FIR.” In: *A&A* 324, pp. 263–275.
- Davis, C. J. *et al.* (2002). “Near-infrared Fabry-Perot imaging of Herbig-Haro energy sources: Collimated, small-scale H₂ jets and wide-angled winds”. In: *A&A* 382, pp. 1021–1031. doi: 10.1051/0004-6361:20011680.
- Davis, C. J. *et al.* (2003). “Near-IR echelle spectroscopy of Class I protostars: Mapping Forbidden Emission-Line (FEL) regions in [FeII]”. In: *A&A* 397, pp. 693–710. doi: 10.1051/0004-6361:20021545.
- Davis, C. J. *et al.* (2011a). “VLT integral field spectroscopy of embedded protostars: using near-infrared emission lines as tracers of accretion and outflow”. In: *A&A* 528, A3, A3. doi: 10.1051/0004-6361/201015897.
- (2011b). “VLT integral field spectroscopy of embedded protostars: using near-infrared emission lines as tracers of accretion and outflow”. In: *A&A* 528, A3, A3. doi: 10.1051/0004-6361/201015897.
- Davis, Christopher J. *et al.* (1994). “Near-Infrared Imaging of the Jets and Flows Associated with Herbig-Haro Objects HH 91, HH 110, and HH 111”. In: *ApJ* 437, p. L55. doi: 10.1086/187681.
- Davis, Christopher J. *et al.* (2000). “New, high-resolution, near-infrared observations of HH1”. In: *MNRAS* 318.3, pp. 747–752. doi: 10.1046/j.1365-8711.2000.03766.x.
- de Gouveia dal Pino, E. M. and R. Opher (1990). “Formation of condensations in young stellar outflows by a thermal instability”. In: *A&A* 231.2, pp. 571–580.
- de Gouveia dal Pino, Elisabete M. and Willy Benz (1993). “Three-dimensional Simulations of Protostellar Jets”. In: *ApJ* 410, p. 686. doi: 10.1086/172785.
- Devine, David *et al.* (1997). “New Herbig-Haro objects”. In: *Herbig-Haro Flows and the Birth of Stars*. Ed. by Bo Reipurth and Claude Bertout. Vol. 182. IAU Symposium, p. 91.
- (1999). “L1551 NE or L1551 IRS 5: Which Source Drives HH 28/29?” In: *AJ* 118.2, pp. 972–982. doi: 10.1086/300992.

- Dionatos, O. *et al.* (2010). “Spitzer spectral line mapping of the HH211 outflow”. In: *A&A* 521, A7, A7. doi: 10.1051/0004-6361/200913650. arXiv: 1006.0821 [astro-ph.GA].
- Dionatos, Odysseas and Manuel Güdel (2017). “Feedback of atomic jets from embedded protostars in NGC 1333”. In: *A&A* 597, A64, A64. doi: 10.1051/0004-6361/201629179. arXiv: 1608.06131 [astro-ph.SR].
- Dionatos, Odysseas *et al.* (2018). “Herschel spectral-line mapping of the HH211 protostellar system”. In: *A&A* 616, A84, A84. doi: 10.1051/0004-6361/201833057. arXiv: 1806.00311 [astro-ph.SR].
- Dougados, C. *et al.* (2002). “Probing the Origin of Mass Loss in T Tauri Stars”. In: *Revista Mexicana de Astronomia y Astrofisica Conference Series*. Ed. by William J. Henney *et al.* Vol. 13. Revista Mexicana de Astronomia y Astrofisica Conference Series, pp. 43–48.
- Dougados, C. *et al.* (2010). “Deriving Physical Diagnostics from Observations”. In: *Lecture Notes in Physics, Berlin Springer Verlag*. Ed. by P. J. V. Garcia and J. M. Ferreira. Vol. 793. Lecture Notes in Physics, Berlin Springer Verlag, p. 213. doi: 10.1007/978-3-642-02289-0_7.
- Draine, B. T. (1980). “Interstellar shock waves with magnetic precursors”. In: *ApJ* 241, pp. 1021–1038. doi: 10.1086/158416.
- Draine, B. T. *et al.* (1983). “Magnetohydrodynamic shock waves in molecular clouds.” In: *ApJ* 264, pp. 485–507. doi: 10.1086/160617.
- Draine, Bruce T. (2011). *Physics of the Interstellar and Intergalactic Medium*.
- Draine, Bruce T. and Christopher F. McKee (1993). “Theory of interstellar shocks.” In: *ARA&A* 31, pp. 373–432. doi: 10.1146/annurev.aa.31.090193.002105.
- Dunham, M. M. *et al.* (2014). “The Evolution of Protostars: Insights from Ten Years of Infrared Surveys with Spitzer and Herschel”. In: *Protostars and Planets VI*. Ed. by Henrik Beuther *et al.*, p. 195. doi: 10.2458/azu_uapress_9780816531240-ch009. arXiv: 1401.1809 [astro-ph.GA].
- Dyson, J. E. and D. A. Williams (1997). *The physics of the interstellar medium*. doi: 10.1201/9780585368115.
- Eddington, A. S. (1927). “The conditions of emission of forbidden lines”. In: *MNRAS* 88, pp. 134–138. doi: 10.1093/mnras/88.2.134.
- Eisloffel, J. and R. Mundt (1992). “Proper motion measurements in the HH34 jet and its associated bow shocks”. In: *A&A* 263, pp. 292–300.
- Eisloffel, Jochen (2000). “Parsec-scale molecular H₂ outflows from young stars”. In: *A&A* 354, pp. 236–246.
- Eisloffel, Jochen *et al.* (1994). “Structure and Proper Motions in Herbig-Haro Objects 1 and 2”. In: *AJ* 108, p. 1042. doi: 10.1086/117133.
- Eisloffel, Jochen *et al.* (1996). “Molecular Hydrogen in the Outflow From CEP E”. In: *AJ* 112, p. 2086. doi: 10.1086/118165.

- Ellerbroek, L. E. *et al.* (2013). “The outflow history of two Herbig-Haro jets in RCW 36: HH 1042 and HH 1043”. In: *A&A* 551, A5, A5. doi: 10.1051/0004-6361/201220635. arXiv: 1212.4144 [astro-ph.SR].
- Estalella, R. *et al.* (2012). “The Counterjet of HH 30: New Light on Its Binary Driving Source”. In: *AJ* 144, 61, p. 61. doi: 10.1088/0004-6256/144/2/61. arXiv: 1206.3391.
- Evans Neal J., II *et al.* (2009). “The Spitzer c2d Legacy Results: Star-Formation Rates and Efficiencies; Evolution and Lifetimes”. In: *ApJS* 181.2, pp. 321–350. doi: 10.1088/0067-0049/181/2/321. arXiv: 0811.1059 [astro-ph].
- Feeney-Johansson, Anton *et al.* (2019). “The First Detection of a Low-frequency Turnover in Nonthermal Emission from the Jet of a Young Star”. In: *ApJ* 885.1, L7, p. L7. doi: 10.3847/2041-8213/ab4b56. arXiv: 1910.09479 [astro-ph.SR].
- Ferreira, J. (1997). “Magnetically-driven jets from Keplerian accretion discs.” In: *A&A* 319, pp. 340–359. eprint: astro-ph/9607057.
- Ferreira, J. *et al.* (2006). “Which jet launching mechanism(s) in T Tauri stars?” In: *A&A* 453.3, pp. 785–796. doi: 10.1051/0004-6361:20054231. arXiv: astro-ph/0604053 [astro-ph].
- Fischer, C. *et al.* (2018). “FIFI-LS: The Field-Imaging Far-Infrared Line Spectrometer on SOFIA”. In: *Journal of Astronomical Instrumentation* 7, 1840003-556, pp. 1840003–556. doi: 10.1142/S2251171718400032.
- Fischer, W. J. *et al.* (2010). “Herschel-PACS imaging of protostars in the HH 1-2 outflow complex”. In: *A&A* 518, L122, p. L122. doi: 10.1051/0004-6361/201014636. arXiv: 1005.2183 [astro-ph.GA].
- Flower, D. R. and G. Pineau Des Forêts (2010). “Excitation and emission of H₂, CO and H₂O molecules in interstellar shock waves”. In: *MNRAS* 406.3, pp. 1745–1758. doi: 10.1111/j.1365-2966.2010.16834.x.
- Flower, D. R. and G. Pineau des Forêts (2015). “Interpreting observations of molecular outflow sources: the MHD shock code mhd_vode”. In: *A&A* 578, A63, A63. doi: 10.1051/0004-6361/201525740.
- Frank, A. *et al.* (2014). “Jets and Outflows from Star to Cloud: Observations Confront Theory”. In: *Protostars and Planets VI*. Ed. by Henrik Beuther *et al.*, p. 451. doi: 10.2458/azu_uapress_9780816531240-ch020. arXiv: 1402.3553 [astro-ph.SR].
- Fridlund, C. V. M. and R. Liseau (1994). “The velocity field of the L 1551 IRS 5 jet.” In: *A&A* 292, pp. 631–640.
- Fridlund, C. V. M. *et al.* (2002). “The molecular disk surrounding the protostellar binary L1551 IRS5”. In: *A&A* 382, pp. 573–582. doi: 10.1051/0004-6361:20011519.
- Fridlund, C. V. M. *et al.* (2005). “HST and spectroscopic observations of the L1551 IRS5 jets (HH154)”. In: *A&A* 436.3, pp. 983–997. doi: 10.1051/0004-6361:20042399. arXiv: astro-ph/0503469 [astro-ph].

- Froebrich, D. (2005). “Which Are the Youngest Protostars? Determining Properties of Confirmed and Candidate Class 0 Sources by Broadband Photometry”. In: *ApJS* 156.2, pp. 169–177. doi: 10.1086/426441. arXiv: astro-ph/0410044 [astro-ph].
- Froebrich, D. *et al.* (2003). “Far-infrared photometry of deeply embedded outflow sources”. In: *MNRAS* 346.1, pp. 163–176. doi: 10.1046/j.1365-2966.2003.07072.x. arXiv: astro-ph/0311158 [astro-ph].
- Garcia Lopez, R. *et al.* (2008). “IR diagnostics of embedded jets: velocity resolved observations of the HH34 and HH1 jets”. In: *A&A* 487.3, pp. 1019–1031. doi: 10.1051/0004-6361:20079045. arXiv: 0805.2841 [astro-ph].
- Garcia Lopez, R. *et al.* (2010). “IR diagnostics of embedded jets: kinematics and physical characteristics of the HH46-47 jet”. In: *A&A* 511, A5, A5. doi: 10.1051/0004-6361/200913304. arXiv: 0912.2043 [astro-ph.SR].
- Giannini, T. *et al.* (2001). “Far-Infrared Investigation of Class 0 Sources: Line Cooling”. In: *ApJ* 555, pp. 40–57. doi: 10.1086/321451.
- Giannini, T. *et al.* (2004). “On the excitation of the infrared knots along protostellar jets”. In: *A&A* 419, pp. 999–1014. doi: 10.1051/0004-6361:20040087. eprint: astro-ph/0402395.
- Giovanardi, C. *et al.* (2000). “Very Large Array Observations of High-Velocity H I in L1551”. In: *ApJ* 538.2, pp. 728–737. doi: 10.1086/309138.
- Goicoechea, Javier R. *et al.* (2015). “Herschel Far-infrared Spectral-mapping of Orion BN/KL Outflows: Spatial Distribution of Excited CO, H₂O, OH, O, and C⁺ in Shocked Gas”. In: *ApJ* 799.1, 102, p. 102. doi: 10.1088/0004-637X/799/1/102. arXiv: 1411.2930 [astro-ph.GA].
- Goldsmith, Paul F. (2019). “Modeling Collisional Excitation of [O I] Fine Structure Line Emission from PDRs. I. Homogeneous Clouds”. In: *ApJ* 887.1, 54, p. 54. doi: 10.3847/1538-4357/ab535e.
- Gómez-Ruiz, A. I. *et al.* (2012). “High-J CO emission in the Cepheus E protostellar outflow observed with SOFIA/GREAT”. In: *A&A* 542, L9, p. L9. doi: 10.1051/0004-6361/201218936. arXiv: 1203.1890 [astro-ph.GA].
- Gorti, U. and D. Hollenbach (2008). “Line Emission from Gas in Optically Thick Dust Disks around Young Stars”. In: *ApJ* 683.1, pp. 287–303. doi: 10.1086/589616. arXiv: 0804.3381 [astro-ph].
- Gorti, U. *et al.* (2011). “Emission Lines from the Gas Disk around TW Hydra and the Origin of the Inner Hole”. In: *ApJ* 735.2, 90, p. 90. doi: 10.1088/0004-637X/735/2/90. arXiv: 1104.4806 [astro-ph.EP].
- Graham, J. A. and M. H. Heyer (1990). “New optical features in L1551 and HH30”. In: *PASP* 102, pp. 972–977. doi: 10.1086/132725.
- Gramajo, Luciana V. *et al.* (2007). “High Spatial Resolution Near-Infrared Images of Taurus Protostars”. In: *AJ* 133.5, pp. 1911–1926. doi: 10.1086/512608.
- Gray, Richard O. and J. Corbally Christopher (2009). *Stellar Spectral Classification*.

- Green, J. D. *et al.* (2013). “Embedded Protostars in the Dust, Ice, and Gas In Time (DIGIT) Herschel Key Program: Continuum SEDs, and an Inventory of Characteristic Far-infrared Lines from PACS Spectroscopy”. In: *ApJ* 770, 123, p. 123. doi: 10.1088/0004-637X/770/2/123. arXiv: 1304.7389.
- Greene, Thomas P. *et al.* (1994). “Further Mid-Infrared Study of the rho Ophiuchi Cloud Young Stellar Population: Luminosities and Masses of Pre–Main-Sequence Stars”. In: *ApJ* 434, p. 614. doi: 10.1086/174763.
- Gueth, F. and S. Guilloteau (1999). “The jet-driven molecular outflow of HH 211”. In: *A&A* 343, pp. 571–584.
- Gullbring, E. *et al.* (1998). “Disk Accretion Rates for T Tauri Stars”. In: *ApJ* 492, pp. 323–341. doi: 10.1086/305032.
- Günther, Hans M. *et al.* (2019). “The fastest components in stellar jets”. In: *BAAS* 51.3, 401, p. 401. arXiv: 1903.09540 [astro-ph.SR].
- Gusdorf, A. *et al.* (2017). “Nature of shocks revealed by SOFIA OI observations in the Cepheus E protostellar outflow”. In: *A&A* 602, A8, A8. doi: 10.1051/0004-6361/201730454. arXiv: 1704.03796 [astro-ph.GA].
- Hanaoka, Yoichiro *et al.* (2018). “Solar Coronal Jets Extending to High Altitudes Observed during the 2017 August 21 Total Eclipse”. In: *ApJ* 860.2, 142, p. 142. doi: 10.3847/1538-4357/aac49b. arXiv: 1805.04251 [astro-ph.SR].
- Haro, Guillermo (1952). “Herbig’s Nebulous Objects Near NGC 1999.” In: *ApJ* 115, p. 572. doi: 10.1086/145576.
- Hartigan, P. *et al.* (1995). “Accretion and Outflow from Young Stars”. In: *Revista Mexicana de Astronomia y Astrofisica Conference Series*. Ed. by M. Pena and S. Kurtz. Vol. 3. Revista Mexicana de Astronomia y Astrofisica Conference Series, p. 93.
- Hartigan, P. *et al.* (2001). “Proper Motions of the HH 111 Jet Observed with the Hubble Space Telescope”. In: *ApJ* 559, pp. L157–L161. doi: 10.1086/323976.
- Hartigan, P. *et al.* (2011). “Fluid Dynamics of Stellar Jets in Real Time: Third Epoch Hubble Space Telescope Images of HH 1, HH 34, and HH 47”. In: *ApJ* 736.1, 29, p. 29. doi: 10.1088/0004-637X/736/1/29. arXiv: 1104.4341 [astro-ph.SR].
- Hartigan, P. *et al.* (2019). “Proper Motions and Shock Wave Dynamics in the HH 7-11 Stellar Jet”. In: *ApJ* 876.2, 147, p. 147. doi: 10.3847/1538-4357/ab18fa. arXiv: 1904.05983 [astro-ph.SR].
- Hartigan, Patrick (1989). “The Visibility of the Mach Disk and the Bow Shock of a Stellar Jet”. In: *ApJ* 339, p. 987. doi: 10.1086/167353.
- Hartigan, Patrick *et al.* (1994). “Mass-Loss Rates, Ionization Fractions, Shock Velocities, and Magnetic Fields of Stellar Jets”. In: *ApJ* 436, p. 125. doi: 10.1086/174887.
- Hartmann, Lee *et al.* (1998). “Accretion and the Evolution of T Tauri Disks”. In: *ApJ* 495.1, pp. 385–400. doi: 10.1086/305277.
- Hartmann, Lee *et al.* (2016). “Accretion onto Pre-Main-Sequence Stars”. In: *ARA&A* 54, pp. 135–180. doi: 10.1146/annurev-astro-081915-023347.

- Hatchell, J. *et al.* (2007). “Star formation in Perseus. III. Outflows”. In: *A&A* 472.1, pp. 187–198. doi: 10.1051/0004-6361:20066467. arXiv: 0706.1724 [astro-ph].
- Hayashi, Masahiko and Tae-Soo Pyo (2009). “Wide-Field Near-Infrared Imaging of the L1551 Dark Cloud”. In: *ApJ* 694.1, pp. 582–592. doi: 10.1088/0004-637X/694/1/582.
- Heathcote, S. and B. Reipurth (1992). “Kinematics and evolution of the HH 34 complex”. In: *AJ* 104, pp. 2193–2212. doi: 10.1086/116394.
- Herbig, G. H. (1974). “Draft Catalog of Herbig-Haro Objects.” In: *Lick Observatory Bulletin* 658, p. 1.
- Herbig, George H. (1951). “The Spectra of Two Nebulous Objects Near NGC 1999.” In: *ApJ* 113, pp. 697–699. doi: 10.1086/145440.
- Herczeg, Gregory J. and Lynne A. Hillenbrand (2008). “UV Excess Measures of Accretion onto Young Very Low Mass Stars and Brown Dwarfs”. In: *ApJ* 681.1, pp. 594–625. doi: 10.1086/586728. arXiv: 0801.3525 [astro-ph].
- Hester, J. Jeff *et al.* (1998). “Hubble Space Telescope Wide Field Planetary Camera 2 Observations of HH 1-2”. In: *AJ* 116.1, pp. 372–395. doi: 10.1086/300396.
- Hodapp, K. W. and R. Chini (2014). “The Launch Region of the SVS 13 Outflow and Jet”. In: *ApJ* 794, 169, p. 169. doi: 10.1088/0004-637X/794/2/169. arXiv: 1408.5940 [astro-ph.SR].
- Hogerheijde, Michiel R. *et al.* (1998). “Envelope Structure on 700 AU Scales and the Molecular Outflows of Low-Mass Young Stellar Objects”. In: *ApJ* 502.1, pp. 315–336. doi: 10.1086/305885.
- Hollenbach, D. (1985). “Mass loss rates from protostars and OI(63 micron) shock luminosities”. In: *Icarus* 61, pp. 36–39. doi: 10.1016/0019-1035(85)90151-4.
- Hollenbach, D. and C. F. McKee (1989). “Molecule formation and infrared emission in fast interstellar shocks. III - Results for J shocks in molecular clouds”. In: *ApJ* 342, pp. 306–336. doi: 10.1086/167595.
- Hollenbach, D. J. and A. G. G. M. Tielens (1997a). “Dense Photodissociation Regions (PDRs)”. In: *ARA&A* 35, pp. 179–216. doi: 10.1146/annurev.astro.35.1.179.
- (1997b). “Dense Photodissociation Regions (PDRs)”. In: *ARA&A* 35, pp. 179–216. doi: 10.1146/annurev.astro.35.1.179.
- Hollenbach, David (1997). “The Physics of Molecular Shocks in YSO Outflows”. In: *Herbig-Haro Flows and the Birth of Stars*. Ed. by Bo Reipurth and Claude Bertout. Vol. 182, pp. 181–198.
- Howard, Christian D. *et al.* (2013). “Herschel/PACS Survey of Protoplanetary Disks in Taurus/Auriga—Observations of [O I] and [C II], and Far-infrared Continuum”. In: *ApJ* 776.1, 21, p. 21. doi: 10.1088/0004-637X/776/1/21. arXiv: 1308.6019 [astro-ph.GA].

- Hsieh, Tien-Hao *et al.* (2019). “Chronology of Episodic Accretion in Protostars—An ALMA Survey of the CO and H₂O Snowlines”. In: *ApJ* 884.2, 149, p. 149. doi: 10.3847/1538-4357/ab425a. arXiv: 1909.02706 [astro-ph.GA].
- Itoh, Yoichi *et al.* (2000). “A Pair of Twisted Jets of Ionized Iron from L 1551 IRS 5”. In: *PASJ* 52, p. 81. doi: 10.1093/pasj/52.1.81.
- Jaquet, R. *et al.* (1992). “Excitation of the fine-structure transitions of O(³P_J) in collisions with ortho- and para-H₂”. In: *Journal of Physics B Atomic Molecular Physics* 25.1, pp. 285–297. doi: 10.1088/0953-4075/25/1/030.
- Kamp, I. *et al.* (2011). “Continuum and line modelling of discs around young stars. II. Line diagnostics for GASPS from the DENT grid”. In: *A&A* 532, A85, A85. doi: 10.1051/0004-6361/201016399. arXiv: 1103.5763 [astro-ph.SR].
- Karska, A. *et al.* (2013). “Water in star-forming regions with Herschel (WISH). III. Far-infrared cooling lines in low-mass young stellar objects”. In: *A&A* 552, A141, A141. doi: 10.1051/0004-6361/201220028. arXiv: 1301.4821 [astro-ph.SR].
- Karska, Agata *et al.* (2018). “The Herschel-PACS Legacy of Low-mass Protostars: The Properties of Warm and Hot Gas Components and Their Origin in Far-UV Illuminated Shocks”. In: *ApJS* 235.2, 30, p. 30. doi: 10.3847/1538-4365/aaaec5. arXiv: 1802.03379 [astro-ph.SR].
- Kaufman, Michael J. *et al.* (1999). “Far-Infrared and Submillimeter Emission from Galactic and Extragalactic Photodissociation Regions”. In: *ApJ* 527.2, pp. 795–813. doi: 10.1086/308102. arXiv: astro-ph/9907255 [astro-ph].
- Khanzadyan, T. *et al.* (2003). “A multi-epoch near-infrared study of the HH 7-11 protostellar outflow”. In: *MNRAS* 338, pp. 57–66. doi: 10.1046/j.1365-8711.2003.06087.x.
- Krabbe, Alfred (2000). “SOFIA telescope”. In: *Airborne Telescope Systems*. Ed. by Ramsey K. Melugin and Hans-Peter Röser. Vol. 4014. Society of Photo-Optical Instrumentation Engineers (SPIE) Conference Series, pp. 276–281. doi: 10.1117/12.389103. arXiv: astro-ph/0004253 [astro-ph].
- Krabbe, Alfred *et al.* (2013). “SOFIA, an airborne observatory for infrared astronomy”. In: *European Journal of Physics* 34.6, S161–S177. doi: 10.1088/0143-0807/34/6/s161. URL: <https://doi.org/10.1088/0143-0807/34/6/s161>.
- Krumholz, Mark R. (2015). “Notes on Star Formation”. In: *arXiv e-prints*, arXiv:1511.03457, arXiv:1511.03457. arXiv: 1511.03457 [astro-ph.GA].
- Kwan, J. H. *et al.* (1977). “On the molecular hydrogen emission at the Orion Nebula.” In: *ApJ* 216, pp. 713–723. doi: 10.1086/155514.
- Lada, Charles J. (1987). “Star formation: from OB associations to protostars.” In: *Star Forming Regions*. Ed. by Manuel Peimbert and Jun Jugaku. Vol. 115. IAU Symposium, p. 1.
- Ladd, E. F. and K. W. Hodapp (1997). “A Double Outflow from a Deeply Embedded Source in Cepheus”. In: *ApJ* 474.2, pp. 749–759. doi: 10.1086/303501.

- Lavalley-Fouquet, C. *et al.* (2000). “DG Tau: A shocking jet”. In: *A&A* 356, pp. L41–L44.
- Lebedev, S. V. *et al.* (2005). “Magnetic tower outflows from a radial wire array Z-pinch”. In: *MNRAS* 361.1, pp. 97–108. doi: 10.1111/j.1365-2966.2005.09132.x. arXiv: astro-ph/0505027 [astro-ph].
- Lee, Chin-Fei (2010). “A Change of Rotation Profile in the Envelope in the HH 111 Protostellar System: A Transition to a Disk?” In: *ApJ* 725.1, pp. 712–720. doi: 10.1088/0004-637X/725/1/712. arXiv: 1010.1310 [astro-ph.GA].
- (2020). “Molecular jets from low-mass young protostellar objects”. In: *A&A Rev.* 28.1, 1, p. 1. doi: 10.1007/s00159-020-0123-7. arXiv: 2002.05823 [astro-ph.GA].
- Lee, Chin-Fei *et al.* (2006). “Infall and Outflow around the HH 212 Protostellar System”. In: *ApJ* 639.1, pp. 292–302. doi: 10.1086/499297. arXiv: astro-ph/0511059 [astro-ph].
- Lee, Chin-Fei *et al.* (2007a). “HH 212: Submillimeter Array Observations of a Remarkable Protostellar Jet”. In: *ApJ* 659.1, pp. 499–511. doi: 10.1086/512540. arXiv: astro-ph/0701284 [astro-ph].
- Lee, Chin-Fei *et al.* (2007b). “Submillimeter Arcsecond-Resolution Mapping of the Highly Collimated Protostellar Jet HH 211”. In: *ApJ* 670.2, pp. 1188–1197. doi: 10.1086/522333. arXiv: 0708.1365 [astro-ph].
- (2007c). “Submillimeter Arcsecond-Resolution Mapping of the Highly Collimated Protostellar Jet HH 211”. In: *ApJ* 670.2, pp. 1188–1197. doi: 10.1086/522333. arXiv: 0708.1365 [astro-ph].
- Lee, Chin-Fei *et al.* (2010). “The Reflection-Symmetric Wiggle of the Young Protostellar Jet HH 211”. In: *ApJ* 713.2, pp. 731–737. doi: 10.1088/0004-637X/713/2/731. arXiv: 1003.1355 [astro-ph.GA].
- Lee, Chin-Fei *et al.* (2014a). “ALMA Results of the Pseudodisk, Rotating Disk, and Jet in the Continuum and HCO⁺ in the Protostellar System HH 212”. In: *ApJ* 786.2, 114, p. 114. doi: 10.1088/0004-637X/786/2/114. arXiv: 1403.5853 [astro-ph.GA].
- Lee, Chin-Fei *et al.* (2015). “Jet Motion, Internal Working Surfaces, and Nested Shells in the Protostellar System HH 212”. In: *ApJ* 805.2, 186, p. 186. doi: 10.1088/0004-637X/805/2/186. arXiv: 1503.07362 [astro-ph.GA].
- Lee, Chin-Fei *et al.* (2018). “A 100 au Wide Bipolar Rotating Shell Emanating from the HH 212 Protostellar Disk: A Disk Wind?” In: *ApJ* 856.1, 14, p. 14. doi: 10.3847/1538-4357/aaae6d. arXiv: 1802.03668 [astro-ph.GA].
- Lee, Jeong-Eun *et al.* (2014b). “Herschel Key Program, “Dust, Ice, and Gas In Time” (DIGIT): The Origin of Molecular and Atomic Emission in Low-mass Protostars in Taurus”. In: *ApJS* 214.2, 21, p. 21. doi: 10.1088/0067-0049/214/2/21. arXiv: 1407.3033 [astro-ph.SR].
- Lefèvre, C. *et al.* (2017). “CALYPSO view of SVS 13A with PdBI: Multiple jet sources”. In: *A&A* 604, L1, p. L1. doi: 10.1051/0004-6361/201730766. arXiv: 1707.02262 [astro-ph.GA].

- Lefloch, B. *et al.* (1996). “The remarkable Class 0 source CEP E”. In: *A&A* 313, pp. L17–L20.
- Lefloch, B. *et al.* (2015). “The structure of the Cepheus E protostellar outflow: The jet, the bowshock, and the cavity”. In: *A&A* 581, A4, A4. doi: 10.1051/0004-6361/201425521.
- Lefloch, Bertrand *et al.* (2007). “Anatomy of HH 111 from CO Observations: A Bow-Shock-driven Molecular Outflow”. In: *ApJ* 658.1, pp. 498–508. doi: 10.1086/509600. arXiv: astro-ph/0609567 [astro-ph].
- Lequeux, James (2005). *The Interstellar Medium*. doi: 10.1007/b137959.
- Lerate, M. R. *et al.* (2006). “A far-infrared molecular and atomic line survey of the Orion KL region”. In: *MNRAS* 370.2, pp. 597–628. doi: 10.1111/j.1365-2966.2006.10518.x. arXiv: astro-ph/0605410 [astro-ph].
- Lique, F. *et al.* (2018). “Fine-structure relaxation of O(³P) induced by collisions with He, H and H₂”. In: *MNRAS* 474, pp. 2313–2322. doi: 10.1093/mnras/stx2907.
- Liseau, R. *et al.* (1997). “Far-IR Spectrophotometry of HH Flows with the ISO Long-Wavelength Spectrometer”. In: *Herbig-Haro Flows and the Birth of Stars*. Ed. by Bo Reipurth and Claude Bertout. Vol. 182, pp. 111–120.
- Liseau, R. *et al.* (2006). “Outflows from young objects observed with the ISO-LWS. I. Fine structure lines [O I] 63 μm, [O I] 145 μm and [C II] 157 μm”. In: *A&A* 446, pp. 561–567. doi: 10.1051/0004-6361:20053925. eprint: astro-ph/0509836.
- Liseau, René *et al.* (2005). “Physics of Outflows: The Binary Protostar L1551 IRS 5 and its Jets”. In: *ApJ* 619.2, pp. 959–967. doi: 10.1086/426783. arXiv: astro-ph/0410405 [astro-ph].
- Livio, Mario (2004). “Astrophysical Jets”. In: *Baltic Astronomy* 13, pp. 273–279.
- Lizano, Susana *et al.* (1988). “Neutral Stellar Winds That Drive Bipolar Outflows in Low-Mass Protostars”. In: *ApJ* 328, p. 763. doi: 10.1086/166335.
- Looney, L. W. *et al.* (2000). “Realizing 3D spectral imaging in the far-infrared: FIFI LS”. In: *Airborne Telescope Systems*. Ed. by R. K. Melugin and H.-P. Röser. Vol. 4014. Proc. SPIE, pp. 14–22. doi: 10.1117/12.389112. eprint: astro-ph/0003303.
- Looney, Leslie W. *et al.* (2003). “FIFI LS: a far-infrared 3D spectral imager for SOFIA”. In: *Airborne Telescope Systems II*. Ed. by Ramsey K. Melugin and Hans-Peter Roeser. Vol. 4857. Society of Photo-Optical Instrumentation Engineers (SPIE) Conference Series, pp. 47–55. doi: 10.1117/12.458631.
- Lord, S. D. (1992). *A new software tool for computing Earth’s atmospheric transmission of near- and far-infrared radiation*. Tech. rep.
- Louvet, F. *et al.* (2018). “The HH30 edge-on T Tauri star. A rotating and precessing monopolar outflow scrutinized by ALMA”. In: *A&A* 618, A120, A120. doi: 10.1051/0004-6361/201731733. arXiv: 1808.03285 [astro-ph.GA].

- Malhotra, S. *et al.* (2001). “Far-Infrared Spectroscopy of Normal Galaxies: Physical Conditions in the Interstellar Medium”. In: *ApJ* 561.2, pp. 766–786. doi: 10.1086/323046. arXiv: astro-ph/0106485 [astro-ph].
- Maret, Sébastien *et al.* (2009). “Spitzer Mapping of Molecular Hydrogen Pure Rotational Lines in NGC 1333: A Detailed Study of Feedback in Star Formation”. In: *ApJ* 698.2, pp. 1244–1260. doi: 10.1088/0004-637X/698/2/1244. arXiv: 0904.0603 [astro-ph.SR].
- Masunaga, Hirohiko and Shu-ichiro Inutsuka (2000). “A Radiation Hydrodynamic Model for Protostellar Collapse. II. The Second Collapse and the Birth of a Protostar”. In: *ApJ* 531.1, pp. 350–365. doi: 10.1086/308439.
- McCaughrean, M. *et al.* (2002). “Standing on the shoulder of a giant: ISAAC, Antu, and star formation”. In: *The Messenger* 109, pp. 28–36.
- McKee, Christopher F. and Eve C. Ostriker (2007). “Theory of Star Formation”. In: *ARA&A* 45.1, pp. 565–687. doi: 10.1146/annurev.astro.45.051806.110602. arXiv: 0707.3514 [astro-ph].
- Miao, Y. *et al.* (2018). “A Blowout Jet Associated with One Obvious Extreme-ultraviolet Wave and One Complicated Coronal Mass Ejection Event”. In: *ApJ* 869.1, 39, p. 39. doi: 10.3847/1538-4357/aaeac1. arXiv: 1703.10022 [astro-ph.SR].
- Micono, M. *et al.* (1998). “Kelvin-Helmholtz instabilities in stellar jets. IV. On the origin of the emission knots”. In: *A&A* 333, pp. 1001–1006.
- Mighell, K. J. (1999). “CCD Aperture Photometry”. In: *Precision CCD Photometry*. Ed. by Eric R. Craine *et al.* Vol. 189. Astronomical Society of the Pacific Conference Series, p. 50.
- Molinari, S. *et al.* (2000). “Infrared Space Observatory Spectroscopy of HH 7-11 Flow and Its Redshifted Counterpart”. In: *ApJ* 538, pp. 698–709. doi: 10.1086/309161.
- Molinari, Sergio and Alberto Noriega-Crespo (2002). “Far-Infrared Spectroscopy of the HH 1/2 Outflow”. In: *AJ* 123.4, pp. 2010–2018. doi: 10.1086/339180. arXiv: astro-ph/0112400 [astro-ph].
- Moro-Martín, Amaya *et al.* (2001). “Infrared and Millimetric Study of the Young Outflow Cepheus E”. In: *ApJ* 555.1, pp. 146–159. doi: 10.1086/321443. arXiv: astro-ph/0103065 [astro-ph].
- Mottram, J. C. *et al.* (2017). “Outflows, infall and evolution of a sample of embedded low-mass protostars. The William Herschel Line Legacy (WILL) survey”. In: *A&A* 600, A99, A99. doi: 10.1051/0004-6361/201628682. arXiv: 1701.04647 [astro-ph.SR].
- Mundt, R. and J. W. Fried (1983). “Jets from young stars”. In: *ApJ* 274, pp. L83–L86. doi: 10.1086/184155.
- Mundt, R. *et al.* (1988). “A close association of five jet and outflow sources in the HL Tauri region”. In: *ApJ* 333, pp. L69–L72. doi: 10.1086/185283.

- Muzerolle, James *et al.* (1998). “A Brgamma Probe of Disk Accretion in T Tauri Stars and Embedded Young Stellar Objects”. In: *AJ* 116.6, pp. 2965–2974. doi: 10.1086/300636.
- Myers, P. C. and E. F. Ladd (1993). “Bolometric Temperatures of Young Stellar Objects”. In: *ApJ* 413, p. L47. doi: 10.1086/186956.
- Neufeld, David A. *et al.* (2019). “SOFIA/EXES Observations of Warm H₂ at High Spectral Resolution: Witnessing Para-to-ortho Conversion behind a Molecular Shock Wave in HH7”. In: *ApJ* 878.1, L18, p. L18. doi: 10.3847/2041-8213/ab2249. arXiv: 1905.10381 [astro-ph.GA].
- Newville, M. *et al.* (2016). *Lmfit: Non-Linear Least-Square Minimization and Curve-Fitting for Python*. Astrophysics Source Code Library. ascl: 1606.014.
- Nisini, B. (2008). “IR Spectroscopy of Jets: Diagnostics and HAR Observations”. In: *Jets from Young Stars II*. Ed. by Francesca Bacciotti *et al.* Vol. 742, p. 79.
- Nisini, B. *et al.* (1996). “LWS-spectroscopy of Herbig Haro objects and molecular outflows in the Cha II dark cloud.” In: *A&A* 315, pp. L321–L324.
- Nisini, B. *et al.* (2002). “1-2.5 μ m spectra of jets from young stars: Strong Fe II emission in HH111, HH240-241 and HH120”. In: *A&A* 393, pp. 1035–1051. doi: 10.1051/0004-6361:20021062.
- Nisini, B. *et al.* (2005). “A combined optical/infrared spectral diagnostic analysis of the HH1 jet”. In: *A&A* 441.1, pp. 159–170. doi: 10.1051/0004-6361:20053097. arXiv: astro-ph/0507074 [astro-ph].
- Nisini, B. *et al.* (2007). “Warm SiO gas in molecular bullets associated with protostellar outflows”. In: *A&A* 462.1, pp. 163–172. doi: 10.1051/0004-6361:20065621. arXiv: astro-ph/0610037 [astro-ph].
- Nisini, B. *et al.* (2015). “[O I] 63 μ m Jets in Class 0 Sources Detected By Herschel”. In: *ApJ* 801.2, 121, p. 121. doi: 10.1088/0004-637X/801/2/121. arXiv: 1501.03681 [astro-ph.SR].
- Nisini, B. *et al.* (2016). “The small-scale HH34 IRS jet as seen by X-shooter”. In: *A&A* 595, A76, A76. doi: 10.1051/0004-6361/201628853. arXiv: 1608.03792 [astro-ph.SR].
- Noriega-Crespo, A. *et al.* (2002). “Hubble Space Telescope NICMOS Images of the HH 7/11 Outflow in NGC 1333”. In: *ApJ* 580, pp. 959–968. doi: 10.1086/343784. eprint: astro-ph/0207605.
- Noriega-Crespo, A. *et al.* (2014). “Proper motions of young stellar outflows in the mid-infrared with Spitzer II HH 377/Cep E”. In: *New Journal of Physics* 16.10, 105008, p. 105008. doi: 10.1088/1367-2630/16/10/105008. arXiv: 1407.6009 [astro-ph.IM].
- Noriega-Crespo, A. *et al.* (2020). “The Jet/Counterjet Symmetry of the HH 212 Outflow”. In: *Rev. Mexicana Astron. Astrofis.* 56, pp. 29–38. doi: 10.22201/ia.01851101p.2020.56.01.05. arXiv: 1911.12297 [astro-ph.IM].

- Norman, M. L. *et al.* (1982). “Structure and dynamics of supersonic jets.” In: *A&A* 113, pp. 285–302.
- Norman, Michael L. (1990). “Fluid dynamics of astrophysical jets.” In: *Annals of the New York Academy of Sciences* 617, pp. 217–233. doi: 10.1111/j.1749-6632.1990.tb37807.x.
- (1996). “Structure and Dynamics of the 3D Supersonic Jet”. In: *Energy Transport in Radio Galaxies and Quasars*. Ed. by Philip E. Hardee *et al.* Vol. 100. Astronomical Society of the Pacific Conference Series, p. 319.
- Norman, Michael L. and Karl-Heinz A. Winkler (1985). *Supersonic jets*.
- O’Connell, B. *et al.* (2005). “The near-infrared excitation of the HH 211 protostellar outflow”. In: *A&A* 431, pp. 223–234. doi: 10.1051/0004-6361:20041821. arXiv: astro-ph/0502107 [astro-ph].
- Osorio, Mayra *et al.* (2003). “A Comprehensive Study of the L1551 IRS 5 Binary System”. In: *ApJ* 586.2, pp. 1148–1161. doi: 10.1086/367695. arXiv: astro-ph/0212074 [astro-ph].
- Osterbrock, Donald E. and Gary J. Ferland (2006). *Astrophysics of gaseous nebulae and active galactic nuclei*.
- Palla, Francesco and Steven W. Stahler (1999). “Star Formation in the Orion Nebula Cluster”. In: *ApJ* 525.2, pp. 772–783. doi: 10.1086/307928.
- Pesenti, N. *et al.* (2003). “Near-IR [Fe II] emission diagnostics applied to cold disk winds in young stars”. In: *A&A* 410, pp. 155–164. doi: 10.1051/0004-6361:20031131.
- Pilyugin, L. S. *et al.* (2003). “On the oxygen abundance in our Galaxy”. In: *A&A* 401, pp. 557–563. doi: 10.1051/0004-6361:20030139. arXiv: astro-ph/0302019 [astro-ph].
- Planck Collaboration *et al.* (2015). “Planck intermediate results. XXIII. Galactic plane emission components derived from Planck with ancillary data”. In: *A&A* 580, A13, A13. doi: 10.1051/0004-6361/201424434. arXiv: 1406.5093 [astro-ph.GA].
- Podio, L. *et al.* (2006). “Recipes for stellar jets: results of combined optical/infrared diagnostics”. In: *A&A* 456.1, pp. 189–204. doi: 10.1051/0004-6361:20054156. arXiv: astro-ph/0606280 [astro-ph].
- Podio, L. *et al.* (2012). “Herschel/PACS observations of young sources in Taurus: the far-infrared counterpart of optical jets”. In: *A&A* 545, A44, A44. doi: 10.1051/0004-6361/201219475. arXiv: 1207.3435 [astro-ph.SR].
- Podio, L. *et al.* (2015). “The jet and the disk of the HH 212 low-mass protostar imaged by ALMA: SO and SO₂ emission”. In: *A&A* 581, A85, A85. doi: 10.1051/0004-6361/201525778. arXiv: 1505.05919 [astro-ph.GA].
- Podio, L. *et al.* (2020). “The CALYPSO IRAM-PdBI survey of jets from Class 0 protostars. Are jets ubiquitous in young stars ?” In: *arXiv e-prints*, arXiv:2012.15379, arXiv:2012.15379. arXiv: 2012.15379 [astro-ph.SR].

- Pravdo, S. H. *et al.* (1985). “Detection of radio continuum emission from Herbig-Haro objects 1 and 2 and from their central exciting source.” In: *ApJ* 293, pp. L35–L38. doi: 10.1086/184486.
- Pudritz, R. E. *et al.* (2007). “Disk Winds, Jets, and Outflows: Theoretical and Computational Foundations”. In: *Protostars and Planets V*. Ed. by Bo Reipurth *et al.*, p. 277. arXiv: astro-ph/0603592 [astro-ph].
- Pudritz, Ralph E. and Tom P. Ray (2019). “The Role of Magnetic Fields in Protostellar Outflows and Star Formation”. In: *Frontiers in Astronomy and Space Sciences* 6, 54, p. 54. doi: 10.3389/fspas.2019.00054. arXiv: 1912.05605 [astro-ph.SR].
- Pyo, Tae-Soo *et al.* (2009). “Spatio-Kinematic Structure at the Base of the [Fe II] Jets from L1551 IRS 5”. In: *ApJ* 694.1, pp. 654–663. doi: 10.1088/0004-637X/694/1/654. arXiv: 0901.2105 [astro-ph.HE].
- Raga, A. C. *et al.* (1990). “Stellar Jets with Intrinsically Variable Sources”. In: *ApJ* 364, p. 601. doi: 10.1086/169443.
- Raga, A. C. *et al.* (2011). “An overview of the observational and theoretical studies of HH 1 and 2”. In: *Rev. Mexicana Astron. Astrofis.* 47, pp. 425–437.
- Ray, T. P. (2007). “The generation of jets from young stars: an observational perspective”. In: *Star-Disk Interaction in Young Stars*. Ed. by Jerome Bouvier and Immo Appenzeller. Vol. 243, pp. 183–194. doi: 10.1017/S1743921307009544.
- Ray, T. P. and J. Ferreira (2020). “Jets from Young Stars”. In: *arXiv e-prints*, arXiv:2009.00547, arXiv:2009.00547. arXiv: 2009.00547 [astro-ph.SR].
- Ray, Thomas P. *et al.* (1996). “HST Observations of Jets from Young Stars”. In: *ApJ* 468, p. L103. doi: 10.1086/310239.
- Reipurth, B. (1989). “The HH111 jet and multiple outflow episodes from young stars”. In: *Nature* 340, pp. 42–45. doi: 10.1038/340042a0.
- (2000). “VizieR Online Data Catalog: General Catalogue of Herbig-Haro Objects (Reipurth+, 1999)”. In: *VizieR Online Data Catalog*, V/104, pp. V/104.
- Reipurth, B. *et al.* (2002). “Hubble Space Telescope Images of the HH 34 Jet and Bow Shock: Structure and Proper Motions”. In: *AJ* 123, pp. 362–381. doi: 10.1086/324738.
- Reipurth, Bo and John Bally (2001). “Herbig-Haro Flows: Probes of Early Stellar Evolution”. In: *ARA&A* 39, pp. 403–455. doi: 10.1146/annurev.astro.39.1.403.
- Reipurth, Bo and Steve Heathcote (1997). “50 Years of Herbig-Haro Research. From discovery to HST”. In: *Herbig-Haro Flows and the Birth of Stars*. Ed. by Bo Reipurth and Claude Bertout. Vol. 182, pp. 3–18.
- Reipurth, Bo *et al.* (1997). “Hubble Space Telescope Images of the HH 111 Jet.” In: *AJ* 114, pp. 757–780. doi: 10.1086/118509.
- Reipurth, Bo *et al.* (1998). “Protostellar jets irradiated by massive stars”. In: *Nature* 396.6709, pp. 343–345. doi: 10.1038/24562.

- Reipurth, Bo *et al.* (1999). “Multiplicity of the HH 111 jet source: it Hubble Space Telescope NICMOS images and VLA maps”. In: *A&A* 352, pp. L83–L86.
- Richer, J. S. *et al.* (2000). “Molecular Outflows from Young Stellar Objects”. In: *Protostars and Planets IV*. Ed. by V. Mannings *et al.*, p. 867. arXiv: astro-ph/9904097 [astro-ph].
- Rieke, G. H. and M. J. Lebofsky (1985). “The interstellar extinction law from 1 to 13 microns.” In: *ApJ* 288, pp. 618–621. doi: 10.1086/162827.
- Rigliaco, E. *et al.* (2012). “X-shooter spectroscopy of young stellar objects. I. Mass accretion rates of low-mass T Tauri stars in σ Orionis”. In: *A&A* 548, A56, A56. doi: 10.1051/0004-6361/201219832. arXiv: 1209.5799 [astro-ph.SR].
- Riviere-Marichalar, P. *et al.* (2012). “HD 172555: detection of 63 μ m [OI] emission in a debris disc”. In: *A&A* 546, L8, p. L8. doi: 10.1051/0004-6361/201219745. arXiv: 1210.0089 [astro-ph.SR].
- Riviere-Marichalar, P. *et al.* (2016). “Herschel-PACS observations of far-IR lines in young stellar objects. I. [OI] and H₂O at 63 μ m”. In: *A&A* 594, A59, A59. doi: 10.1051/0004-6361/201527829. arXiv: 1607.07991 [astro-ph.SR].
- Robitaille, Thomas P. *et al.* (2006). “Interpreting Spectral Energy Distributions from Young Stellar Objects. I. A Grid of 200,000 YSO Model SEDs”. In: *ApJS* 167.2, pp. 256–285. doi: 10.1086/508424. arXiv: astro-ph/0608234 [astro-ph].
- Rodríguez, Luis F. *et al.* (2000). “New VLA Observations of the HH 1-2 Region: Evidence for Density Enhancements Moving along the Axis of the VLA 1 Radio Jet”. In: *AJ* 119.2, pp. 882–889. doi: 10.1086/301231.
- Rodríguez, Luis F. *et al.* (2014). “Radio Continuum Sources associated with the HH 92 and HH 34 Jets”. In: *Rev. Mexicana Astron. Astrofis.* 50, pp. 285–291. arXiv: 1405.6638 [astro-ph.SR].
- Rosen, A. and M. D. Smith (2004). “Numerical simulations of highly collimated protostellar outflows. The effects of relative density”. In: *A&A* 413, pp. 593–607. doi: 10.1051/0004-6361:20031566.
- Russell, H. N. and F. A. Saunders (1925). “New Regularities in the Spectra of the Alkaline Earths”. In: *ApJ* 61, p. 38. doi: 10.1086/142872.
- Sadun, Alberto C. and Philip Morrison (2002). “Hercules A (3C 348): Phenomenology of an Unusual Active Galactic Nucleus”. In: *AJ* 123.5, pp. 2312–2320. doi: 10.1086/339829.
- Schilke, P. *et al.* (1997). “SiO production in interstellar shocks.” In: *A&A* 321, pp. 293–304.
- Schwartz, R. D. (1975). “T Tauri nebulae and Herbig-Haro nebulae: evidence for excitation by a strong stellar wind.” In: *ApJ* 195, pp. 631–642. doi: 10.1086/153364.
- (1977). “Evidence of star formation triggered by expansion of the Gum Nebula.” In: *ApJ* 212, pp. L25–L26. doi: 10.1086/182367.

- (1978). “A shocked cloudlet model for Herbig-Haro objects.” In: *ApJ* 223, pp. 884–900. doi: 10.1086/156321.
- Shu, F. *et al.* (1994). “Magnetocentrifugally driven flows from young stars and disks. 1: A generalized model”. In: *ApJ* 429, pp. 781–796. doi: 10.1086/174363.
- Shu, F. H. *et al.* (1988). “Mass loss from rapidly rotating magnetic protostars”. In: *ApJ* 328, pp. L19–L23. doi: 10.1086/185152.
- Shu, F. H. *et al.* (2000). “X-Winds Theory and Observations”. In: *Protostars and Planets IV*. Ed. by V. Mannings *et al.*, pp. 789–814.
- Smith, M. D. and P. W. J. L. Brand (1990). “H₂ profiles of C-type bow shocks.” In: *MNRAS* 245, p. 108.
- Smith, M. D. *et al.* (2003). “Anatomy of the Herbig-Haro object HH7 bow shock”. In: *MNRAS* 339, pp. 524–536. doi: 10.1046/j.1365-8711.2003.06195.x.
- Smith, M. D. *et al.* (2007). “The excitation within the molecular hydrogen jets of the protostellar outflow HH 212”. In: *A&A* 466.2, pp. 565–577. doi: 10.1051/0004-6361:20066734.
- Smith, Nathan *et al.* (2010). “HST/ACS H α imaging of the Carina Nebula: outflow activity traced by irradiated Herbig-Haro Jets”. In: *MNRAS* 405.2, pp. 1153–1186. doi: 10.1111/j.1365-2966.2010.16520.x. arXiv: 1002.4898 [astro-ph.SR].
- Snell, R. L. *et al.* (1980). “Observations of CO in L 1551 : evidence for stellar wind driven shocks.” In: *ApJ* 239, pp. L17–L22. doi: 10.1086/183283.
- Sperling, T. *et al.* (2020). “Probing the hidden atomic gas in Class I jets with SOFIA”. In: *A&A* 642, A216, A216. doi: 10.1051/0004-6361/201937242. arXiv: 2010.09314 [astro-ph.GA].
- Stanke, Thomas (2001). “An unbiased infrared H₂ search for embedded flows from young stars in Orion A”. PhD thesis. Universität Potsdam.
- Stone, James M. and Michael L. Norman (1992). “ZEUS-2D: A Radiation Magnetohydrodynamics Code for Astrophysical Flows in Two Space Dimensions. I. The Hydrodynamic Algorithms and Tests”. In: *ApJS* 80, p. 753. doi: 10.1086/191680.
- Strom, K. M. *et al.* (1976). “Infrared surveys of dark-cloud complexes. I. The Lynds 1630 dark cloud.” In: *AJ* 81, pp. 308–313. doi: 10.1086/111888.
- Tanabe, Yoshihiro *et al.* (2019). “Nobeyama 45 m mapping observations toward Orion A. I. Molecular Outflows”. In: *PASJ* 71, S8, S8. doi: 10.1093/pasj/psz100. arXiv: 1910.07495 [astro-ph.SR].
- Temi, Pasquale *et al.* (2014). “The SOFIA Observatory at the Start of Routine Science Operations: Mission Capabilities and Performance”. In: *ApJS* 212.2, 24, p. 24. doi: 10.1088/0067-0049/212/2/24. arXiv: 1405.7390 [astro-ph.IM].
- Tennyson, Jonathan (2019). *Astronomical Spectroscopy. An Introduction to the Atomic and Molecular Physics of Astronomical Spectroscopy*. doi: 10.1142/q0207.
- Tobin, John J. *et al.* (2016). “The VLA Nascent Disk and Multiplicity Survey of Perseus Protostars (VANDAM). II. Multiplicity of Protostars in the Perseus Molecular Cloud”.

- In: *ApJ* 818.1, 73, p. 73. doi: 10.3847/0004-637X/818/1/73. arXiv: 1601.00692 [astro-ph.SR].
- Tsinganos, Kanaris (2010). “MHD theory of astrophysical jets”. In: *Memorie della Societa Astronomica Italiana Supplementi* 15, p. 102.
- Tychoniec, Łukasz *et al.* (2020). “Dust masses of young disks: constraining the initial solid reservoir for planet formation”. In: *A&A* 640, A19, A19. doi: 10.1051/0004-6361/202037851. arXiv: 2006.02812 [astro-ph.EP].
- Vacca, G. M. (2016). *Guest Investigator Handbook for FIFI-LS Data Products*. Tech. rep.
- van Dishoeck, E. F. *et al.* (2011). “Water in Star-forming Regions with the Herschel Space Observatory (WISH). I. Overview of Key Program and First Results”. In: *PASP* 123.900, p. 138. doi: 10.1086/658676. arXiv: 1012.4570 [astro-ph.GA].
- van Kempen, T. A. *et al.* (2009). “Dense and warm molecular gas in the envelopes and outflows of southern low-mass protostars”. In: *A&A* 508.1, pp. 259–274. doi: 10.1051/0004-6361/200811099. arXiv: 0910.1034 [astro-ph.SR].
- van Kempen, T. A. *et al.* (2010). “Origin of the hot gas in low-mass protostars. Herschel-PACS spectroscopy of HH 46”. In: *A&A* 518, L121, p. L121. doi: 10.1051/0004-6361/201014615. arXiv: 1005.2031 [astro-ph.SR].
- Velusamy, T. *et al.* (2011). “Jets and Wide-angle Outflows in Cepheus E: New Evidence from Spitzer”. In: *ApJ* 741.1, 60, p. 60. doi: 10.1088/0004-637X/741/1/60. arXiv: 1108.3578 [astro-ph.GA].
- Vieira, Daniel and Roman V. Krems (2017). “Rate Constants for Fine-structure Excitations in O-H Collisions with Error Bars Obtained by Machine Learning”. In: *ApJ* 835.2, 255, p. 255. doi: 10.3847/1538-4357/835/2/255. arXiv: 1701.01897 [astro-ph.GA].
- Vig, S. *et al.* (2018). “Detection of non-thermal emission from the massive protostellar jet HH80-81 at low radio frequencies using GMRT”. In: *MNRAS* 474.3, pp. 3808–3816. doi: 10.1093/mnras/stx3032. arXiv: 1711.07642 [astro-ph.SR].
- Walawender, Josh *et al.* (2005). “Deep Imaging Surveys of Star-forming Clouds. III. Herbig-Haro Objects in the Perseus Molecular Cloud”. In: *AJ* 129.5, pp. 2308–2351. doi: 10.1086/428955.
- Watson, D. M. *et al.* (2016). “Evolution of Mass Outflow in Protostars”. In: *ApJ* 828, 52, p. 52. doi: 10.3847/0004-637X/828/1/52. arXiv: 1511.04787 [astro-ph.SR].
- White, G. J. *et al.* (2000). “An infrared study of the L1551 star formation region”. In: *A&A* 364, pp. 741–762.
- White, Russel J. and Lynne A. Hillenbrand (2004). “On the Evolutionary Status of Class I Stars and Herbig-Haro Energy Sources in Taurus-Auriga”. In: *ApJ* 616.2, pp. 998–1032. doi: 10.1086/425115. arXiv: astro-ph/0408244 [astro-ph].
- Wood, Kenneth *et al.* (2002). “The Spectral Energy Distribution of HH 30 IRS: Constraining the Circumstellar Dust Size Distribution”. In: *ApJ* 564.2, pp. 887–895. doi: 10.1086/324285. arXiv: astro-ph/0109048 [astro-ph].

- Yang, Ji *et al.* (1997). “Detection of Infall Motion from the Circumstellar Disk Associated with the Exciting Source of HH 111”. In: *ApJ* 475.2, pp. 683–692. doi: 10.1086/303558.
- Yang, Yao-Lun *et al.* (2017). “The Class 0 Protostar BHR71: Herschel Observations and Dust Continuum Models”. In: *ApJ* 835.2, 259, p. 259. doi: 10.3847/1538-4357/835/2/259. arXiv: 1701.00803 [astro-ph.SR].
- Yang, Yao-Lun *et al.* (2018). “CO in Protostars (COPS): Herschel-SPIRE Spectroscopy of Embedded Protostars”. In: *ApJ* 860.2, 174, p. 174. doi: 10.3847/1538-4357/aac2c6. arXiv: 1805.00957 [astro-ph.GA].
- Yıldız, U. A. *et al.* (2015). “APEX-CHAMP⁺ high-J CO observations of low-mass young stellar objects. IV. Mechanical and radiative feedback”. In: *A&A* 576, A109, A109. doi: 10.1051/0004-6361/201424538. arXiv: 1501.03259 [astro-ph.SR].
- Yoshida, Tomohiro *et al.* (2021). “Multi-epoch Submillimeter Array Observations of the L1448C(N) Protostellar SiO Jet”. In: *ApJ* 906.2, 112, p. 112. doi: 10.3847/1538-4357/abc94f. arXiv: 2011.04882 [astro-ph.SR].
- Young, E. T. *et al.* (2012). “Early Science with SOFIA, the Stratospheric Observatory For Infrared Astronomy”. In: *ApJ* 749, L17, p. L17. doi: 10.1088/2041-8205/749/2/L17. arXiv: 1205.0791 [astro-ph.IM].
- Zinnecker, H. (2013). “SOFIA: first science highlights and future science potential”. In: *Astronomische Nachrichten* 334.6, pp. 558–575. doi: 10.1002/asna.201311908.
- Zinnecker, Hans *et al.* (1998). “A symmetrically pulsed jet of gas from an invisible protostar in Orion”. In: *Nature* 394.6696, pp. 862–865. doi: 10.1038/29716.
- Zucker, Catherine *et al.* (2019). “A Large Catalog of Accurate Distances to Local Molecular Clouds: The Gaia DR2 Edition”. In: *ApJ* 879.2, 125, p. 125. doi: 10.3847/1538-4357/ab2388. arXiv: 1902.01425 [astro-ph.GA].

APPENDIX A

Accretion rates of Cep E and SVS 13

Cep E: In the case of Cep E we decided to estimate its accretion rate using the same approach as presented in Section 5.4, but with different stellar parameters. The reason for this is, that Cep E-mm is an intermediate-mass protostar ($M_\star \sim 2 - 5 M_\odot$, e.g. Velusamy *et al.* 2011), thus appearing as a scaled-up version of the remaining low mass protostars of our sample (see references in Frank *et al.* 2014; Hartmann *et al.* 2016). Assuming the stellar parameters for Cep E-mm to be $M_\star \sim 3 M_\odot$ (Velusamy *et al.* 2011), $L_{\text{bol}} \sim 80 L_\odot$ (Froebrich *et al.* 2003), and $R_\star \sim 20 R_\odot$ (Velusamy *et al.* 2011), and assuming further that $L_{\text{acc}} \approx L_{\text{bol}}$, we estimate the accretion rate via (McKee and Ostriker 2007)

$$\left(\frac{\dot{M}_{\text{acc}}}{10^{-6} M_\odot \text{ yr}^{-1}} \right) \approx \frac{1}{3.1 f_{\text{acc}}} \left(\frac{0.25 M_\odot}{M_\star} \right) \left(\frac{R_\star}{2.5 R_\odot} \right) \left(\frac{L_{\text{acc}}}{L_\odot} \right). \quad (\text{A.1})$$

With $f_{\text{acc}} \approx 1$ (fraction of the gravitational potential energy released by accretion) we get $\dot{M}_{\text{acc}} \sim 1.7 \times 10^{-5} M_\odot \text{ yr}^{-1}$ for Cep E-mm.

SVS13: The accretion rate of SVS13 can be estimated via the emission in the Bry line at $\lambda = 2.166 \mu\text{m}$. Davis *et al.* (2011a) measure a line flux of $F_{\text{Bry}}^{\text{obs}} = (249 \pm 5) \times 10^{-17} \text{ W m}^{-2}$. We correct this line flux assuming the extinction law (Rieke and Lebofsky 1985)

$$A_\lambda/A_v = (\lambda_v/\lambda)^{1.6}, \quad (\text{A.2})$$

and

$$F_{\text{Bry}}^0 = F_{\text{Bry}}^{\text{obs}} \times 10^{A_\lambda/2.5}, \quad (\text{A.3})$$

whereby A_v represents the visual extinction at $\lambda_v = 0.55 \mu\text{m}$ and F_{Bry}^0 is the extinction corrected line flux. We assume $A_v = 10$ (Davis *et al.* 2011b). Thus, at $D = 235 \text{ pc}$ we get a line luminosity of $L(\text{Bry}) \approx 1.2 \times 10^{-2} L_\odot$. Therefore, the accretion luminosity estimated via

$$\log(L_{\text{acc}}/L_\odot) = a \times \log(L(\text{Bry})/L_\odot) + b,$$

with $a = 1.19 \pm 0.10$ and $b = 4.02 \pm 0.51$ (Alcalá *et al.* 2017) is $L_{\text{acc}} \approx 54 L_\odot$. This value is consistent with the bolometric luminosity stated in Davis *et al.* (2011b),

that is $L_{\text{bol}} = 50 - 80 L_{\odot}$. Inferring the fiducial values of the protostellar mass and radius of $M_{\star} = 0.5 M_{\odot}$ and $R_{\star} = 4 R_{\odot}$ respectively, we calculate a mass accretion rate of (Gullbring *et al.* 1998)

$$\dot{M}_{\text{acc}} = \frac{L_{\text{acc}} R_{\star}}{GM_{\star}} \approx 1.4 \times 10^{-5} M_{\odot} \text{ yr}^{-1}.$$

The accretion rate might be even higher by a factor of $(1 - R_{\star}/R_i)^{-1}$. In consideration of $R_i = 5 R_{\star}$ the corresponding mass accretion rate is $\dot{M}_{\text{acc}} = 1.7 \times 10^{-5} M_{\odot} \text{ yr}^{-1}$.

APPENDIX B

Detected continuum sources and their fluxes

The obtained continuum maps for the nine observed outflows are presented in Fig. B.1-B.9. From these maps continuum fluxes for the detected sources are measured as described below. The 2D Gaussian function

$$\Phi_s(x, y) = \frac{A_s}{2\pi\sigma_s^2} \exp\left(-\frac{(x - x_s)^2 + (y - y_s)^2}{2\sigma_s^2}\right) + B_s \quad (\text{B.1})$$

with the free parameters x_s , y_s , A_s , σ_s , and B_s was fitted to each detected continuum source. Here, the radial distance from the center (x_s, y_s) of the 2D Gaussian is specified as $r^2 = (x - x_s)^2 + (y - y_s)^2$. The quantities A_s , B_s , and σ_s correspond to the peak flux amplitude of the source, the continuum background, and the standard deviation, respectively. Thus, the total background-corrected flux within a circular aperture of radius $R > 0$ is given in polar coordinates (r, φ) by

$$F_\lambda = \int_{\varphi=0}^{2\pi} \int_{r=0}^R \frac{A_s}{2\pi\sigma_s^2} \exp\left(-\frac{r^2}{2\sigma_s^2}\right) r dr d\varphi = A_s \cdot \left[1 - \exp\left(-\frac{R^2}{2\sigma_s^2}\right)\right]. \quad (\text{B.2})$$

Table B.1 lists all determined fluxes choosing an aperture radius of $R = 1.5\sigma_s$ (Mighell 1999) corresponding to $F_\lambda \approx 0.6753 A_s$. (For $R = \sqrt{2 \ln 2} \sigma_s$ and $R = \infty$ the corresponding fluxes are $0.5 A_s$ and $1.0 A_s$, respectively.)

Tab. B.1. Measured continuum fluxes of our objects at the observed [OI] transitions. The listed values correspond to the background-corrected flux within an aperture of radius $1.5\sigma_s$.

Target	$F_{63\mu\text{m}}$ ($10^{-13} \text{ erg s}^{-1} \text{ cm}^{-2} \mu\text{m}^{-1}$)	$F_{145\mu\text{m}}$ ($10^{-13} \text{ erg s}^{-1} \text{ cm}^{-2} \mu\text{m}^{-1}$)
Cep E (IRAS 23011+6126)	361.4 ± 9.4	170.3 ± 1.7
HH 1 (VLA 1)	127.7 ± 14.1	117.8 ± 1.1
HH 1 radio source	–	223.2 ± 3.0
HH 212 (IRAS 05413-0104)	95.3 ± 8.3	81.3 ± 1.5
HH26 IRS	–	13.7 ± 0.9
HH34 IRS	312.0 ± 19.5	36.6 ± 2.0
HH 111 IRS	255.2 ± 6.9	61.9 ± 1.4
L1551 IRS5	1857.7 ± 24.5	572.4 ± 7.0
SVS 13	1335.6 ± 14.5	245.1 ± 1.9
HH30 IRS	–	–

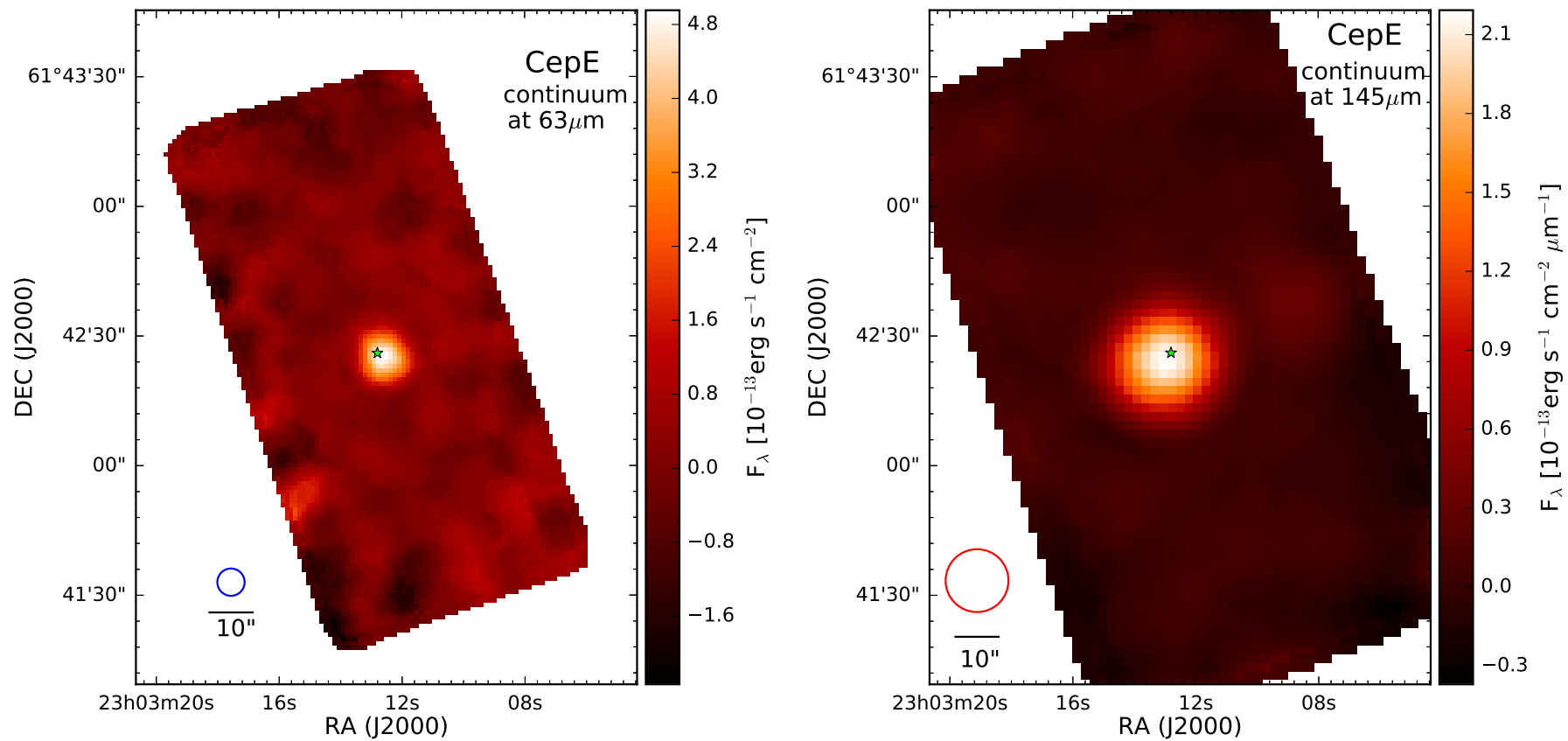
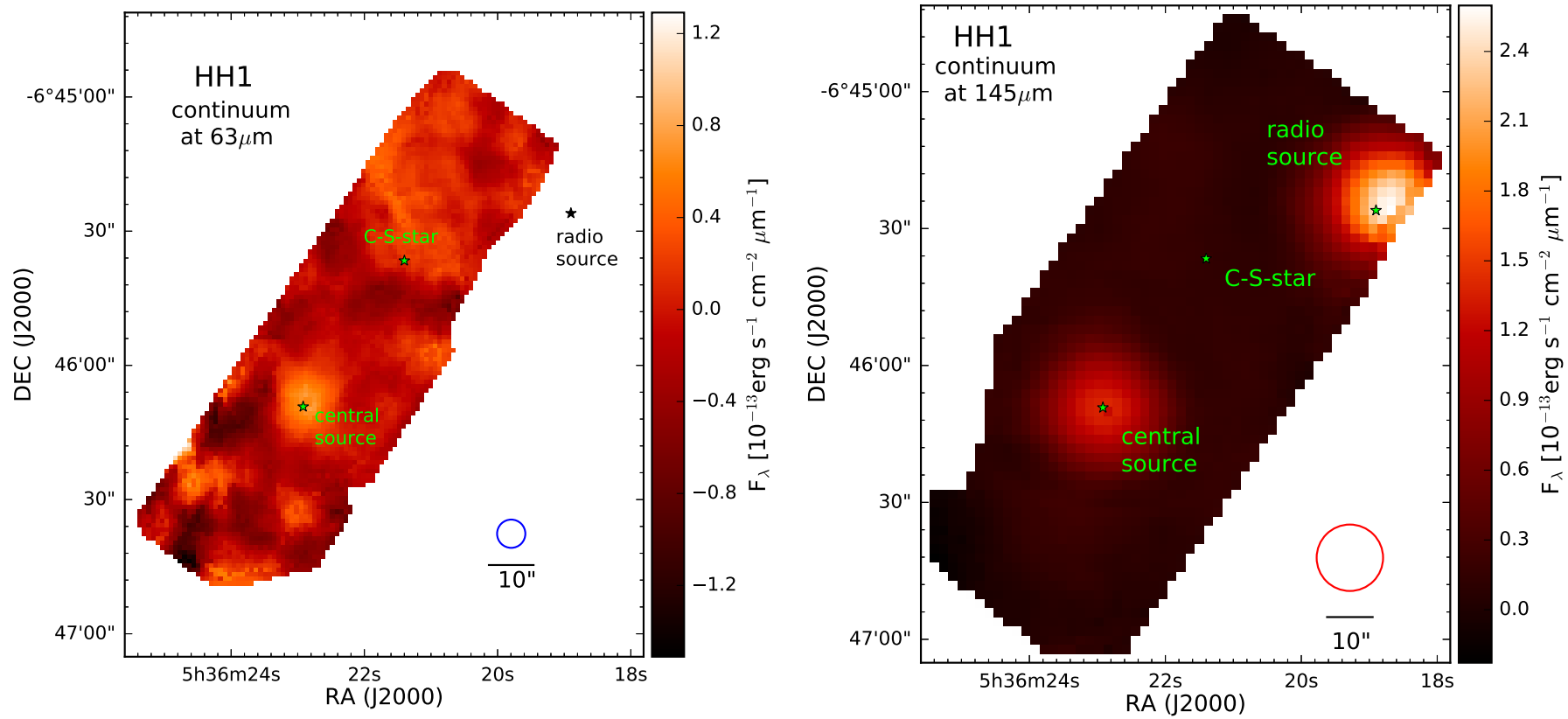


Fig. B.1. Continuum maps of Cep E.

**Fig. B.2.** Continuum maps of HH 1.

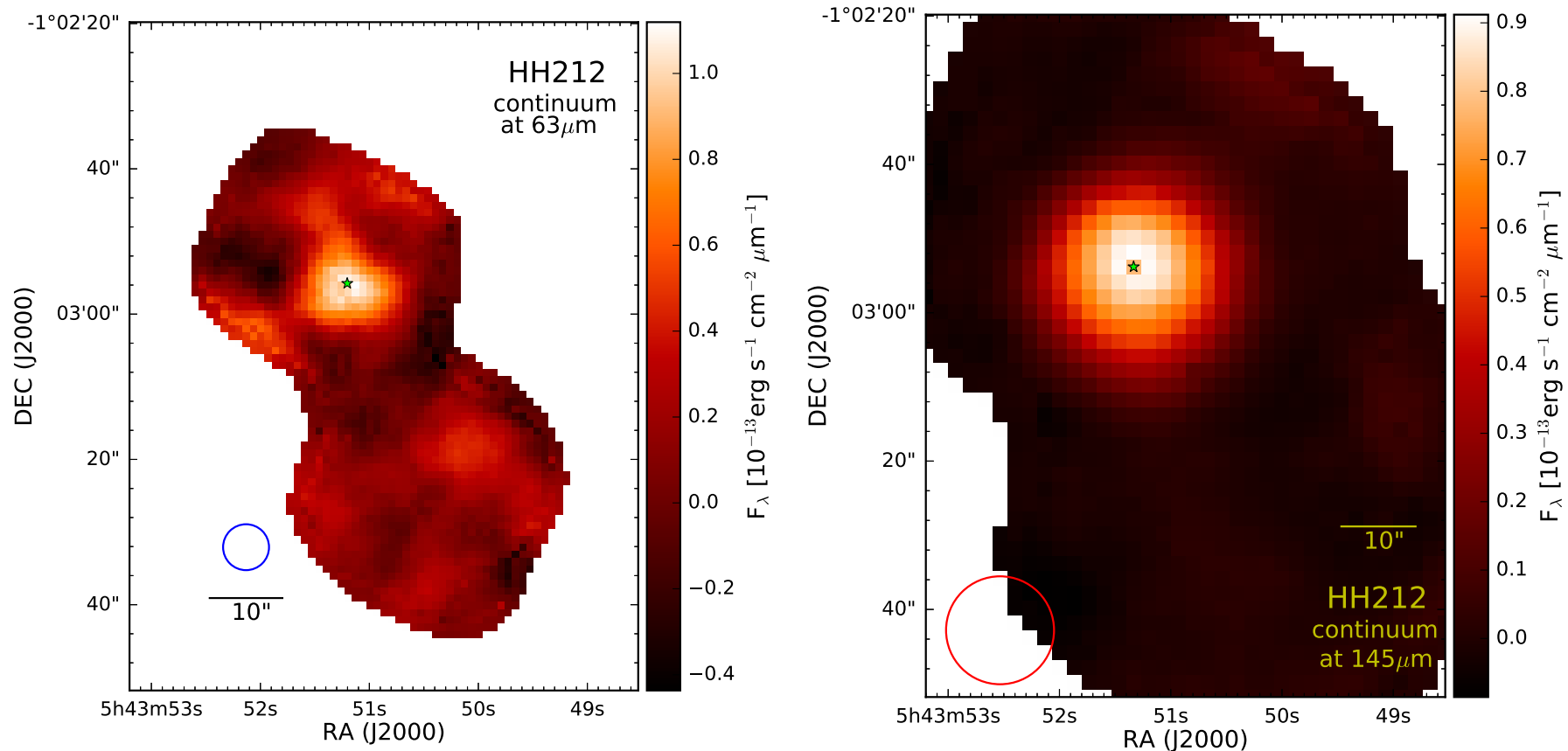


Fig. B.3. Continuum maps of HH 212.

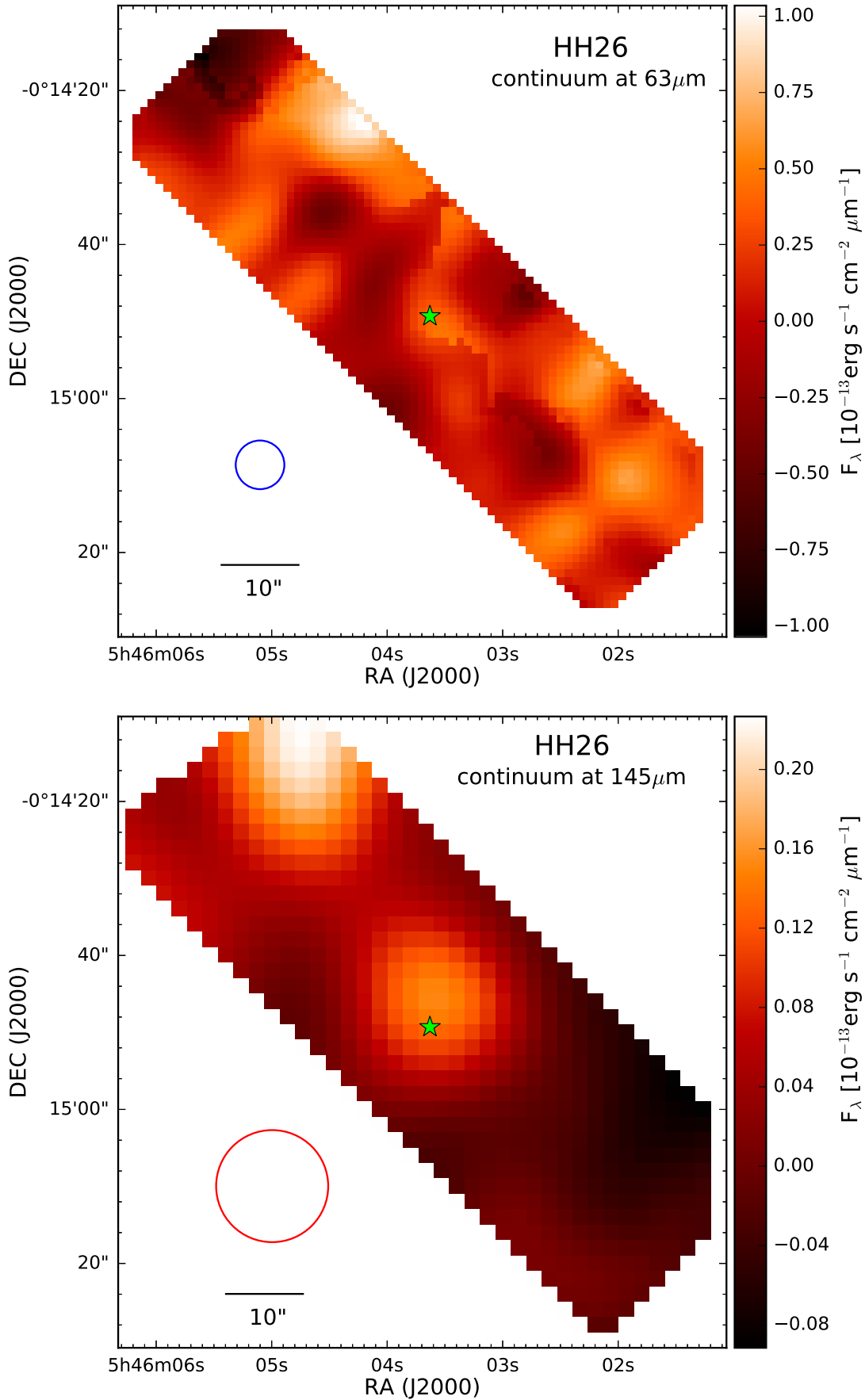


Fig. B.4. Continuum maps of HH 26.

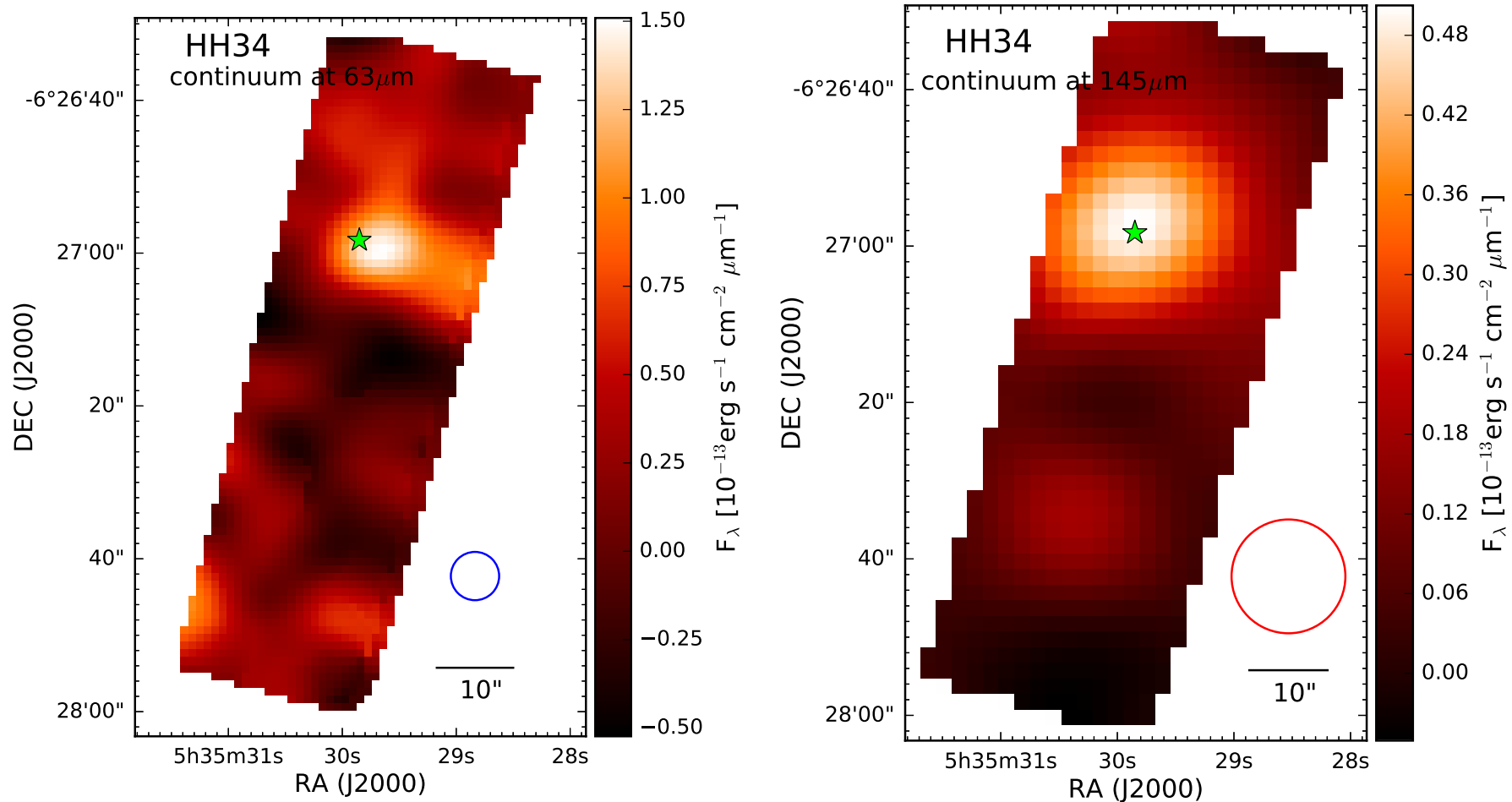


Fig. B.5. Continuum maps of HH 34.

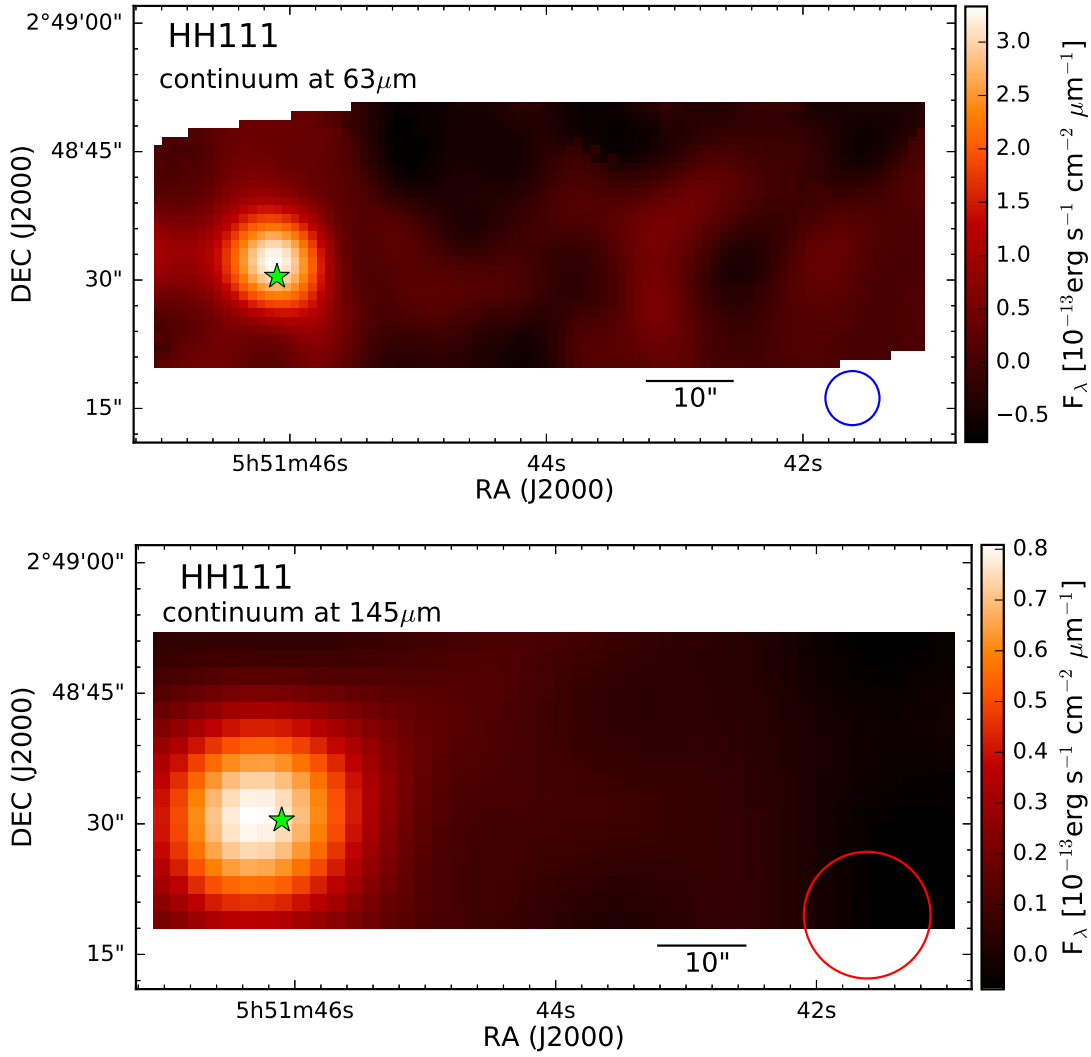


Fig. B.6. Continuum maps of HH 111.

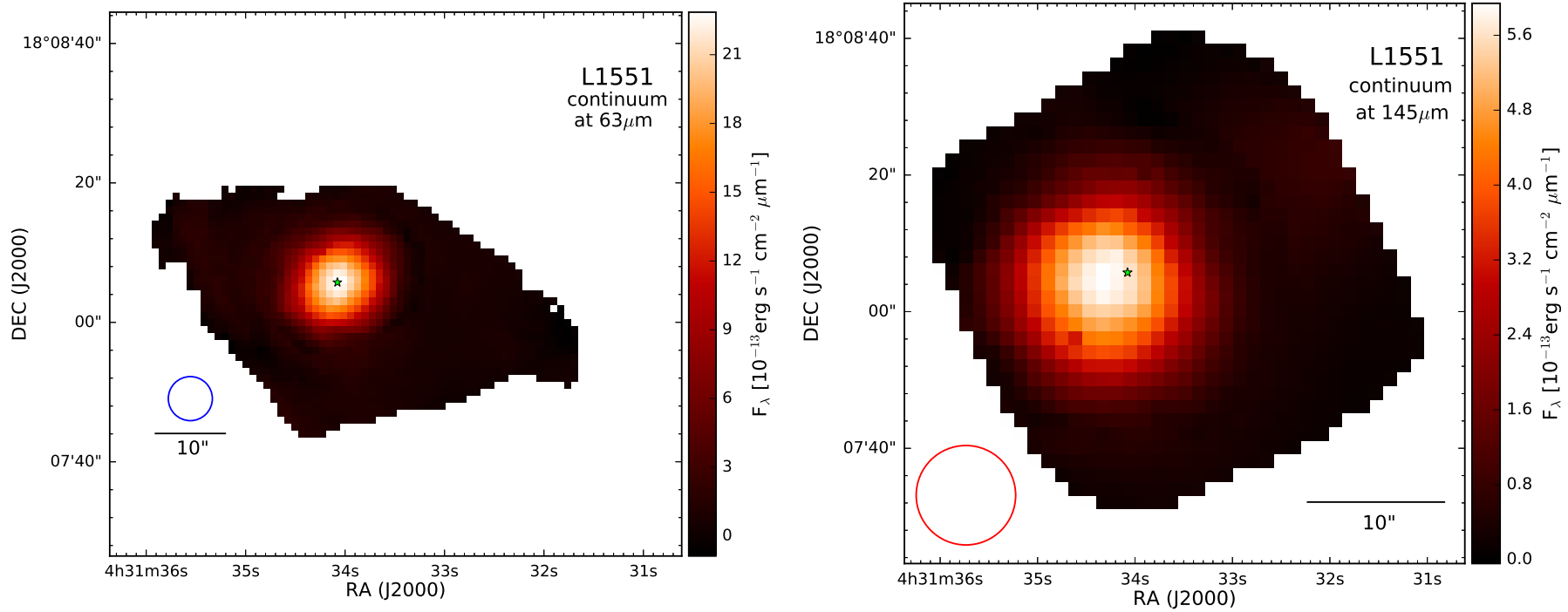


Fig. B.7. Continuum maps of L1551 IRS5.

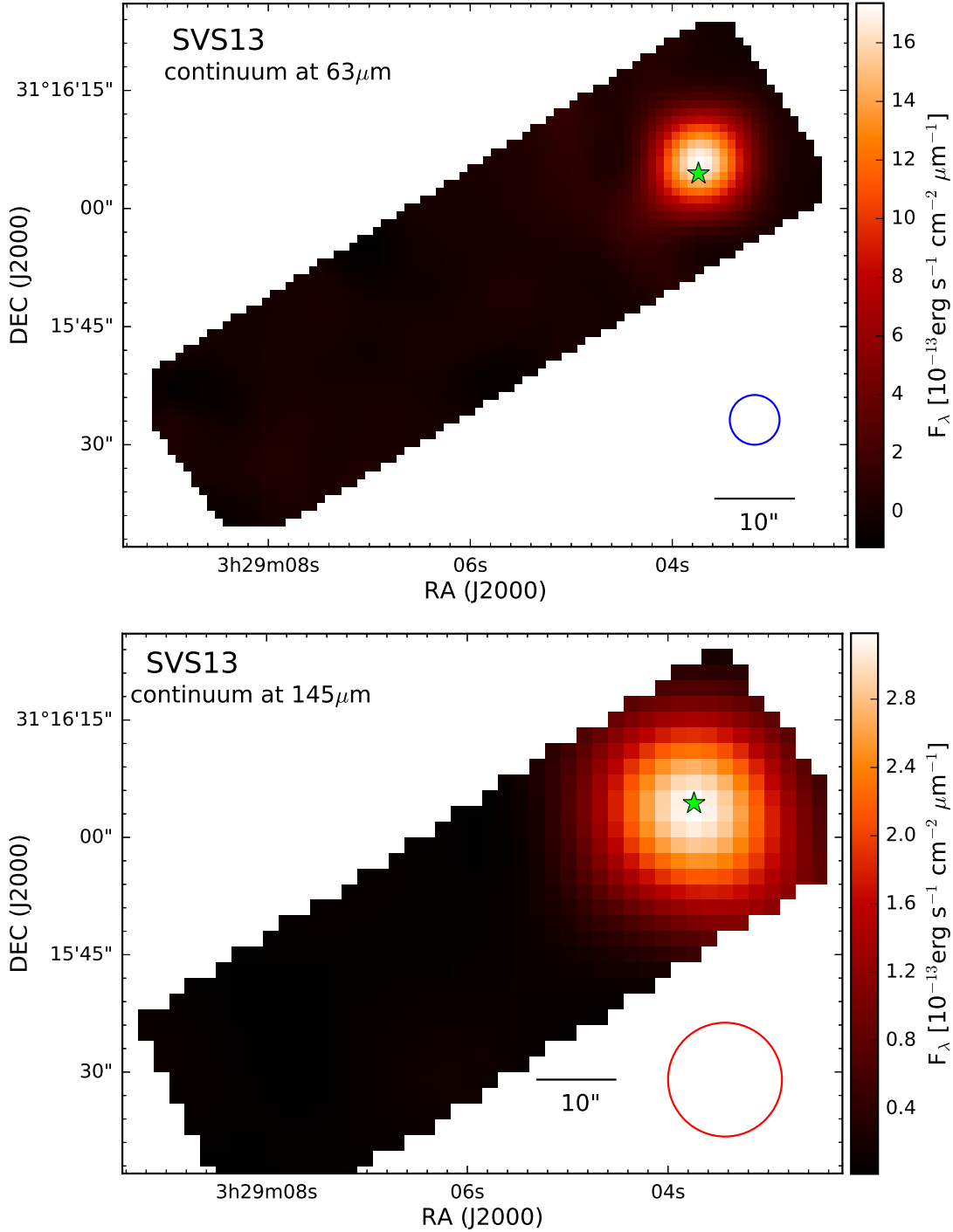


Fig. B.8. Continuum maps of SVS 13.

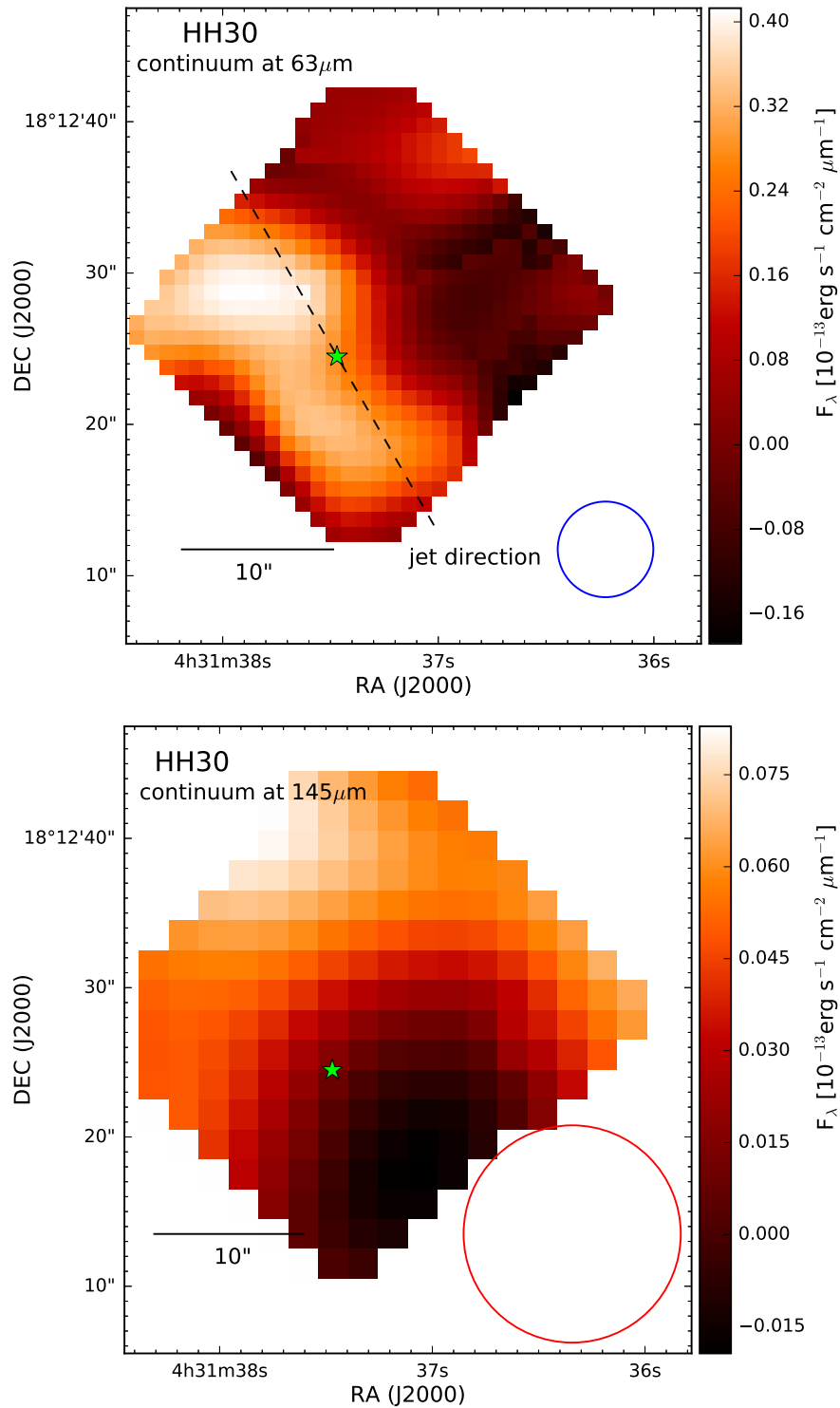


Fig. B.9. Continuum maps of HH 30.

APPENDIX C

Publications, Talks and accepted Proposals

Paper

1. *Probing the hidden atomic gas in Class I jets with SOFIA* (fully refereed)

T. Sperling, J. Eislöffel, C. Fischer, B. Nisini, T. Giannini and A. Krabbe, 2020, *A&A*, 642, A216

2. *Evolution of the atomic component in protostellar outflows* (fully refereed)

T. Sperling, J. Eislöffel, C. Fischer, B. Nisini, T. Giannini and A. Krabbe, *A&A*, 650, A173

Talks

- **Tautenburg presentation series (Tautoloquium)**

(12.02.2018 Tautenburg)

Jets from another world

- **Spectroscopy with SOFIA: new results & future opportunities**

(20–23.01.2019 Ringberg Castle)

Probing the hidden atomic gas in Class I jets

- **The 2019 Annual Meeting of the German Astronomical Society: Mission**

to the Universe – From Earth to Planets, Stars & Galaxies

(16–20.09.2019 Stuttgart)

SOFIA observations of [OI]-outflows from Class I objects

Accepted proposals

- SOFIA Cycle 7 Proposal, ID 07_0069

Probing the hidden atomic gas in Class I jets

observed targets: HH1, HH212, L1551 IRS5

Ehrenwörtliche Erklärung

Ich erkläre hiermit ehrenwörtlich, dass ich die vorliegende Arbeit selbständig, ohne unzulässige Hilfe Dritter und ohne Benutzung anderer als der angegebenen Hilfsmittel und Literatur angefertigt habe. Die aus anderen Quellen direkt oder indirekt übernommenen Daten und Konzepte sind unter Angabe der Quelle gekennzeichnet.

Bei der Auswahl und Auswertung folgenden Materials haben mir die nachstehend aufgeführten Personen in der jeweils beschriebenen Weise entgeltlich/unentgeltlich geholfen:

- Dr. Jochen Eislöffel – durch seine fachliche Betreuung der vorliegenden Arbeit
- Dr. Brunella Nisini, Dr. Teresa Giannini – durch die gemeinsame Arbeit an den beiden wissenschaftlichen Publikationen, auf deren Konzept diese Thesis aufbaut
- Dr. Christian Fischer – Bestimmung der passenden Flugparameter für die Datenauswertung, Konzeption der Auswertungsroutine JENA.py

Weitere Personen waren an der inhaltlich-materiellen Erstellung der vorliegenden Arbeit nicht beteiligt. Insbesondere habe ich hierfür nicht die entgeltliche Hilfe von Vermittlungs- bzw. Beratungsdiensten (Promotionsberater oder andere Personen) in Anspruch genommen. Niemand hat von mir unmittelbar oder mittelbar geldwerte Leistungen für Arbeiten erhalten, die im Zusammenhang mit dem Inhalt der vorgelegten Dissertation stehen.

Die Arbeit wurde bisher weder im In- noch im Ausland in gleicher oder ähnlicher Form einer anderen Prüfungsbehörde vorgelegt. Die geltende Promotionsordnung der Physikalisch-Astronomischen Fakultät ist mir bekannt. Ich versichere ehrenwörtlich, dass ich nach bestem Wissen und Gewissen die reine Wahrheit gesagt und nichts verschwiegen habe.

Ort und Datum

Unterschrift